

**DISCLAIMER:**

This document does not meet the current format guidelines of the Graduate School at The University of Texas at Austin.

It has been published for informational use only.

Copyright  
by  
Justin M. Dragna  
2011

**The Dissertation Committee for Justin M. Dragna Certifies that this is the approved  
version of the following dissertation:**

**Sensing Chiral Amines *via* Supramolecular Chemistry and Circular  
Dichroism Spectroscopy**

**Committee:**

---

Eric Anslyn, Supervisor

---

Jon Sessler

---

Dionicio Siegel

---

David Hoffman

---

Philip Magnus

---

Jason Shear

---

Walter Fast

**Sensing Chiral Amines *via* Supramolecular Chemistry and Circular  
Dichroism Spectrometry**

**by**

**Justin M. Dragna, B. S.**

**Dissertation**

Presented to the Faculty of the Graduate School of Chemistry and Biochemistry

The University of Texas at Austin

in Partial Fulfillment

of the Requirements

for the Degree of

**Doctor of Philosophy**

**The University of Texas at Austin**

**August 2011**

## **Dedication**

In memory of my dad.

## Acknowledgements

Thanks to all of the members of the Anslyn group. Thanks to Marco for all the helpful scientific talks and getting me through my second year exam. Thanks to Colin for enriching my life with outdoor activities, fitness, and beard love. Thanks Jeff for helping me destroy my kidneys by participating in countless lab work breaks to drink soda and for the helpful scientific talks that accompanied those breaks. Thanks to Alex for turning me onto the wonders of expired horse blood. Thanks Guru for helping me collect some last minute NMR spectra.

Thanks to Eric for being such a supportive, and all around great, advisor. Eric's unwavering optimism about science and life helped keep me motivated throughout my Ph.D.

Thanks to both of the undergraduates that worked under my guidance, Lee and Soo. Thanks to Lee for contributing his extremely skilled hands in the collection of data for chapters 3 and 4. Thanks Soo for helping collect data for chapter 2.

Thanks to my sister who is a constant source of inspiration for everything I do in my life - ride to die.

Thanks to Bruce and Corinne Gibb. Bruce and Corinne have been great advisors and friends over the years.

I extend a special thanks to my wife, Heather. Without Heather I would have self-destructed long before I completed my Ph.D.

# **Sensing Chiral Amines *via* Supramolecular Chemistry and Circular Dichroism Spectrometry**

Justin M. Dragna, Ph.D.

The University of Texas at Austin, 2011

Supervisor: Eric V. Anslyn

In chapter 1 the principles behind circular dichroism spectroscopy and exciton coupled circular dichroism spectroscopy are outlined, and examples are cited that illustrate the utility of these methods in the determination of absolute configuration and *ee* of chiral amines. This provides background and context for this thesis, which mostly pertains to the sensing of chirality in amines.

An exciton coupled circular dichroism method based on the induction of helical chirality in an organometallic host for sensing chiral amines is presented in chapter 2. The method can be used to determine absolute configuration by relating the sign of the first Cotton effect of the host-amine complex to the handedness of the amine. Analysis of the primary circular dichroism optical data is by principal component analysis allows for differentiation of the analytes based on their identity and handedness.

A novel circular dichroism method for detecting chiral amines is discussed in chapter 3. The method uses a highly efficient derivatization method to convert the primary amine into a bidentate imine. Three equivalents of the imine are then assembled together by coordination to Fe(II). The proximity and chiral orientation of the imines leads to exciton coupled circular dichroism, which is of utility in the determination of absolute configuration. Additionally, there is a metal-to-ligand charge transfer band in

the visible region that can be used to develop calibration curves, which allow for the determination of the enantiomeric excess of unknown samples with an absolute error of  $\pm 5\%$ .

Chapter 4 details another imine based circular dichroism method for chiral amines. The method uses a commercially available aldehyde, Fe(II), and circular dichroism spectrometry to sense chirality in amines. It is shown that the circular dichroism signals in the ultraviolet spectrum vary predictably with the handedness of the chiral amine, which has potential applications in the determination of absolute configuration. By developing calibration curves, signals in the visible spectrum can be used to determine enantiomeric excess with an absolute error of  $\pm 6\%$ . Analyzing the primary circular dichroism optical data with linear discriminant analysis allows for differentiation between amines based on their identity and handedness.

Finally, chapter 5 illustrates the potential of using the thermodynamic parameters of partitioning between water and octanol as a predictive tool for estimating the contributions of hydrophobicity to host-guest binding events. This is done by showing a relationship between the thermodynamics of partitioning and thermodynamics of hydrophobic binding events for a series of guests and cyclodextrin. A plot of the thermodynamic parameters of binding of a variety of guests to cyclodextrin as a function of the thermodynamic parameters of partitioning between water and octanol shows a linear relationship for a series of alcohols.



## Table of Contents

List of Tables.....	xii
List of Schemes .....	xiv
List of Figures .....	xvi
Chapter 1: Introduction .....	24
1.1 Introduction .....	24
1.1.1 Absolute Configuration .....	24
1.1.2 Methods For Determining Absolute Configuration .....	25
1.1.3 Enantiomeric Excess .....	26
1.1.4 Methods for Determining Enantiomeric Excess .....	26
1.2 Circular Dichroism .....	27
1.2.1 Enantiomeric Excess Determation by induced CD in Metals ...	27
1.2.2 Exciton Coupled Circular Dichroism .....	29
1.3 ECCD by Covalent Modification of the Analyte .....	29
1.3.1 Chiral Diols .....	29
1.3.2 Amino Acids and Amines .....	31
1.3.3 Allylic Alcohols .....	32
1.4 ECCD by Supramolecular Recognition of the Analyte .....	33
1.4.1 Qualitative Overview of Host-Guest Energetics for ECCD induction .....	34
1.5 Supramolecular ECCD Methods for Sensing Chiral Amines .....	36
1.5.1 Porphyrin Tweezers.....	36
1.5.2 Polyacetylene Host .....	40
1.5.3 Aldehyde and Ketone Based Sensors .....	42
1.6 Summary and Goals .....	45
1.7 Other Thesis Topics .....	45
1.8 References .....	45

Chapter 2: Supramolecular ECCD Method for Determining Absolute Configuration of $\alpha$ -Chiral Primary Amines .....	49
2.1 Introduction .....	49
2.1.1 Design Criteria .....	49
2.2 Results and Discussion .....	50
2.2.1 Amines Studied .....	50
2.2.2 Induction of ECCD.....	50
2.2.3 Model for Asymmetric Induction.....	52
2.2.4 Principal Component Analysis.....	53
2.3 Summary and Conclusions .....	54
2.4 Experimental Details .....	55
2.4.1 CD Spectra .....	55
2.5 References .....	58
Chapter 3: Iron(II) and Aldehyde Sensing Ensemble for the Determination of Enantiomeric Excess and Absolute Configuration of $\alpha$ -Chiral Primary Amines .....	59
3.1 Introduction .....	59
3.1.1 Design Criteria .....	60
3.2 Results and Discussion .....	61
3.2.1 Increasing the Rate of Imine Formation.....	61
3.2.2 Choice of Analytes and Derivatization Method .....	62
3.2.3 Determining Saturation <i>via</i> UV-vis Titrations .....	64
3.2.4 Stereoisomerism .....	65
3.2.5 Constructing Calibration Curves .....	67
3.2.6 Crystal Structure.....	73
3.2.7 NMR Experiments to Determine the Diastereomeric Bias .....	74
3.2.8 Exciton Coupling.....	75
3.2.9 Enantiomeric Excess Determination .....	77
3.3 Conclusions .....	80
3.4 Experimental Details .....	81
3.4.1 General .....	81

3.4.2 UV-Visible Titrations.....	81
3.4.3 Calibration Curves and Test Sample Experimental for PPI.....	81
3.4.4 Calibration Curves and Test Sample Experimental for CPI.....	82
3.4.5 Calibration Curves and Test Sample Experimental for HPI....	82
3.5 Probability Calculations.....	83
3.5.1 General.....	83
3.5.2 Probability Calculations at 100% <i>ee</i> .....	83
3.5.3 Probability Calculations at 80% <i>ee</i> .....	83
3.6 NMR Spectra.....	87
3.6.1 <sup>1</sup> H NMR Spectra for PPI, CPI, and HPI.....	87
3.6.2 <sup>1</sup> H NMR Spectra for Enantiomerically Impure Solutions of PPI- Fe(II).....	89
3.7 References:.....	105
Chapter 4: Chiral Amine Sensing via Iron(II) Templated Imine Formation.....	106
4.1 Introduction:.....	106
4.1.1 Design Criteria:.....	106
4.2 Results and Discussion.....	107
4.2.1 Imine Formation.....	107
4.2.2 Choice of Analytes.....	108
4.2.3 Titrations.....	109
4.2.4 Stereoisomerism.....	110
4.2.5 Absolute Configuration and Exciton Coupling.....	112
4.2.6 Linear Discriminant Analysis.....	117
4.2.7 Calibration Curves and Test Samples.....	118
4.3 Summary.....	120
4.4 Experimental Details and Supplementary Information.....	121
4.5 References.....	153
Chapter 5. Correlating Hydrophobicity in Guest Binding to Cyclodextrin with Guest Partitioning Between Water and n-Octanol.....	154
5.1 Introduction.....	154

5.1.1 Design Criteria .....	155
5.2 Results and Discussion .....	156
5.2.1 Alcohols .....	156
5.2.2 Substituted Benzenes.....	159
5.3 Summary .....	162
5.4 References .....	162

## List of Tables

Table 2.1. A table showing the identity of the amine, the wavelength of first Cotton effect, and the sign and magnitude of the CD signal. ....	52
Table 3.1. A table of the calculated probabilities spanning 100% <i>ee</i> to -100% <i>ee</i> for different mixtures of chiral imine stereogenic centers surrounding Fe(II). ....	69
Table 3.2. A list of the actual <i>ee</i> values as calculated from enantiomerically pure solutions and those determined using the assay (Experimental <i>ee</i> ). 79	
Table 3.3. A summary of the calculated probabilities for populations of different isomer sets at different <i>ee</i> values. A negative sign is introduced for the probabilities for ( <i>S,S,R</i> ) and ( <i>S,S,S</i> ) to reflect the equal and opposite nature of CD signals for different enantiomers. ....	86
Table 3.4. Crystal data and structure refinement for <i>S-PPI-Δ-fac</i> Fe(II) .....	92
Table 3.5. Bond lengths [Å] and angles [°] for <i>S-PPI-Δ-fac</i> Fe(II). ....	95
Table 3.6. Atomic coordinates ( x 10 <sup>4</sup> ) and equivalent isotropic displacement parameters (Å <sup>2</sup> x 10 <sup>3</sup> )for <i>S-PPI-Δ-fac</i> Fe(II). U(eq) is defined as one third of the trace of the orthogonalized U <sup>ij</sup> tensor. ....	99
Table 3.7. Hydrogen coordinates ( x 10 <sup>4</sup> ) and isotropic displacement parameters (Å <sup>2</sup> x 10 <sup>3</sup> )for <i>S-PPI-Δ-fac</i> Fe(II) .....	102
Table 3.8. Anisotropic displacement parameters (Å <sup>2</sup> x 10 <sup>3</sup> ) for <i>S-PPI-Δ-fac</i> Fe(II). The anisotropic displacement factor exponent takes the form: -2p <sup>2</sup> [ h <sup>2</sup> a* <sup>2</sup> U <sub>11</sub> + ... + 2 h k a* b* U <sub>12</sub> ] .....	104
Table 4.1. A summary of how the sign of the CD signals vary predictably with the handedness of the amines. ....	112

Table 4.2. A summary of the experimental, actual <i>ee</i> values, and absolute errors for the different amines studied. ....	119
Table 4.3. Crystal data and structure refinement for the <b>R-MBA</b> derivative of complex <b>4.2</b> . ....	136
Table 4.4. Atomic coordinates ( x 10 <sup>4</sup> ) and equivalent isotropic displacement parameters (Å <sup>2</sup> x 10 <sup>3</sup> ) for the <b>R-MBA</b> derivative of complex <b>4.2</b> . U(eq) is defined as one third of the trace of the orthogonalized U <sup>ij</sup> tensor. ....	139
Table 4.5. Bond lengths [Å] and angles [°] for the <b>R-MBA</b> derivative of complex <b>4.2</b> . ....	145
Table 4.6. Anisotropic displacement parameters (Å <sup>2</sup> x 10 <sup>3</sup> ) for the <b>R-MBA</b> derivative of complex <b>4.2</b> . The anisotropy displacement factor exponent takes the form: $-2\pi^2 [ h^2 a^{*2} U^{11} + \dots + 2 h k a^* b^* U^{12} ]$ ....	148
Table 4.7. Hydrogen coordinates ( x 10 <sup>4</sup> ) and isotropic displacement parameters (Å <sup>2</sup> x 10 <sup>3</sup> ) for the <b>R-MBA</b> derivative of complex <b>4.2</b> . ....	149
Table 4.8. Torsion angles [°] for for the <b>R-MBA</b> derivative of complex 4.2. ...	153

## List of Schemes

- Scheme 1.1. The chiral Cu(I) receptor and imine binding scheme for our previously reported protocol. A CD active charge transfer band is present in the receptor and is modulated upon binding of the imine. .... 28
- Scheme 1.2. Diol **1.2** is converted to **1.3** in the strategy developed by Nakanishi for the determination of the absolute configuration of chiral diols by the benzoate or ECCD method. The sign between the two benzoates can be related to the absolute configuration of the diols. .... 30
- Scheme 1.3. Steroid **1.4** is converted to porphyrin derivative **1.5** to determine the absolute configuration of chiral diols. .... 30
- Scheme 1.4. The system used by Canary *et al.* to determine the absolute configuration of amino acids. Reaction of the amine moiety with 2 equivalents of 2-Br-quinoline followed by complexation to Cu(II) leads to intense ECCD. The sign of the dihedral angle between the chromophores correlates with the identity of the stereogenic center of the amino acid. .... 31
- Scheme 1.5. An extension of the original Canary system from amino acids to primary amines. The sign of the dihedral angle correlates with the sign of the ECCD couplet. However, the amplitude of the ECCD is much smaller than those of the similar amino acid adducts. .... 32
- Scheme 1.6. The method used by Berova *et al.* in the determination of absolute configuration of allylic alcohols. .... 33
- Scheme 1.7. The two step derivatization method for amino acids and amino alcohols used by Nakanishi. .... 39

Scheme 1.8. The method used by Nakanishi to derivatize primary chiral amines.	39
Scheme 1.9. Inoue's porphyrin tweezer system for determining the absolute configuration of underivatized primary amines. The tweezer opens up from the syn conformation to the anti conformation upon binding a chiral amine.	40
Scheme 1.10. The biaryl host used by Wolf <i>et al.</i> for sensing amino alcohols. <b>1.19</b> exists as an equal mixture of conformational isomers. Reaction of the host with an enantiomerically pure amino alcohol leads adduct <b>1.19</b> , which has extensive hydrogen bonding (in red) and favors one helical isomer.	44
Scheme 1.11. The aryl probe used by Wolf <i>et al.</i> to sense chirality in diamines. Upon reaction with a diamine the host becomes conformationally locked.	44
Scheme 2.1. The receptor employed, <b>2.1</b> , and the predicted binding mode.	49
Scheme 3.1. The chiral Cu(I) receptor <b>3.1</b> and imine binding scheme for our previously reported protocol. A CD active charge transfer band is present in the receptor and is modulated upon binding of the imine.	60
Scheme 3.2. Aldehyde <b>3.2</b> is used to convert a chiral amine into bidentate imine <b>3.3</b> . The imine is complexed to Fe(II) to form the octahedral complex <b>3.4</b> .	61
Scheme 4.2. A comparison of the reactivity of aldehyde <b>4.1</b> with amines in the absence and presence of Fe(II) and with the reactivity of pyridine carboxaldehyde in the presence of amines.	108



## List of Figures

- Figure 1.2. Positive helical chirality is described by M or  $\Lambda$  and negative helical chirality is described by P or  $\Delta$  as seen for the atropisomers of 1,2-dibromoethane. Of course, at room temperature the enantiomers are inseparable due to a low energy barrier to rotation around the carbon-carbon bond..... 25
- Figure 1.3. A positive first Cotton effect is seen for an ECCD couplet if the sign of the dihedral angle between the chromophores is positive, as shown above. Conversely, a negative first Cotton effect is seen if the sign of the dihedral angle is negative..... 29
- Figure 1.4. A hypothetical potential energy diagram for a host, H, and a bidentate guest G. The anti conformer A is highest in energy because it only has one favorable interaction with the analyte. The syn conformers B and C are lower in energy than A because each has two favorable interactions between H and G. The difference in energy between B and C is arbitrary and illustrates that differentiation between B and C is possible only if it is energetically favorable to populate the syn conformer. .... 35
- Figure 1.5. A hypothetical potential energy diagram for a host, H, and a monodentate guest G. The syn conformers A and B are higher in energy than the anti conformer C because they possess the same number of favorable interactions with the G, but are more sterically strained. The energy difference between A and B is of little consequence since C would be the most populated state. .... 36

Figure 1.6. The porphyrin tweezer developed by Nakanishi <i>et al.</i> . Binding of diamines results in complex <b>1.12</b> . The disymmetric restriction of the chromophores leads to ECCD. ....	38
Figure 1.7. The polyacetylene polymer host used by Okamoto for the sensing of chiral primary amines and amino alcohols.....	41
Figure 1.8. The binding mode proposed by Okamoto for recognition of chiral primary amines by polyacetylene <b>1.15</b> . The large group points away from the polymer, and the model proposed by Okamoto <i>et al.</i> for asymmetric induction from amino alcohols to polyacetylene <b>1.15</b> . The alcohol provides an additional interaction with the polymer.	42
Figure 1.9. The ketone host used by Chin <i>et al.</i> for amino acid recognition. L- amino acids induce a positive helical twist <i>via</i> hydrogen bonding (shown in red) between the carboxylate and the phenol. ....	43
Figure 2.1. The chiral amines chosen for study. ....	50
Figure 2.2. The CD and UV-vis spectra of <b>2.1-MBA</b> at 0.3mM of <b>2.1</b> and 0.6mM of <b>MBA</b> in methylene chloride in a 0.1cm quartz cell. ....	51
Figure 2.3. Two different views of the host-guest complex in equilibrium between the <i>S</i> - $\Lambda$ and <i>S</i> - $\Delta$ isomer. The equilibrium favors the <i>S</i> - $\Lambda$ isomer because the steric interaction between the quinoline and $R_M$ is less severe than the steric interaction between the quinoline and $R_L$ in the <i>S</i> - $\Delta$ .....	53
Figure 2.4. A PCA plot showing how the analytes separate across two axes. The primary optical data for the PCA plot was collected at 260, 240, and 235nm.....	54
Figure 2.5. The CD spectrum of <b>2.1-MBA</b> .....	55

Figure 2.6. The CD spectrum of <b>2.1-NBA</b> .....	56
Figure 2.7. The CD spectrum of <b>2.1-CHA</b> .....	56
Figure 2.8. The CD spectrum of <b>2.1-AHA</b> .....	57
Figure 2.9. The CD spectrum of <b>2.1-IPA</b> .....	57
Figure 3.1. The three amines studied. ....	62
Figure 3.2. The imines formed after reaction of the amines with aldehyde <b>3.3</b> ...	63
Figure 3.3. UV- <i>vis</i> and CD spectra of the MLCT bands of <b>3.4</b> for the three different imines studied, <b>PPI</b> (3mM), <b>CPI</b> (6mM), and <b>HPI</b> (7mM), at 100% <i>ee</i> in acetonitrile at 1mM Fe(II) in a 0.1cm quartz cell.....	63
Figure 3.4. The change in absorbance as a function of equivalents of imine titrated into an acetonitrile solution of 1mM Fe(II) at 575nm, 577nm, and 570nm for <b>PPI</b> , <b>CPI</b> , and <b>HPI</b> , respectively. Equivalents of imine is defined as the concentration of imine divided by the concentration of Fe(II).....	64
Figure 3.5. The 24 possible stereoisomers that can form upon mixing of enantiomers of <b>3.3</b> with Fe(II). In this figure, the isomers are organized by the mixture of stereogenic centers on each complex, the geometry isomerism ( <i>fac</i> and <i>mer</i> ), and the helical isomerism (D and L). The red dotted lines trace out the ‘face’ and ‘meridian’ defined by the three imine nitrogens for the <i>fac</i> and <i>mer</i> isomers, respectively.	66
Figure 3.6. A plot of the ellipticity at 519nm as a function of <i>ee</i> with 1mM Fe(II), 2mM <b>3.3</b> , and 3mM, 4mM, and 5mM of <b>PPI</b> (derived from <b>MBA</b> ) in acetonitrile in a 0.1cm cell. ....	67

Figure 3.7. A plot of the ellipticity at 525nm as a function of <i>ee</i> with 1mM Fe(II), 2mM <b>3.3</b> , and 6mM, 7mM, 8mM, and 9mM of <b>CPI</b> (derived from <b>CEA</b> ) in acetonitrile in a 0.1cm cell. ....	68
Figure 3.8. The overlay of the uncorrected calculated data, corrected calculated data, and experimental data for <b>MBA</b> .....	71
Figure 3.9. The overlay of the uncorrected calculated data, corrected calculated data, and experimental data for <b>CEA</b> . ....	72
Figure 3.10. The overlay of the uncorrected calculated data, corrected calculated data, and experimental data for <b>HPA</b> .....	72
Figure 3.11. A crystal structure of the <i>S</i> - <b>PPI</b> - $\Delta$ - <i>fac</i> Fe(II) showing a partial atom labeling scheme. Displacement ellipsoids are scaled to the 50% probability level. Most hydrogen atoms were removed for clarity. ....	73
Figure 3.12. <sup>1</sup> H NMR spectrum of the <b>PPI</b> -Fe(II) complex at -100% <i>ee</i> . The four quartets correspond to the benzylic proton (in red) for the four different diastereomers .....	75
Figure 3.13. The helical arrangement of the transition dipoles that couple giving rise to the positive and negative ECCD couplets for the $\Delta$ - <i>R</i> and $\Lambda$ - <i>S</i> <i>fac</i> isomers, respectively. ....	76
Figure 3.14. The ECCD spectra for the <b>PPI</b> , <b>CPI</b> , and <b>HPI</b> Fe(II) complexes at 0.3mM in a 0.1cm cuvette.....	77
Figure 3.15. A graph of the probability of the four different isomer sets as functions of enantiomeric excess. ....	85
Figure 3.16. A graph of the four different isomer sets as a functions of <i>ee</i> with the introduction of a sign change for predominantly <i>S</i> isomer sets. ....	86

Figure 3.17. <sup>1</sup> H NMR of 10mM aldehyde <b>3.2</b> and 6mM <b>MBA</b> . .....	87
Figure 3.18. <sup>1</sup> H NMR of 10mM aldehyde <b>3.2</b> and 6mM <b>CEA</b> . .....	88
Figure 3.19. <sup>1</sup> H NMR of 10mM aldehyde <b>3.2</b> and 6mM <b>HPA</b> . .....	88
Figure 3.20. The <sup>1</sup> H NMR of the <b>PPI</b> -iron(II) complex at -60% <i>ee</i> . .....	89
Figure 3.21. The <sup>1</sup> H NMR of the <b>PPI</b> -iron(II) complex at -20% <i>ee</i> . .....	90
Figure 3.22. The <sup>1</sup> H NMR of the <b>PPI</b> -iron(II) complex at 0% <i>ee</i> . .....	90
Figure 3.23. The <sup>1</sup> H NMR of the <b>PPI</b> -iron(II) complex at 20% <i>ee</i> . .....	91
Figure 3.24. The <sup>1</sup> H NMR of the <b>PPI</b> -iron(II) complex at 60% <i>ee</i> . .....	91
Figure 4.1. The different chiral amines chosen for study .....	108
Figure 4.2. The change in absorbance at 600nm as a function of equivalents of aldehyde for the different amine analytes. ....	110
Figure 4.3. The possible stereoisomers that can exist for enantiomerically impure solutions of complex <b>4.2</b> . ....	111
Figure 4.4. The CD curve for complex <b>4.2</b> derived from <b>CEA</b> . .....	113
Figure 4.5. The UV- <i>vis</i> spectrum for complex <b>4.2</b> derived from <b>CEA</b> . .....	113
Figure 4.6. The CD curve for complex <b>4.2</b> derived from <b>MBA</b> . .....	114
Figure 4.7. The UV- <i>vis</i> spectrum for complex <b>4.2</b> derived from <b>MBA</b> . .....	114
Figure 4.8. A crystal structure of the <i>S</i> - <b>CEA</b> derivative of complex <b>4.2</b> showing a partial atom labeling scheme. Displacement ellipsoids are scaled to the 50% probability level. Most hydrogen atoms were removed for clarity .....	115
Figure 4.9. A crystal structure of the <i>R</i> - <b>MBA</b> derivative of complex <b>4.2</b> showing a partial atom labeling scheme. Displacement ellipsoids are scaled to the 50% probability level. Most hydrogen atoms were removed for clarity .....	116

Figure 4.10. An LDA plot of the CD primary optical data from 275-310nm, 320-340nm, 415-435nm, 465-485nm, 540-560nm, 580-600nm, 620-640nm, and 720-740nm for the different amine analytes. ....	118
Figure 4.11. The primary CD optical data gathered for calibration curves of <b>MBA</b> . .....	121
Figure 4.12. The calibration curve for <b>MBA</b> . ....	122
Figure 4.13. The primary CD optical data gathered for calibration curves of <b>CEA</b> . .....	122
Figure 4.14. The calibration curve for <b>CEA</b> . ....	123
Figure 4.15. The primary CD optical data gathered for calibration curves of <b>HPA</b> . .....	123
Figure 4.16. The calibration curve for <b>HPA</b> . ....	124
Figure 4.17. The primary CD optical data gathered for calibration curves of <b>dmBA</b> . .....	124
Figure 4.18. The calibration curve for <b>dmBA</b> . ....	125
Figure 4.19. The primary CD optical data gathered for calibration curves of <b>AMB</b> . .....	125
Figure 4.20. The calibration curve for <b>AMB</b> . ....	126
Figure 4.21. The primary CD optical data gathered for calibration curves of <b>SBA</b> .	126
Figure 4.22. The calibration curve for <b>SBA</b> . ....	127
Figure 4.23. The UV-vis data collected for <b>MBA</b> for the LDA plot. ....	127
Figure 4.24. The UV-vis data collected for <b>MBA</b> for the LDA plot. ....	128
Figure 4.25. The UV-vis data collected for <b>CEA</b> for the LDA plot. ....	128
Figure 4.26. The UV-vis data collected for <b>CEA</b> for the LDA plot. ....	129
Figure 4.28. The UV-vis data collected for <b>HPA</b> for the LDA plot. ....	130

Figure 4.29. The UV-vis data collected for <b>dmBA</b> for the LDA plot. ....	130
Figure 4.30. The UV-vis data collected for <b>dmBA</b> for the LDA plot. ....	131
Figure 4.31. The UV-vis data collected for <b>SBA</b> for the LDA plot. ....	131
Figure 4.32. The UV-vis data collected for <b>SBA</b> for the LDA plot. ....	132
Figure 4.34. <sup>1</sup> H NMR of the <b>MBA</b> derivative of complex <b>4.2</b> . ....	132
Figure 4.35. <sup>1</sup> H NMR of the <b>dmBA</b> derivative of complex <b>4.2</b> . ....	133
Figure 4.36. <sup>1</sup> H NMR of the <b>CEA</b> derivative of complex <b>4.2</b> . ....	133
Figure 4.37. <sup>1</sup> H NMR of the <b>AMB</b> derivative of complex <b>4.2</b> . ....	134
Figure 4.38. <sup>1</sup> H NMR of the <b>HPA</b> derivative of complex <b>4.2</b> . ....	134
Figure 4.39. <sup>1</sup> H NMR of the <b>SBA</b> derivative of complex <b>4.2</b> . ....	135
Figure 5.1. An illustration of the similarities between the partitioning of a guest, in this case an alcohol, into water/n-octanol and binding to cyclodextrin (labeled $\alpha$ -CD). The water is in blue, and the hydrophobic areas are labeled in orange. ....	156
Figure 5.2. A plot of the free energy of binding to $\alpha$ -cyclodextrin as a function of the free energy of transfer from water to n-octanol for a variety of alcohols. ....	157
Figure 5.3. A plot of the enthalpy of binding to $\alpha$ -cyclodextrin as a function of the enthalpy of transfer from water to n-octanol for a variety of alcohols. .....	158
Figure 5.4. A plot of the entropy of binding to $\alpha$ -cyclodextrin as a function of the entropy of transfer from water to n-octanol for a variety of alcohols. .....	159

Figure 5.5. A plot of the free energy of binding to  $\beta$ -cyclodextrin as a function of the free energy of transfer from water to n-octanol for a variety of alcohols..... 160

Figure 5.6. A plot of the enthalpy of binding to  $\beta$ -cyclodextrin as a function of the enthalpy of transfer from water to n-octanol for a variety of substituted benzenes..... 161

Figure 5.7. A plot of the entropy of binding to  $\beta$ -cyclodextrin as a function of the entropy of transfer from water to n-octanol for a variety of substituted benzenes..... 161



## Chapter 1: Introduction

### 1.1 INTRODUCTION

The determination of absolute configuration and enantiomeric excess (*ee*) is of central importance to the development of chiral drugs.<sup>1-8</sup> Typically, only a single enantiomer of a compound will be of therapeutic value, while the other enantiomer may be inactive or have unwanted side effects.<sup>2,4</sup> Thus, determining the *ee* and absolute configuration of potential pharmaceuticals is an essential step in the development of safe and effective therapeutic compounds.

#### 1.1.1 Absolute Configuration

Absolute configuration refers to the spatial arrangement of the atoms or groups around a stereogenic unit in molecule.<sup>9</sup> For chiral molecules, the most common descriptors in organic chemistry are *R* and *S*, which are based on the Cahn-Ingold-Prelog priority rules, and typically refer to the spatial relationship between atoms attached to a stereogenic carbon atom (Figure 1.1). Another set of descriptors are used to describe helical chirality such as that seen in the conformational stereoisomers of 1,2 dibromoethane (Figure 1.2). The letter P or Greek symbol  $\Delta$  describes a positive clockwise helicity whereas, the letter M or symbol  $\Lambda$  describes a negative or counterclockwise twist.<sup>9</sup>

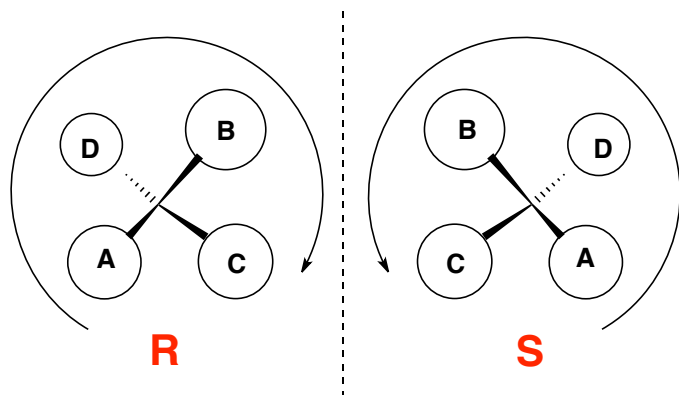


Figure 1.1. The descriptors *R* and *S* are used to describe opposing chirality based on the Cahn-Ingold-Prelog priority system. A, B, C, and D refer to atoms of decreasing atomic number.

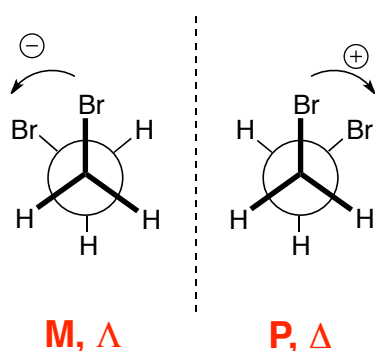


Figure 1.2. Positive helical chirality is described by *M* or  $\Lambda$  and negative helical chirality is described by *P* or  $\Delta$  as seen for the atropisomers of 1,2-dibromoethane. Of course, at room temperature the enantiomers are inseparable due to a low energy barrier to rotation around the carbon-carbon bond.

### 1.1.2 Methods For Determining Absolute Configuration

Absolute configuration can be established non-empirically using the bijvoet x-ray crystallographic method.<sup>10-12</sup> However, in the case of natural products, there is frequently not enough material available to grow a crystal. Chiroptical methods such as circular dichroism (CD) and optical rotatory dispersion (ORD) can also be useful in the determination of absolute configuration, but are usually based on empirical or semiempirical rules, and thus, cannot be used to confidently assign absolute configuration.<sup>10</sup> When only small quantities of a material are

available, the most practical method for assigning absolute configuration is the exciton coupled circular dichroism method (ECCD).<sup>12</sup>

### 1.1.3 Enantiomeric Excess

The two non-superimposable mirror images of a chiral molecule are referred to as enantiomers.<sup>9</sup> A measure of how much of each enantiomer is present in a mixture is the percent enantiomeric excess (*ee*) and is defined as:

$$ee = \frac{(R - S)}{(R + S)} * 100\%$$

Where *R* and *S* are the mole fractions of each of the respective enantiomers in the mixture.<sup>9</sup>

### 1.1.4 Methods for Determining Enantiomeric Excess

Currently, the most common techniques for determining *ee* are chiral HPLC and chiral GC.<sup>13-17</sup> While these methods are effective at determining *ee* with high accuracy, they are presently limited to low-throughput screening.<sup>13-17</sup> Low-throughput screening is a viable technique in traditional asymmetric catalyst discovery where a catalyst is designed, tested, modified and then retested until an acceptable enantioselectivity is reached. However, rapid screening of large libraries of asymmetric catalysts is emerging as a potentially faster and more cost-effective method for the discovery of efficient enantioselective catalysts.<sup>13,14,16-21</sup> Thus, there is clear need for the development of methods for the rapid determination of *ee*.

A variety of methods are under development for the rapid determination of *ee* such as liquid crystals,<sup>22-24</sup> capillary electrophoresis,<sup>18</sup> IR thermography,<sup>19</sup> and optical techniques.<sup>15,16,25-33</sup> Optical techniques such as fluorescence,<sup>16,26-29</sup> UV-vis,<sup>22,23,25,31,32</sup> and CD spectroscopy<sup>30</sup> are

particularly attractive because the instrumentation is commercially available, relatively inexpensive, and data collection is typically fast.

## 1.2 CIRCULAR DICHROISM

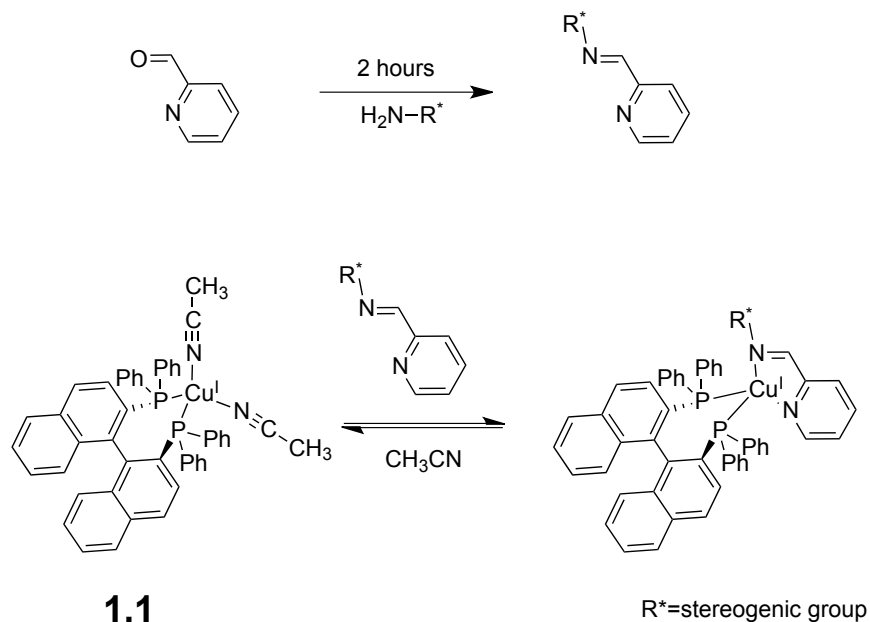
Circular dichroism (CD) spectroscopy allows for the differentiation between enantiomers *via* the use of circularly polarized light.<sup>10</sup> Because circularly polarized light is chiral, it interacts differentially with opposing enantiomers and induces dissymmetric electronic transitions.<sup>10</sup> Thus, left and right circularly polarized light are absorbed differentially by an enantiomerically enriched chiral chromophore, or a chromophore in an enantiomerically enriched chiral environment.<sup>10</sup> The ability of CD to differentiate between enantiomers using a chiral light source make it a natural choice for the determination of *ee* since it potentially eliminates the need for a chiral reagent such as those needed for other techniques such as NMR or UV-*vis*.

### 1.2.1 Enantiomeric Excess Determination by induced CD in Metals

A particularly attractive method for the determination of *ee* is the induction of CD in metals. Several methods have been developed for the induction of CD in metals upon addition of a chiral analyte.<sup>34-40</sup> Nakanishi *et al.* reported the use of a Ni(II) salt as a probe for the detection of chirality in glycols and amino alcohols. In the presence of chiral glycols or amino alcohols, the d-d transitions of Ni(II) become optically active.<sup>36</sup> The sign of the optically active band can be related to the chirality of the glycol or amino alcohol. Similar probes based on Pr(III)<sup>37,40</sup> and Cu(II)<sup>34</sup> have also been reported. However, all of these methods were developed for the empirical determination of absolute configuration. As previously discussed, empirical methods are unreliable for the determination of absolute configuration and are, thus, of limited value. Because of this, over the past 10-15 years, little research has been done on the induction of chirality in metals.

While these methods are not of high utility for the determination of absolute configuration, they have use in the determination of *ee*. Because the determination of *ee* by CD spectrometry requires the use of an empirically determined calibration curve, it is irrelevant whether the signal being used for the calibration curve can be calculated non-empirically. Further, metals offer several advantages. They are typically inexpensive and the signals induced in metals usually appear at high wavelengths,<sup>34-40</sup> which is preferable because it avoids potential interference from other absorbing species such as chromophores inherent to the analyte or solvent.

We recently demonstrated the potential of metal-based systems in the determination of *ee* of  $\alpha$ -chiral primary amines.<sup>30</sup> Amines were first converted to imines using pyridine carboxaldehyde. Binding of the imine to organometallic complex **1.1** resulted in modulation of a CD active charge transfer band and could be used to determine *ee* with an absolute of error of 12%.



Scheme 1.1. The chiral Cu(I) receptor and imine binding scheme for our previously reported protocol. A CD active charge transfer band is present in the receptor and is modulated upon binding of the imine.

## 1.2.2 Exciton Coupled Circular Dichroism

ECCD is a non-empirical CD method commonly used for absolute configuration determination and more recently rapid *ee* determination.<sup>10,12</sup> It arises from the coupling of the excited states of at least two asymmetrically oriented, proximal chromophores.<sup>10</sup> The sign of the first Cotton effect of the ECCD couplet is determined by the sign of the dihedral angle formed between the transition dipoles of the chromophores of interest (Figure 1.3).<sup>10</sup> Thus, absolute configuration can be assigned based on the sign of the first Cotton effect. The Cotton effects produced from ECCD are typically very intense<sup>10</sup> leading to a high signal-to-noise ratio making it possible to determine *ee* with high to moderately high accuracy (less than 5% absolute error).<sup>41,42</sup>

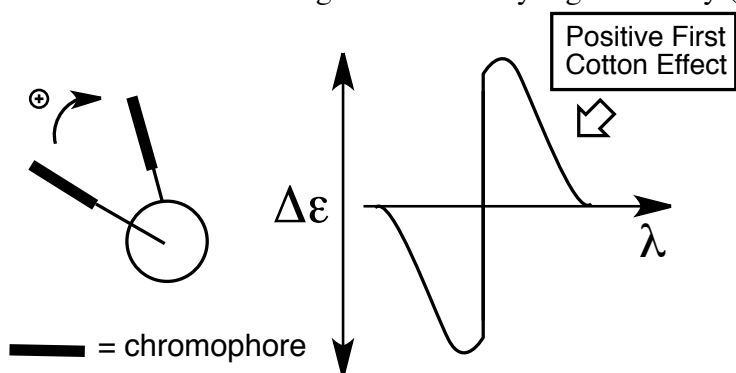


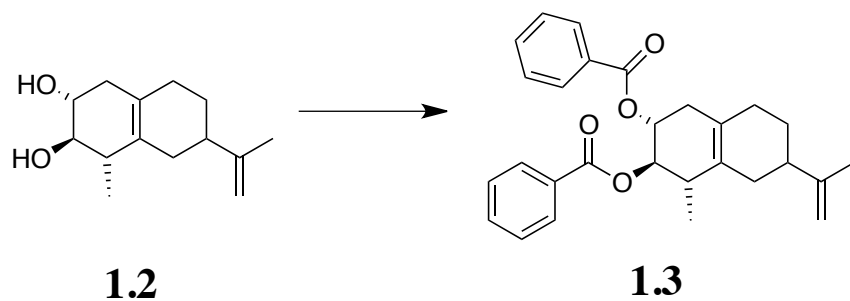
Figure 1.3. A positive first Cotton effect is seen for an ECCD couplet if the sign of the dihedral angle between the chromophores is positive, as shown above. Conversely, a negative first Cotton effect is seen if the sign of the dihedral angle is negative.

## 1.3 ECCD BY COVALENT MODIFICATION OF THE ANALYTE

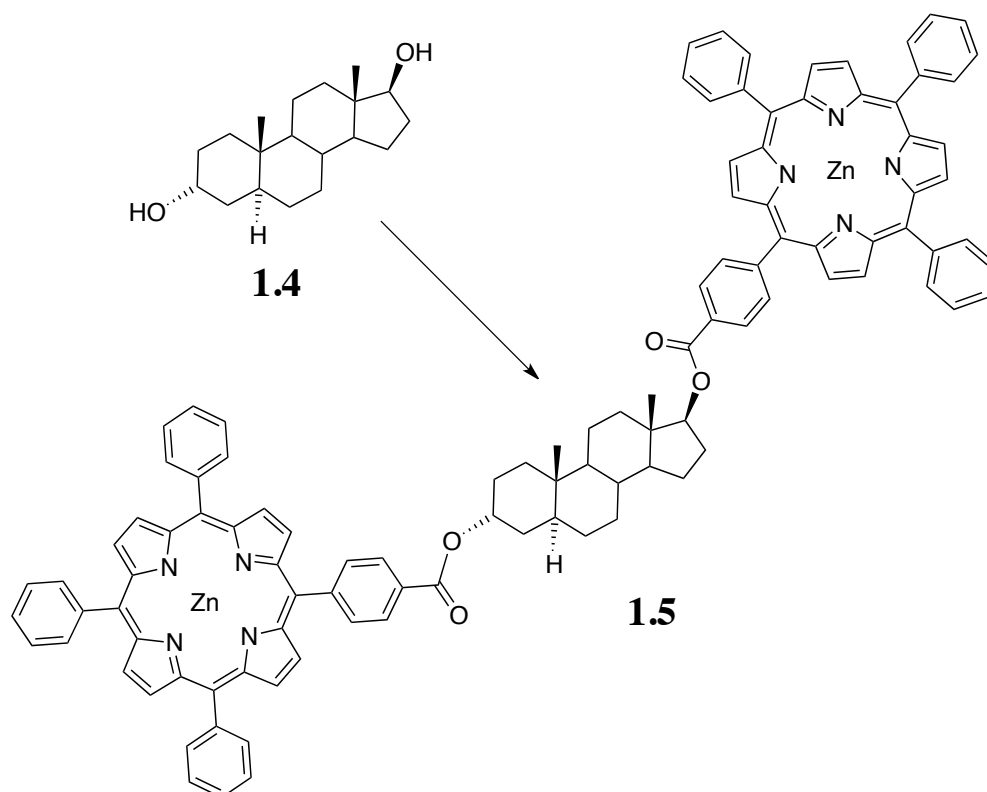
### 1.3.1 Chiral Diols

The ECCD method was originally developed for the determination of absolute configuration of diols.<sup>10,39</sup> The method was called the dibenzoate chirality method and required

the covalent introduction of benzoate groups into the analyte (Scheme 1.2).<sup>10,39</sup> The method was eventually extended to other chromophores, such as porphyrins, and was renamed ECCD (Scheme 1.3).<sup>43</sup>



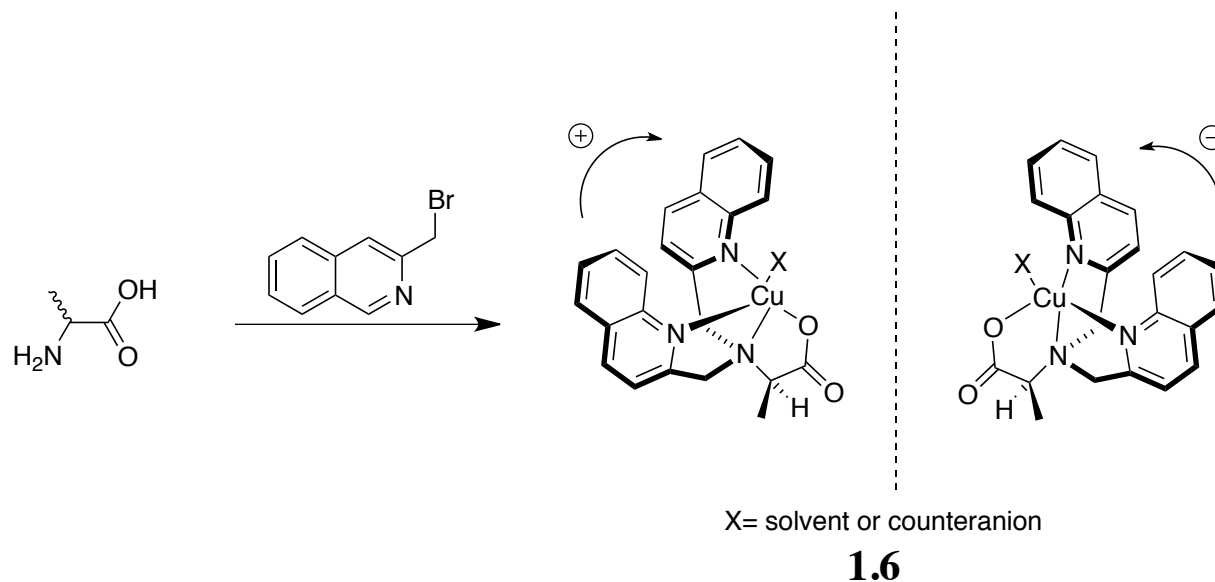
Scheme 1.2. Diol **1.2** is converted to **1.3** in the strategy developed by Nakanishi for the determination of the absolute configuration of chiral diols by the benzoate or ECCD method. The sign between the two benzoates can be related to the absolute configuration of the diols.



Scheme 1.3. Steroid **1.4** is converted to porphyrin derivative **1.5** to determine the absolute configuration of chiral diols.

### 1.3.2 Amino Acids and Amines

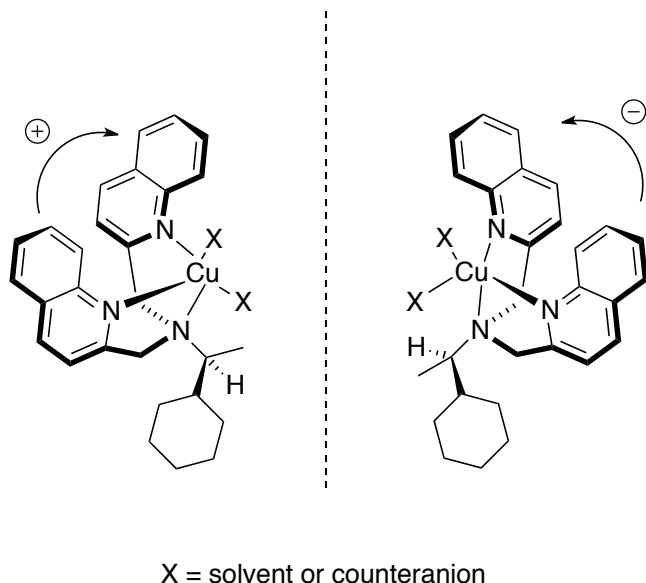
Later, the ECCD method was extended to determining absolute configuration of functional groups other than diols. Canary *et al.* developed a method for the determination of absolute configuration of amino acids.<sup>44,45</sup> The amino acid is converted to a tetradentate ligand by reaction of the amine moiety with two equivalents of 2-bromomethyl quinoline. The ligand is very weakly CD active. However, upon complexation to Cu(II), the structure becomes rigid, and forms the helically biased distorted trigonal pyramidal complex **1.6** (Scheme 1.4). The proximity, rigidity, and chiral orientation of the quinoline groups leads to ECCD, and the sign of the ECCD couplet can be correlated with the identity of the stereogenic center for the amino acid.



Scheme 1.4. The system used by Canary *et al.* to determine the absolute configuration of amino acids. Reaction of the amine moiety with 2 equivalents of 2-Br-quinoline followed by complexation to Cu(II) leads to intense ECCD. The sign of the dihedral angle between the chromophores correlates with the identity of the stereogenic center of the amino acid.



Canary extended his method from amino acids to chiral amines using a similar derivatization and metal complexation strategy to form **1.7** (Scheme 1.5).<sup>46</sup> However, in comparison to the amino acid Cu(II)-quinoline derivative, the amplitude of the Cotton effects are smaller.



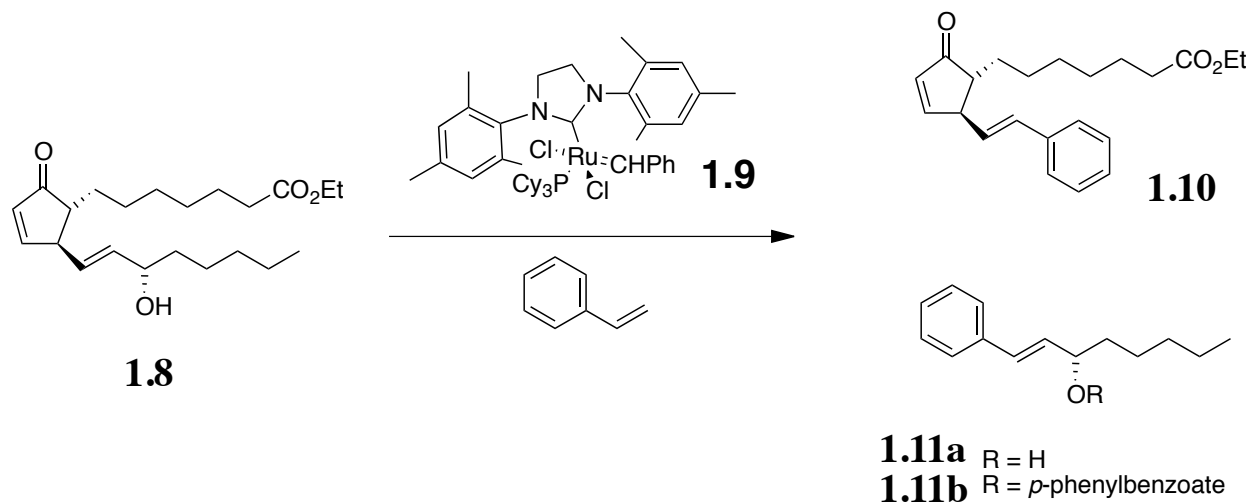
### **1.7**

Scheme 1.5. An extension of the original Canary system from amino acids to primary amines. The sign of the dihedral angle correlates with the sign of the ECCD couplet. However, the amplitude of the ECCD is much smaller than those of the similar amino acid adducts.

### **1.3.3 Allylic Alcohols**

Berova *et al.* showed the utility of the metathesis reaction in the determination of the absolute configuration of allylic alcohols. Prostaglandin **1.8** was converted to **1.10** and **1.11a** by reaction with styrene and Grubbs' catalyst **1.9** (Scheme 1.6). The coupling of the enone and the styrenoid chromophore allows for assignment of absolute configuration to **1.10**. **1.11a** required the introduction of a second chromophore. Incorporation of the chromophore was done by

reaction of the alcohol with *p*-phenylbenzoic acid to give **1.11b**. Coupling between the *p*-phenylbenzoate and styrene allowed for the assignment of absolute configuration of the alcohol.



Scheme 1.6. The method used by Berova *et al.* in the determination of absolute configuration of allylic alcohols.

#### 1.4 ECCD BY SUPRAMOLECULAR RECOGNITION OF THE ANALYTE

There are several drawbacks to the irreversible covalent modification of analytes prior to the determination of *ee* or absolute configuration by ECCD. In the case of rapid *ee* determination, covalent modification requires extra time for preparation of the analyte and, in most cases, an additional purification step. In the determination of absolute configuration, covalent modification wastes material. Thus, the use of supramolecular hosts for sensing chirality with ECCD is an attractive alternative.

Supramolecular ECCD based methods for the detection of chirality are reviewed below. Several of the hosts reviewed use reversible covalent bond formation. While these systems are not technically based on supramolecular interactions, they possess the same advantages as supramolecular systems, namely, the host-guest interactions are reversible and dynamic.

### 1.4.1 Qualitative Overview of Host-Guest Energetics for ECCD induction

Several groups have developed host systems capable of ECCD upon binding of a chiral analyte.<sup>10</sup> The majority of systems developed are capable of ECCD upon binding bidentate but not monodentate analytes. Bidentate analytes are well suited for inducing ECCD in supramolecular hosts because they are capable of having simultaneous favorable interactions with two chromophores. The favorable interactions provide a thermodynamic incentive for the chromophores to remain in proximity to one another and to the stereogenic center, which would otherwise be sterically disfavored (Figure 1.4). Close proximity of the chromophores to one another and to the stereogenic center results in more efficient induction of dissymmetry and exciton coupling.

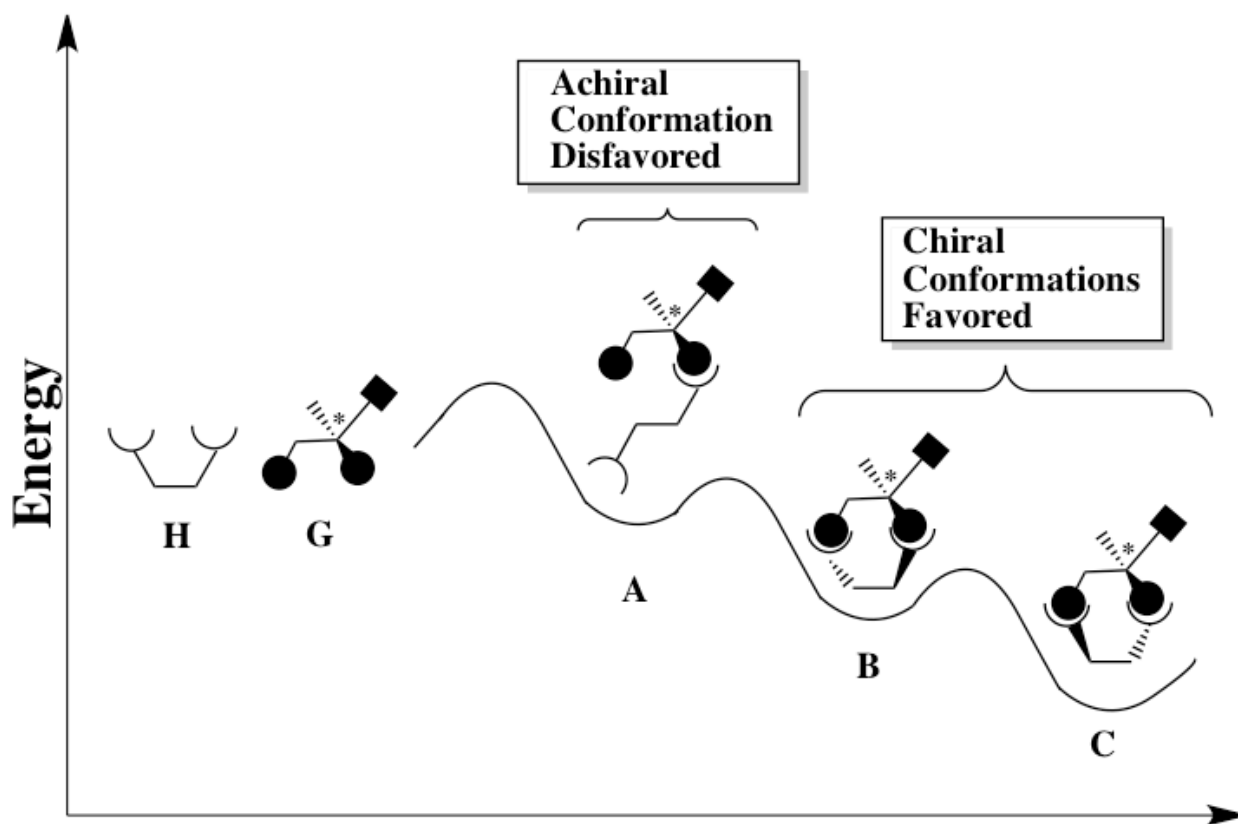


Figure 1.4. A hypothetical potential energy diagram for a host, H, and a bidentate guest G. The anti conformer A is highest in energy because it only has one favorable interaction with the analyte. The syn conformers B and C are lower in energy than A because each has two favorable interactions between H and G. The difference in energy between B and C is arbitrary and illustrates that differentiation between B and C is possible only if it is energetically favorable to populate the syn conformer.

Because a single monodentate analyte cannot bind two chromophores simultaneously, the chromophores have no energetic incentive to remain in a rigid disymmetric conformation. Instead, the chromophores can freely rotate into less sterically encumbered conformations where interactions with the stereogenic center are less likely. This typically results in weak asymmetric induction into the host, and thus, weak ECCD signals. (Figure 1.6).

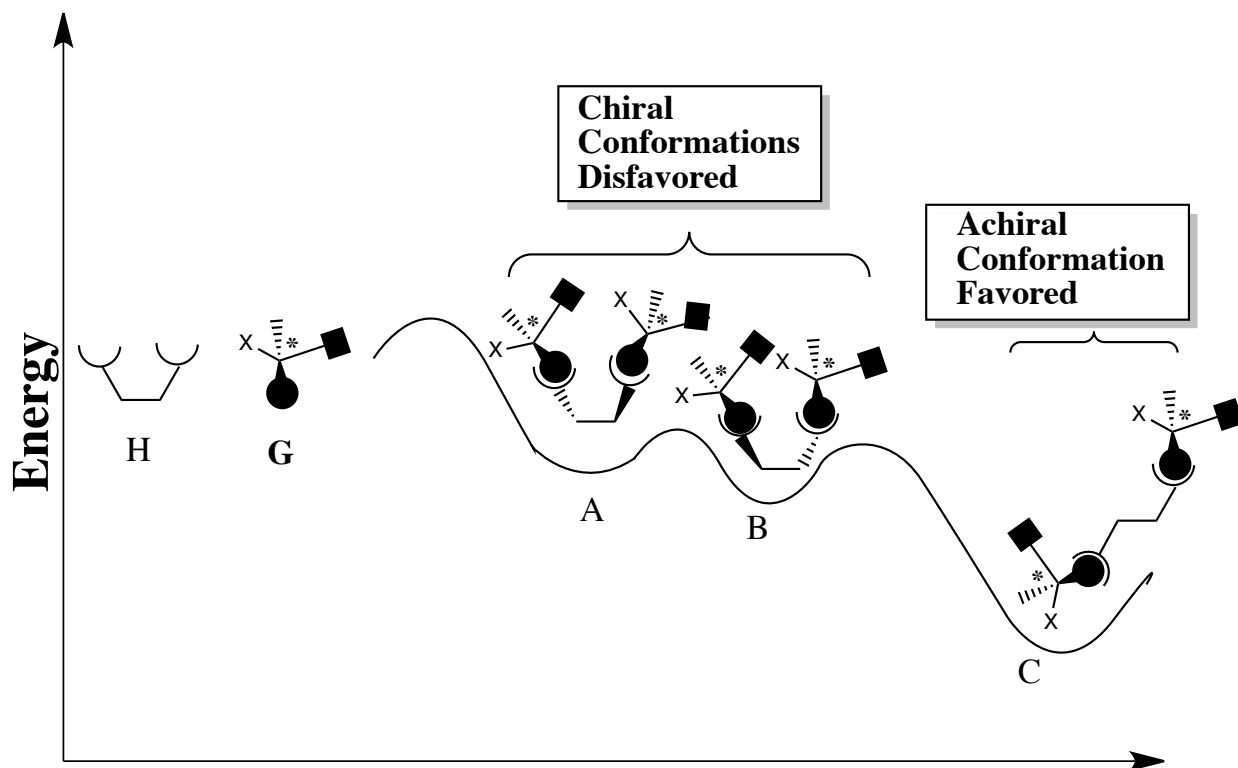


Figure 1.5. A hypothetical potential energy diagram for a host, H, and a monodentate guest G. The syn conformers A and B are higher in energy than the anti conformer C because they possess the same number of favorable interactions with the G, but are more sterically strained. The energy difference between A and B is of little consequence since C would be the most populated state.

## 1.5 SUPRAMOLECULAR ECCD METHODS FOR SENSING CHIRAL AMINES

Chiral amines are an important class of functional group because of their utility as building blocks in chemical and pharmaceutical transformations.<sup>30</sup> Thus, methods for the determination of their absolute configuration and *ee* are desirable.

### 1.5.1 Porphyrin Tweezers

The most popular supramolecular hosts for ECCD sensing are porphyrin tweezers.<sup>47-51</sup> Porphyrin tweezers typically consist of two porphyrins connected by an alkyl spacer.<sup>10,47-51</sup> The porphyrin tweezers are achiral but become disymmetrically oriented upon binding a chiral

analyte making them ECCD active.<sup>10,47-51</sup> Porphyrin systems are most commonly employed for the determination of absolute configuration.

The popularity of porphyrin tweezers is due to the amenability of the porphyrin chromophore to ECCD. Porphyrins have high absorption coefficients and large electric transition moments that can couple at distances over 50Å making them ideal for exciton coupling.<sup>10</sup>

Nakanishi *et al.* reported the first example of ECCD induction in a porphyrin tweezer.<sup>47</sup> The tweezer is capable of binding a chiral diamine and inducing an asymmetric conformational bias in the porphyrins leading to an ECCD couplet. The conformational bias arises from steric interactions that favor a negative or positive dihedral angle between the porphyrins. The sign of the dihedral angle is dependent on whether the stereogenic center identity is *R* or *S*. According to Nakanishi's model, the dihedral angle is positive for diamines with *S* stereochemistry because it is sterically unfavorable for the porphyrins to twist in the opposite direction (Figure 1.7).

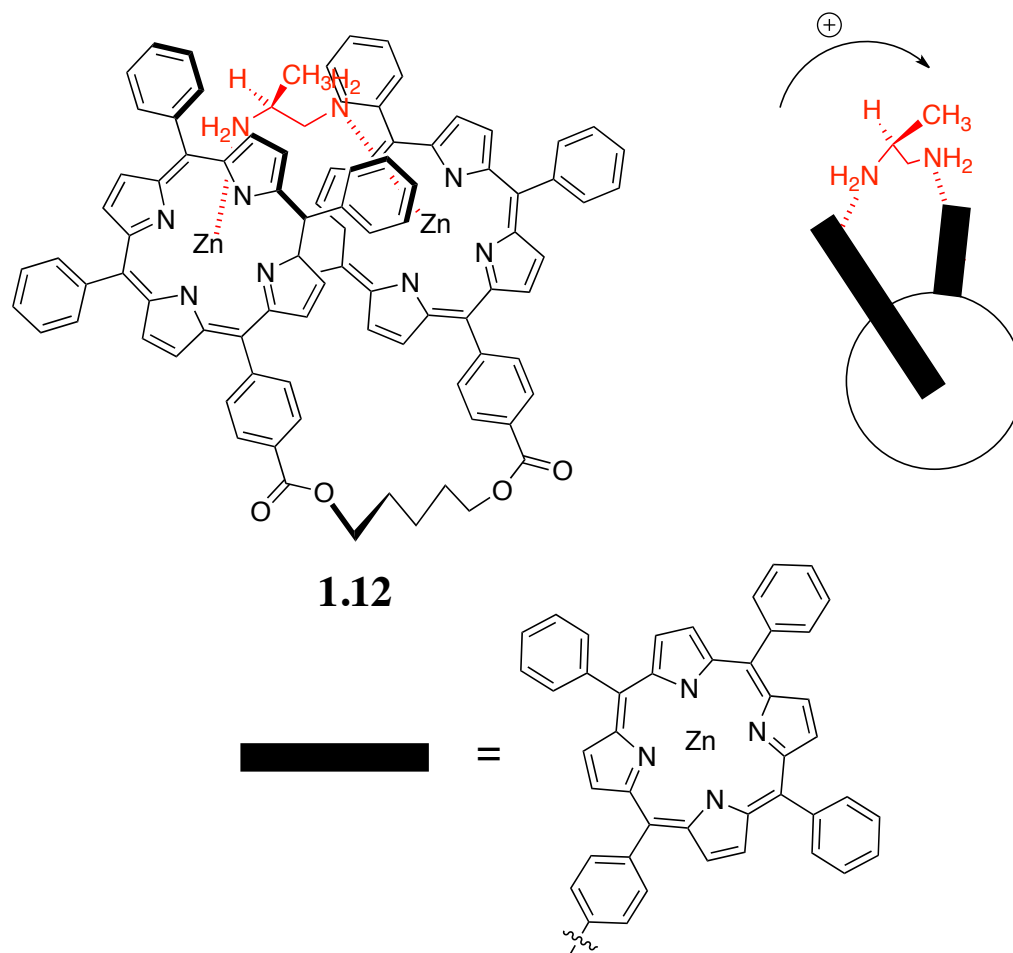
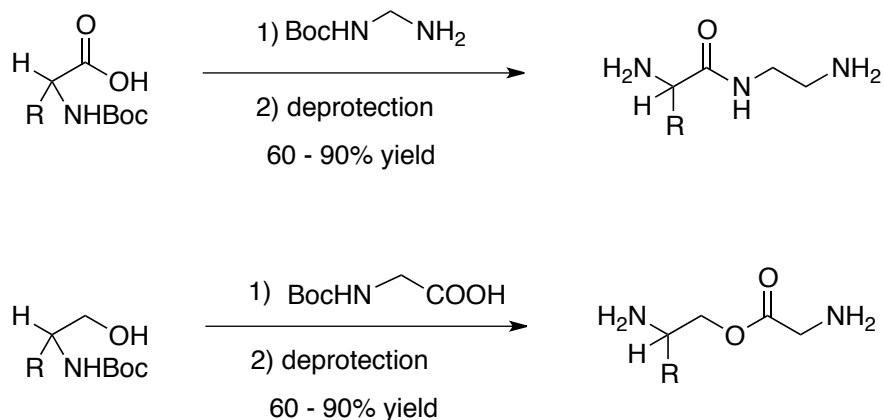


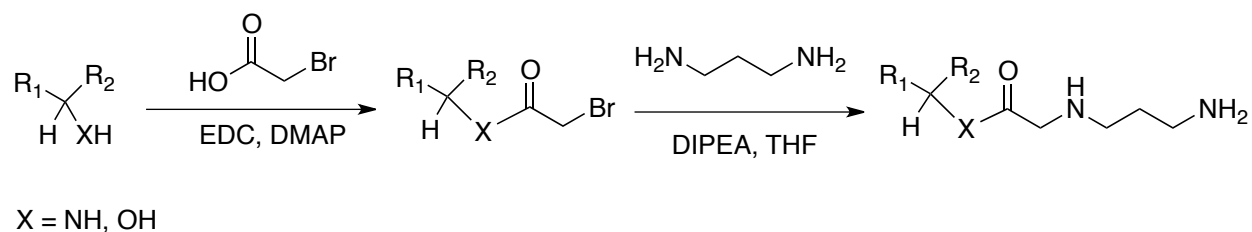
Figure 1.6. The porphyrin tweezer developed by Nakanishi *et al.* Binding of diamines results in complex **1.12**. The dissymmetric restriction of the chromophores leads to ECCD.

The method can also be used to sense chirality in amino acids and amino alcohols, if the carboxylic acid or alcohol is first derivatized in two steps with ethylene diamine or glycine, respectively (Scheme 1.7).<sup>47</sup>



Scheme 1.7. The two step derivatization method for amino acids and amino alcohols used by Nakanishi.

Later reports demonstrated the utility of tweezer **1.12** in the determination of chiral primary amines and secondary monoalcohols, if the amines and alcohols are first converted into diamines using a derivatizing agent (Scheme 1.6).<sup>48,49</sup>



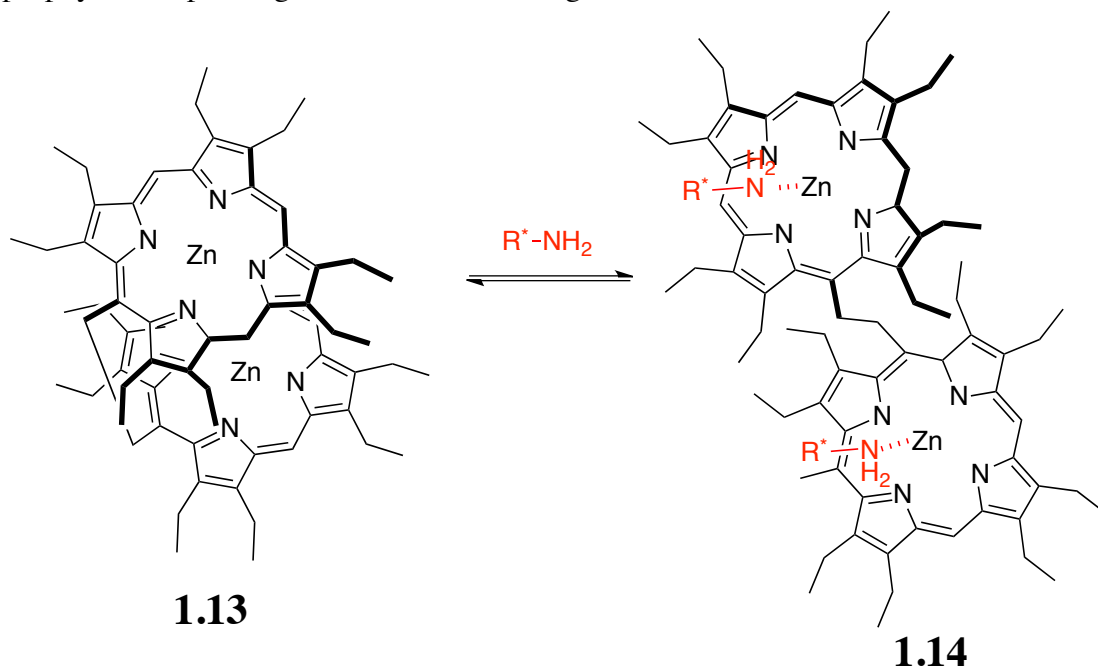
Scheme 1.8. The method used by Nakanishi to derivatize primary chiral amines.

The use of a covalent derivatization method followed by complexation to a supramolecular host suffers from the same drawbacks as the introduction of chromophores to analytes *via* covalent modifications.

In order to extend the use of porphyrin tweezer to primary amines without the need for covalent modification, Inoue *et al.* developed porphyrin tweezer host **1.13** (Scheme 1.9).<sup>52,53</sup> Tweezer **1.13** has a short ethane spacer and prefers the syn conformation due to favorable  $\pi$ - $\pi$  stacking interactions between the porphyrins. Binding of a chiral amine to one of the porphyrins causes the porphyrin tweezer to open up into an anti conformation. A second chiral amine can



bind to the other porphyrin to form complex **1.14**, which results in weak asymmetric induction into the tweezer system as evidenced by the small amplitudes of the Cotton effects. According to Inoue, chirality is induced into the porphyrin tweezer by unfavorable steric interactions between the bulkiest group of the stereogenic center and the ethane groups of the neighboring porphyrin causing a small preference for a positive or negative helical preference between the porphyrins, depending on the absolute configuration of the amine.



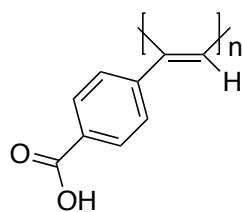
Scheme 1.9. Inoue's porphyrin tweezer system for determining the absolute configuration of underivatized primary amines. The tweezer opens up from the syn conformation to the anti conformation upon binding a chiral amine.

### 1.5.2 Polyacetylene Host

Polyacetylene **1.15** was used by Okamoto *et al.* in chirality sensing of primary amines and amino alcohols (Figure 1.8).<sup>54</sup> The acid-base complexation of the amino group with the carboxylic acid results in the induction of a preferred helicity in the polyacetylene, which gives

an ECCD couplet. The amplitude of the Cotton effects of the induced ECCD signal upon binding of a chiral primary amine varied directly with the steric size of the groups surrounding the stereogenic center of the amine, although the signals were always fairly small. The authors propose a binding model where the large group is directed away from the polymer (Figure 1.8). While this is likely the most energetically favorable conformation, it is difficult to use this model to rationalize how asymmetry is translated from the large group to the polymer.

For amino alcohols, there is no correlation between sterics and the amplitude of the Cotton effect. Amino alcohols always yield ECCD signals that are as high as primary sterically encumbered amines, regardless of the steric bulkiness of the ligand. The authors attribute this enhanced chirality induction to an additional hydrogen bonding interaction between the alcohol and the carboxylic acid, which would not be present in primary amines (Figure 1.9).



## 1.15

Figure 1.7. The polyacetylene polymer host used by Okamoto for the sensing of chiral primary amines and amino alcohols.

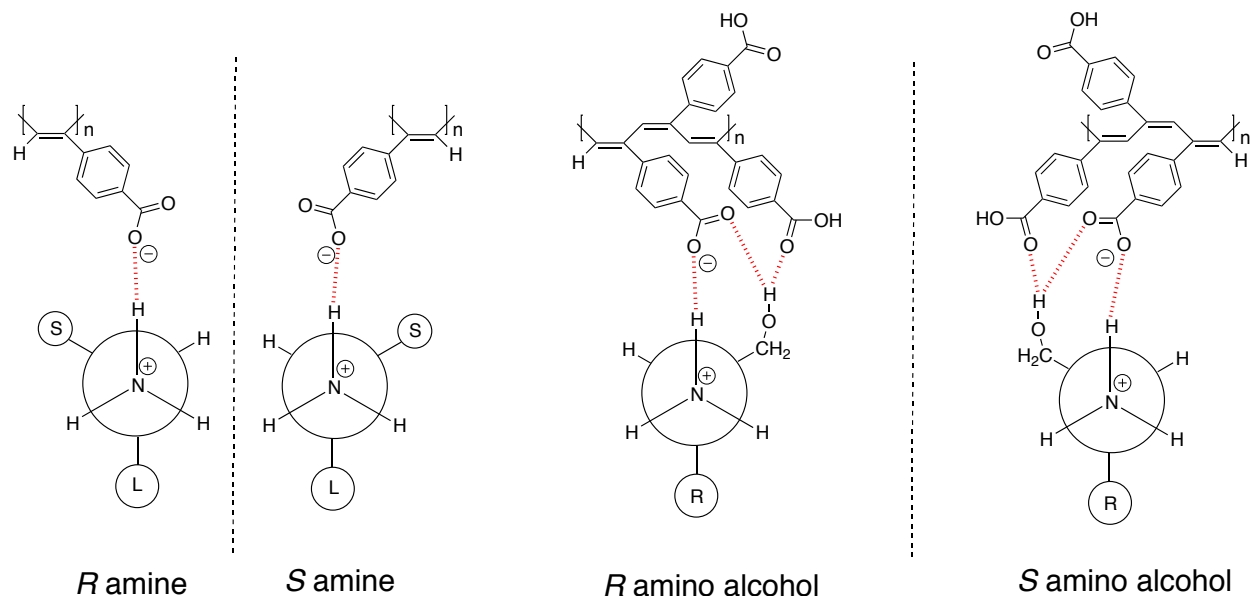


Figure 1.8. The binding mode proposed by Okamoto for recognition of chiral primary amines by polyacetylene **1.15**. The large group points away from the polymer, and the model proposed by Okamoto *et al.* for asymmetric induction from amino alcohols to polyacetylene **1.15**. The alcohol provides an additional interaction with the polymer.

### 1.5.3 Aldehyde and Ketone Based Sensors

Chin *et al.* reported the use of a ketone-based sensor for amino acid chirality (Figure 1.10).<sup>55</sup> The ketone is flanked by hydroxyl groups, which activate it towards nucleophilic attack facilitating imine formation. The imine and carboxylic acid act as acceptors for hydrogen bonds from the two phenol groups creating a dissymmetric twist in the chromophores allowing for ECCD. The dihedral angle between the chromophores varies predictably with the chirality at the stereogenic center. L and D amino acids impart a positive or negative dihedral angle between the chromophores, respectively. However, there was no correlation between sterics and the amplitude of the Cotton effects. Regardless of the steric size of the side chains, the amino acids all had Cotton effects of similar amplitude. Based on crystal structures and computational methods, the authors concluded that the asymmetric twist is induced *via* hydrogen bonding between the carboxylate and the phenol making the system insensitive to the sterics of the side

chain. It was also shown that if the amplitude of the CD signal for the valine adduct **1.17** at 360nm was plotted as a function of *ee*, there was a linear relationship suggesting that the sensor might have applications in the determination of *ee* for amino acids. However, no unknown samples were tested, and thus, no error was reported for the system.

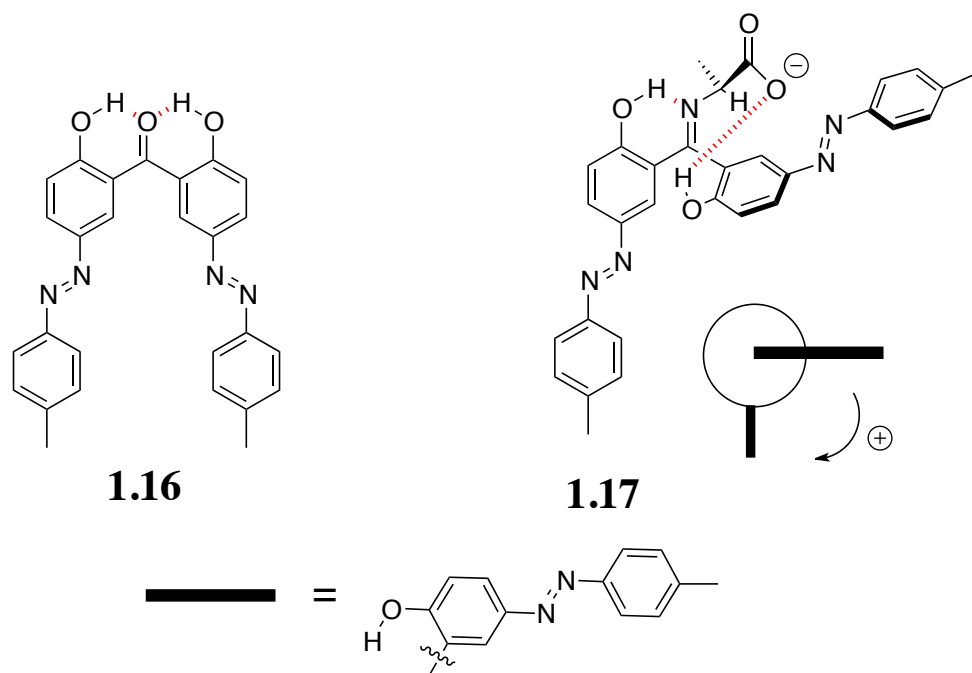
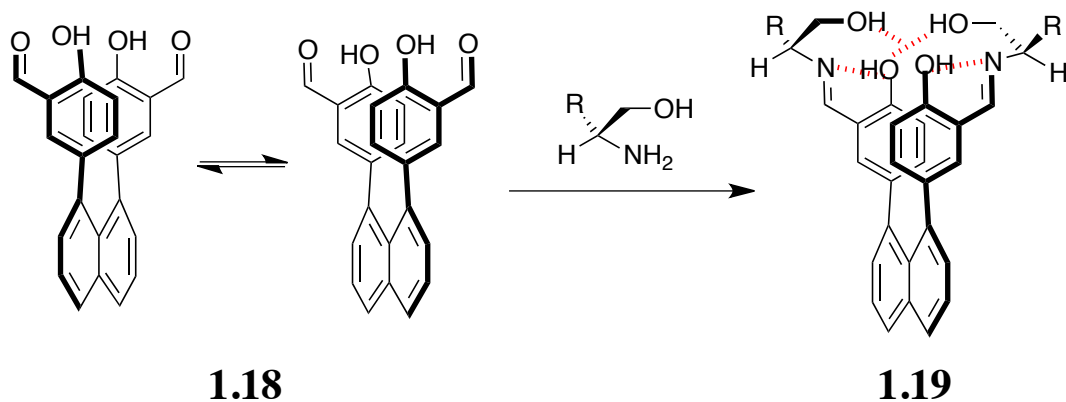


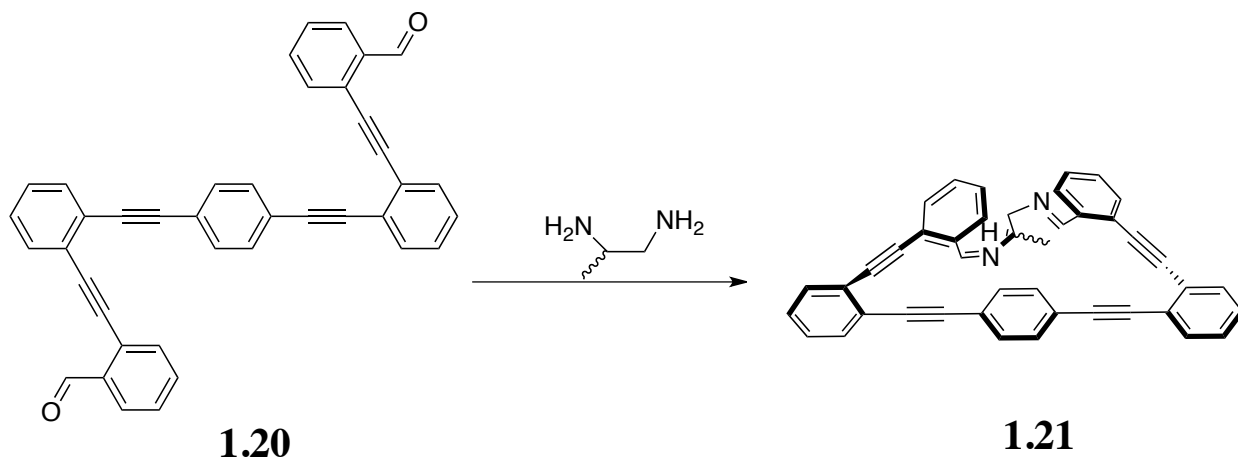
Figure 1.9. The ketone host used by Chin *et al.* for amino acid recognition. L- amino acids induce a positive helical twist *via* hydrogen bonding (shown in red) between the carboxylate and the phenol.

Wolf *et al.* used a similar approach for the determination of the absolute configuration and *ee* of amino alcohols.<sup>41,54</sup> Triaryl probe **1.18** was used, which reacts with two equivalents of amine to form a diimine (Scheme 1.10). Extensive hydrogen bonding in the imine derivative of the probe creates a preponderance of one helical conformation over another leading to ECCD.



Scheme 1.10. The biaryl host used by Wolf *et al.* for sensing amino alcohols. **1.19** exists as an equal mixture of conformational isomers. Reaction of the host with an enantiomerically pure amino alcohol leads adduct **1.19**, which has extensive hydrogen bonding (in red) and favors one helical isomer.

Another report by Wolf uses aryl acetylene host **1.20** to sense chirality in mono and diamines (Scheme 1.11).<sup>56</sup> Reaction of **1.20** with diamines produces the rigid imine cycle **1.21**. The topology of **1.21** is controlled by the chirality of the diamine and leads to ECCD between the aryl groups. Reaction of **1.20** with monoamines leads to a conformationally flexible host-guest system and thus, the amplitude of the Cotton effects are much smaller. The system could be used to determine *ee* with an average absolute error of approximately 5%.



Scheme 1.11. The aryl probe used by Wolf *et al.* to sense chirality in diamines. Upon reaction with a diamine the host becomes conformationally locked.

## 1.6 SUMMARY AND GOALS

Other groups have examined the use of induced CD in metals as an empirical method for the determination of absolute configuration. We recently reported a system (scheme 1.1), which demonstrated the potential of metals in the determination of *ee*. The work in this thesis addresses those limitations and expands the scope of simple metal-based CD systems in the determination of *ee*.

Additionally, while a number of ECCD based supramolecular systems exist for sensing chirality in bidentate amine analytes<sup>41,47-49,52-54,56</sup> such as amino acids, diamines, and amino alcohols, few systems are capable of ECCD upon binding monodentate primary amines. Porphyrin tweezer **1.13**,<sup>47</sup> polyacetylene **1.15**<sup>54</sup> and aryl probe **1.20**<sup>56</sup> are some of the best examples of hosts capable of ECCD upon binding primary amines. However, all of these systems suffer from poor translation of the chirality from the monodentate guest to the host molecules as evidenced by their weak induced ECCD signals. The weak induction of chirality and requirement of synthetic effort limits the practical utility of these systems in the determination of absolute configuration. The research described in this thesis attempts to address this problem.

## 1.7 OTHER THESIS TOPICS

While the majority of this thesis focuses on the CD determination of absolute configuration and *ee* of chiral primary amines, there is one chapter that deviates from this topic. A brief introduction to this new topic is provided at the beginning of this chapter.

## 1.8 REFERENCES

- (1) Oikawa, H.; Ichihara, A.; Sakamura, S. *Agr Biol Chem Tokyo* 1984, 48, 2603.
- (2) Margolin, A. L. *Enzyme Microb Tech* 1993, 15, 266.
- (3) Harada, N.; Saito, A.; Ono, H.; Murai, S.; Li, H. Y.; Gawronski, J.; Gawronska, K.; Sugioka, T.; Uda, H. *Enantiomer* 1996, 1, 119.

- (4) Caner, H.; Groner, E.; Levy, L.; Agranat, I. *Drug Discov Today* 2004, 9, 105.
- (5) Boeckman, R. K.; Ferreira, M. D. R.; Mitchell, L. H.; Shao, P. C. *J Am Chem Soc* 2002, 124, 190.
- (6) Benohoud, M.; Leman, L.; Cardoso, S. H.; Retailleau, P.; Dauban, P.; Thierry, J.; Dodd, R. H. *J Org Chem* 2009, 74, 5331.
- (7) Batista, J. M.; Batista, A. N. L.; Rinaldo, D.; Vilegas, W.; Ambrosio, D. L.; Cicarelli, R. M. B.; Bolzani, V. S.; Kato, M. J.; Nafie, L. A.; Lopez, S. N.; Furlan, M. J. *Nat Prod* 2011, 74, 1154.
- (8) Adam, W.; Lukacs, Z.; Viebach, K.; Humpf, H. U.; Saha-Moller, C. R.; Schreier, P. *J Org Chem* 2000, 65, 186.
- (9) Anslyn, E. V.; Dougherty, D. A. *Modern physical organic chemistry*; University Science: Sausalito, CA, 2006.
- (10) Nakanishi; Woody, R. W. *Circular Dichroism: Principles and Applications*; Wiley-VCH, 2000.
- (11) Furusaki, A.; Shiraham, H.; Matsumoto, T. *Chem Lett* 1973, 1293.
- (12) Cai, G. L.; Bozhkova, N.; Odingo, J.; Berova, N.; Nakanishi, K. *J Am Chem Soc* 1993, 115, 7192.
- (13) Stambuli, J. P.; Hartwig, J. F. *Curr Opin Chem Biol* 2003, 7, 420.
- (14) Shimizu, K. D.; Snapper, M. L.; Hoveyda, A. H. *Chem-Eur J* 1998, 4, 1885.
- (15) Shabbir, S. H.; Regan, C. J.; Anslyn, E. V. *P Natl Acad Sci USA* 2009, 106, 10487.
- (16) Shabbir, S. H.; Joyce, L. A.; da Cruz, G. M.; Lynch, V. M.; Sorey, S.; Anslyn, E. V. *J Am Chem Soc* 2009, 131, 13125.
- (17) Reetz, M. T. *Angew Chem Int Edit* 2002, 41, 1335.
- (18) Reetz, M. T.; Kuhling, K. M.; Deege, A.; Hinrichs, H.; Belder, D. *Angew Chem Int Edit* 2000, 39, 3891.
- (19) Reetz, M. T.; Becker, M. H.; Liebl, M.; Furstner, A. *Angew Chem Int Edit* 2000, 39, 1236.
- (20) Pescarmona, P. P.; van der Waal, J. C.; Maxwell, I. E.; Maschmeyer, T. *Catal Lett* 1999, 63, 1.
- (21) Finn, M. G.; Guo, J.; Keller, K. A. *Abstr Pap Am Chem S* 2000, 219, U776.
- (22) van Delden, R. A.; Feringa, B. L. *Chem Commun* 2002, 174.
- (23) van Delden, R. A.; Feringa, B. L. *Angew Chem Int Edit* 2001, 40, 3198.
- (24) Eelkema, R.; van Delden, R. A.; Feringa, B. L. *Angew Chem Int Edit* 2004, 43, 5013.
- (25) Zhu, L.; Zhong, Z. L.; Anslyn, E. V. *J Am Chem Soc* 2005, 127, 4260.

- (26) Xu, K. X.; He, Y. B.; Qin, H. J.; Qing, G. Y.; Liu, S. Y. *Tetrahedron-Asymmetr* 2005, 16, 3042.
- (27) Wolf, C.; Liu, S. L.; Reinhardt, B. C. *Chem Commun* 2006, 4242.
- (28) Pagliari, S.; Corradini, R.; Galaverna, G.; Sforza, S.; Dossena, A.; Montalti, M.; Prodi, L.; Zaccheroni, N.; Marchelli, R. *Chem-Eur J* 2005, 11, 7145.
- (29) Pagliari, S.; Corradini, R.; Galaverna, G.; Sforza, S.; Dossena, A.; Montalti, M.; Prodi, L.; Zaccheroni, N.; Marchelli, R. *Chem-Eur J* 2004, 10, 2749.
- (30) Nieto, S.; Lynch, V. M.; Anslyn, E. V.; Kim, H.; Chin, J. *J Am Chem Soc* 2008, 130, 9232.
- (31) Leung, D.; Folmer-Andersen, J. F.; Lynch, V. M.; Anslyn, E. V. *J Am Chem Soc* 2008, 130, 12318.
- (32) Leung, D.; Anslyn, E. V. *J Am Chem Soc* 2008, 130, 12328.
- (33) Heinrichs, G.; Schellentrager, M.; Kubik, S. *Eur J Org Chem* 2006, 4177.
- (34) Dillon, J.; Nakanish.K *J Am Chem Soc* 1974, 96, 4055.
- (35) Nakanish.K; Schooley, D. A.; Koreeda, M.; Dillon, J. *Journal of the Chemical Society D-Chemical Communications* 1971, 1235.
- (36) Dillon, J.; Nakanishi, K. *J Am Chem Soc* 1975, 97, 5409.
- (37) Dillon, J.; Nakanishi, K. *J Am Chem Soc* 1975, 97, 5417.
- (38) Dillon, J.; Nakanish.K *J Am Chem Soc* 1974, 96, 4059.
- (39) Harada, N.; Nakanish.K *J Am Chem Soc* 1969, 91, 3989.
- (40) Mitchell, G. N.; Carroll, F. I. *J Am Chem Soc* 1973, 95, 7912.
- (41) Ghosn, M. W.; Wolf, C. *J Am Chem Soc* 2009, 131, 16360.
- (42) Liu, S. L.; Wolf, C. *Org Lett* 2007, 9, 2965.
- (43) Matile, S.; Berova, N.; Nakanishi, K.; Novkova, S.; Philipova, I.; Blagoev, B. *J Am Chem Soc* 1995, 117, 7021.
- (44) Holmes, A. E.; Zahn, S.; Canary, J. W. *Chirality* 2002, 14, 471.
- (45) Zahn, S.; Canary, J. W. *Org Lett* 1999, 1, 861.
- (46) Zhang, J.; Holmes, A. E.; Sharma, A.; Brooks, N. R.; Rarig, R. S.; Zubieta, J.; Canary, J. W. *Chirality* 2003, 15, 180.
- (47) Huang, X. F.; Rickman, B. H.; Borhan, B.; Berova, N.; Nakanishi, K. *J Am Chem Soc* 1998, 120, 6185.
- (48) Kurtan, T.; Nesnas, N.; Koehn, F. E.; Li, Y. Q.; Nakanishi, K.; Berova, N. *J Am Chem Soc* 2001, 123, 5974.
- (49) Kurtan, T.; Nesnas, N.; Li, Y. Q.; Huang, X. F.; Nakanishi, K.; Berova, N. *J Am Chem Soc* 2001, 123, 5962.
- (50) Li, X. Y.; Borhan, B. *J Am Chem Soc* 2008, 130, 16126.



- (51) Li, X. Y.; Tanasova, M.; Vasileiou, C.; Borhan, B. *J Am Chem Soc* 2008, 130, 1885.
- (52) Borovkov, V. V.; Lintuluoto, J. M.; Inoue, Y. *J Am Chem Soc* 2001, 123, 2979.
- (53) Borovkov, V. V.; Lintuluoto, J. M.; Sugeta, H.; Fujiki, M.; Arakawa, R.; Inoue, Y. *J Am Chem Soc* 2002, 124, 2993.
- (54) Yashima, E.; Matsushima, T.; Okamoto, Y. *J Am Chem Soc* 1997, 119, 6345.
- (55) Kim, H.; So, S. M.; Yen, C. P. H.; Vinhato, E.; Lough, A. J.; Hong, J. I.; Kim, H. J.; Chin, J. *Angew Chem Int Edit* 2008, 47, 8657.
- (56) Iwaniuk, D. P.; Wolf, C. *J Am Chem Soc* 2011, 133, 2414.

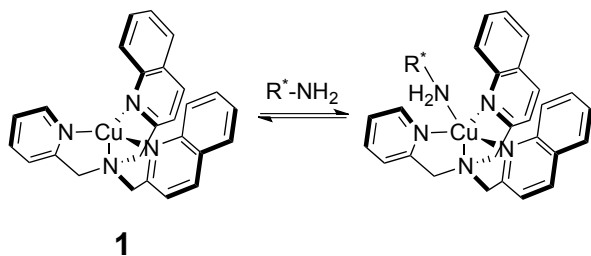
## Chapter 2: Supramolecular ECCD Method for Determining Absolute Configuration of $\alpha$ -Chiral Primary Amines

### 2.1 INTRODUCTION

As previously discussed, Canary *et al.* reported an ECCD method for the determination of the absolute configuration of primary amines.<sup>1</sup> The method depends on covalent modification of the amine group followed by reaction with Cu(II) to form helically biased complex **1.7**. In collaboration with Canary, we sought to extend the use these helical complexes to the absolute configuration determination of amines without the need for covalent modification. Herein we report such a system.

#### 2.1.1 Design Criteria

Our goal was to create an ECCD based supramolecular method for determining the absolute configuration of monodentate  $\alpha$ -chiral primary amines. In order to address this challenge, achiral receptor **2.1** (Scheme 2.1) was prepared using previously reported methods.<sup>2</sup> It was predicted that primary amines would bind to the apical position of Cu(II) (Scheme 2.1). This binding mode would position the stereogenic center of the amine in proximity to the quinoline chromophores, and induce a twist to the quinoline chromophores *via* steric interactions.



Scheme 2.1. The receptor employed, **2.1**, and the predicted binding mode.

## 2.2 RESULTS AND DISCUSSION

### 2.2.1 Amines Studied

The five chiral amines in Figure 2.1 were chosen for study to demonstrate the generality of the system across different classes of chiral amines, namely, cyclic (**CHA**), aliphatic (**AHA**), bicyclic (**IPA**), and aromatic (**MBA and NBA**).

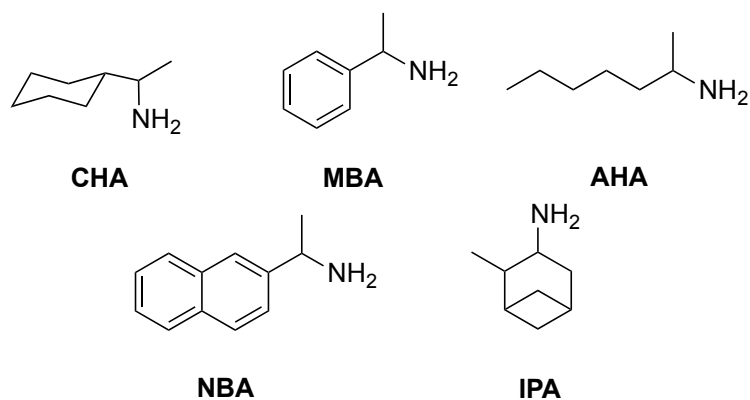


Figure 2.1. The chiral amines chosen for study.

### 2.2.2 Induction of ECCD

The addition of chiral amines to **2.1** induced ECCD in the quinoline chromophores as evidenced by the approximately coincident null in the ECCD couplet with the absorption maxima of the UV-vis spectrum (Figure 2.3). Only part of the second Cotton effect of the ECCD couplet can be seen due to interference from absorption of the solvent, methylene chloride. The first Cotton effect of the ECCD couplet appears between 235 and 241 nm, depending on the identity of the chiral amine (Table 2.1). The sign of the first Cotton effect of the ECCD signal varies predictably with the identity of the stereogenic center of the amine. *R*

and *S* enantiomers consistently yield negative and positive first Cotton effects, respectively, for all of the amines tested.

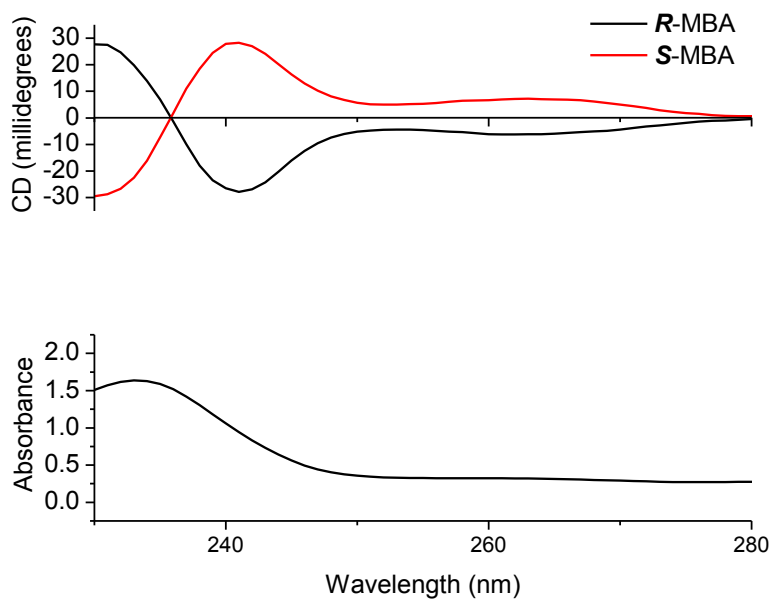


Figure 2.2. The CD and UV-vis spectra of **2.1-MBA** at 0.3mM of **2.1** and 0.6mM of **MBA** in methylene chloride in a 0.1cm quartz cell.

amine	$\lambda$ (nm)	CD (millidegrees)
<i>R</i> -CHA	241	-8.7
<i>S</i> -CHA	241	9.0
<i>R</i> -MBA	241	-27.8
<i>S</i> -MBA	241	28.3
<i>R</i> -AHA	240	-9.1
<i>S</i> -AHA	241	9.4
<i>R</i> -NBA	235	55.7
<i>S</i> -NBA	235	-47.3
<i>R</i> -IPA	240	21.8
<i>S</i> -IPA	240	-26.1

Table 2.1. A table showing the identity of the amine, the wavelength of first Cotton effect, and the sign and magnitude of the CD signal.

### 2.2.3 Model for Asymmetric Induction

Based on previously reported crystal structures from Canary *et al.*<sup>1,2</sup>, it was deduced that a negative or positive first Cotton effect is indicative of a  $\Lambda$  or  $\Delta$ , helicity in **2.1**. Thus, *R* and *S* chiral amines induce a  $\Lambda$  or  $\Delta$  helicity in receptor **2.1**, respectively. CPK model building led to the development of a simple model for chirality transfer from the chiral amine to **2.1** (Figure 2.4). For the host guest complex, the least sterically encumbered conformation, and thus most energetically favorable conformation, places the small substituent  $R_S$  in a staggered conformation in between the quinolines. This places the large and medium groups,  $R_L$  and  $R_M$ , on either side of the smaller pyridine substituent of the host. Unfavorable steric interactions between a proton on the quinoline and  $R_L$  make it favorable for the quinoline to twist away from  $R_L$  resulting in helical induction in the host-guest complex. In the case of the *R* enantiomer, this results in a negative helicity. Conversely, the *S* enantiomer induces a positive helicity.

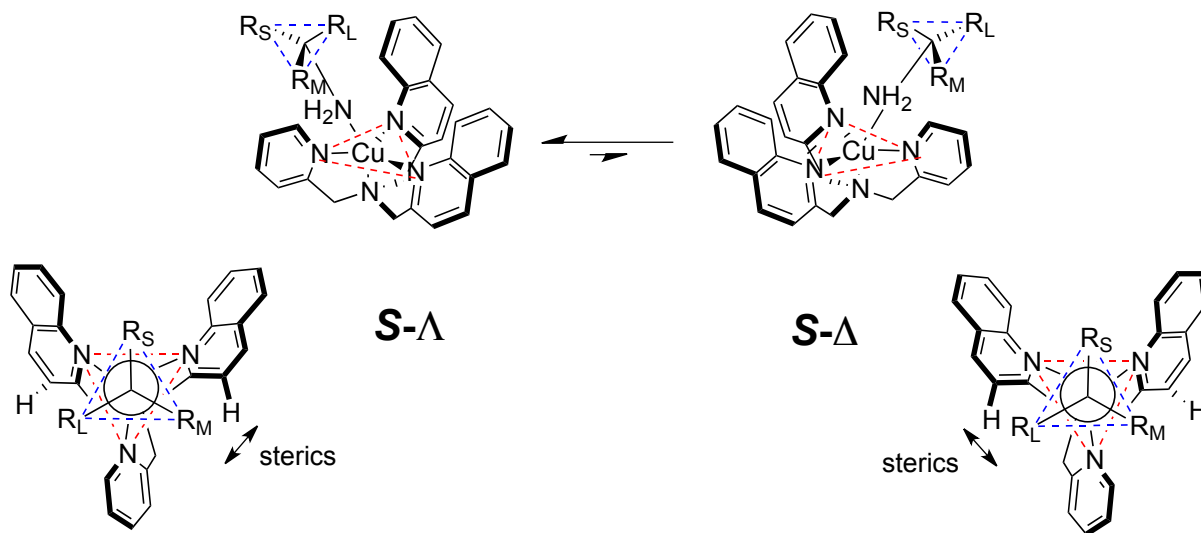


Figure 2.3. Two different views of the host-guest complex in equilibrium between the  $S-\Lambda$  and  $S-\Delta$  isomer. The equilibrium favors the  $S-\Lambda$  isomer because the steric interaction between the quinoline and  $R_M$  is less severe than the steric interaction between the quinoline and  $R_L$  in the  $S-\Delta$ .

## 2.2.4 Principal Component Analysis

Principal component analysis (PCA) is a useful technique for reducing complex multidimensional systems to a lower dimensionality projection. Here it is employed to visualize the relationship between the primary CD optical data and the identity and stereogenicity of the different amines studied. PCA allowed for the differentiation of the identity of most of the chiral amines as well as the handedness of the stereogenic center of the chiral amines (Figure 2.5). **CHA** and **AHA** were not separated in the PCA plot, which suggests that both induce a virtually identical conformational bias in the receptor.

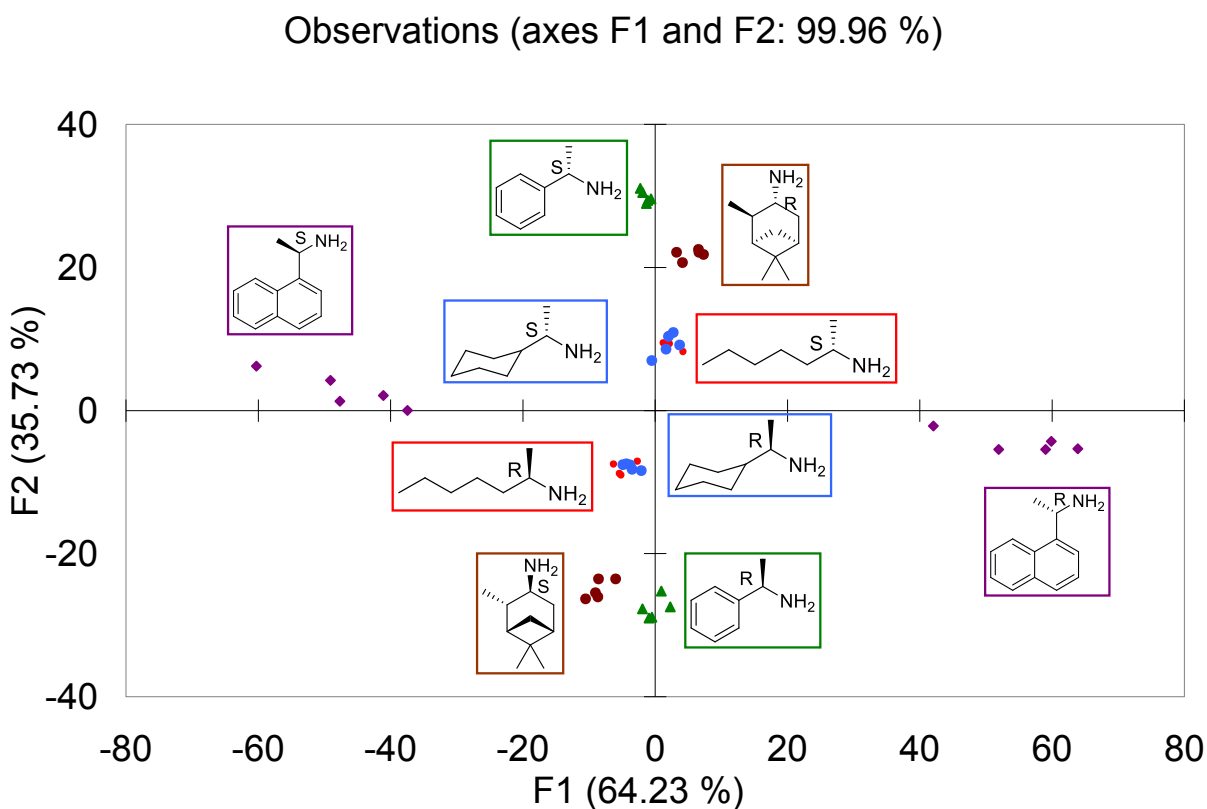


Figure 2.4. A PCA plot showing how the analytes separate across two axes. The primary optical data for the PCA plot was collected at 260, 240, and 235nm.

### 2.3 SUMMARY AND CONCLUSIONS

In summary, we demonstrate a novel method for the supramolecular induction of chirality into a helical Cu(II) complex. The helicity of the complex is reflected in the sign of the first Cotton effect of the ECCD couplet and varies predictably with the identity of the stereogenic center of the amine. A simple model based on steric interactions between the largest group on the amine stereogenic center and the quinoline group can be used to explain the mechanism of asymmetric induction. Analysis of the primary optical data by PCA allows for the separation of all of the amines by handedness and the identity of the groups on the stereogenic center, with the exception of **CHA** and **AHA**.

While host **2.1** is effective at detecting chirality, it suffers from several drawbacks. It requires synthetic effort, which is time-consuming, and sensor **2.1** absorbs in the ultra-violet region, and thus, suffers from interference from solvent. Thus, a method for sensing chirality in chiral amines that does not require synthetic effort and absorbs at higher wavelengths is preferable. These limitations are addressed in chapters 2 and 3.

Currently, the potential of host **2.1** in sensing other chiral analytes, such as chiral carboxylates, is being explored.

## 2.4 EXPERIMENTAL DETAILS

### 2.4.1 CD Spectra

All CD spectra were taken on a JASCO-815 CD Spectrometer in a 0.1cm cell at 0.3mM of **2.1** and 0.6mM of amine in methylene chloride. CD spectra for **2.1** complexed with **MBA**, **NBA**, **CHA**, **AHA**, and **IPA** are show in Figures 2.6, 2.7, 2.8, 2.9, and 2.10, respectively.

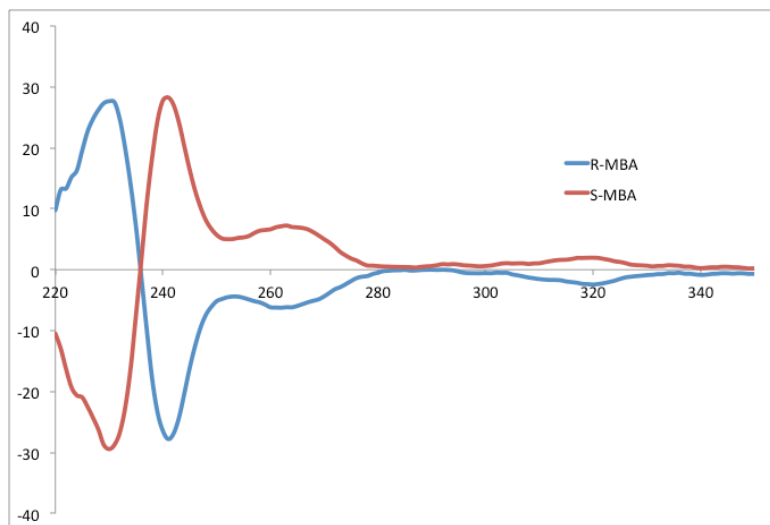


Figure 2.5. The CD spectrum of **2.1-MBA**



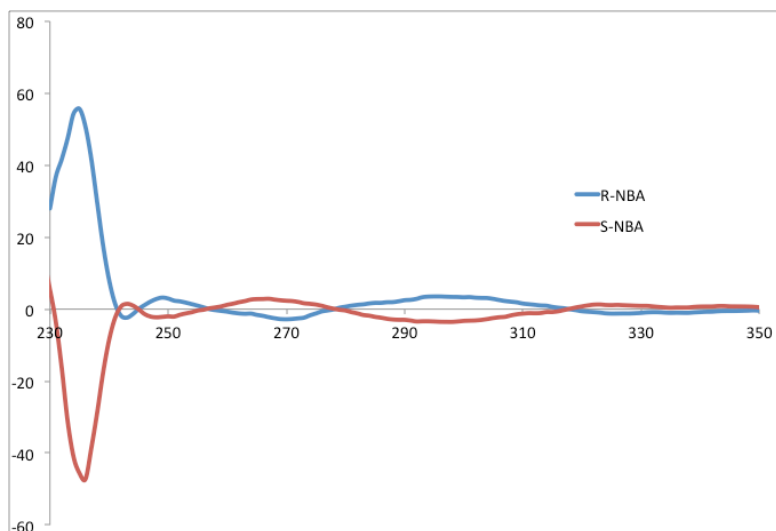


Figure 2.6. The CD spectrum of **2.1-NBA**

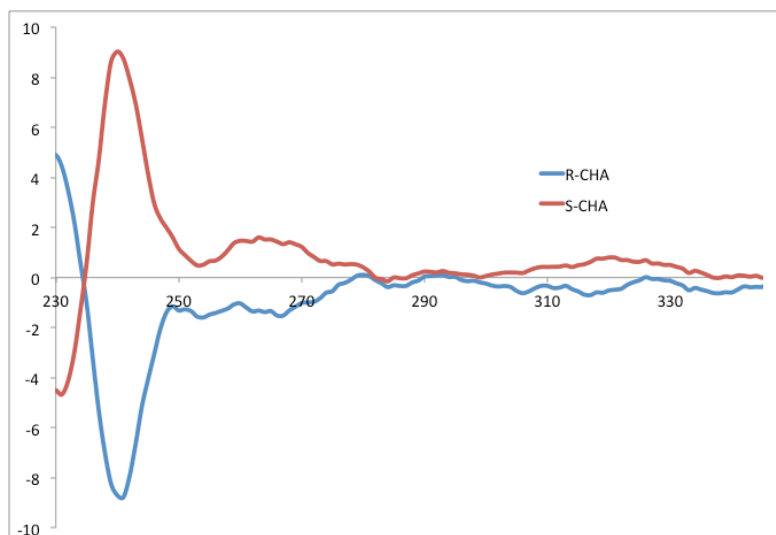


Figure 2.7. The CD spectrum of **2.1-CHA**

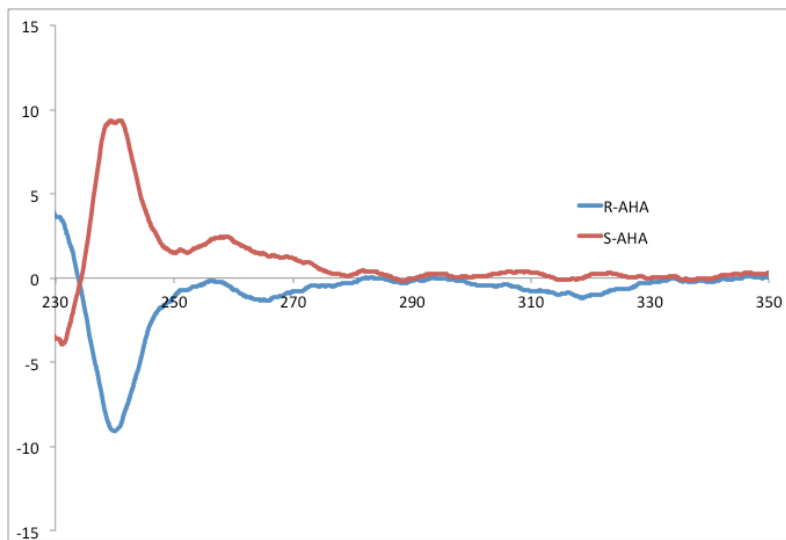


Figure 2.8. The CD spectrum of **2.1-AHA**

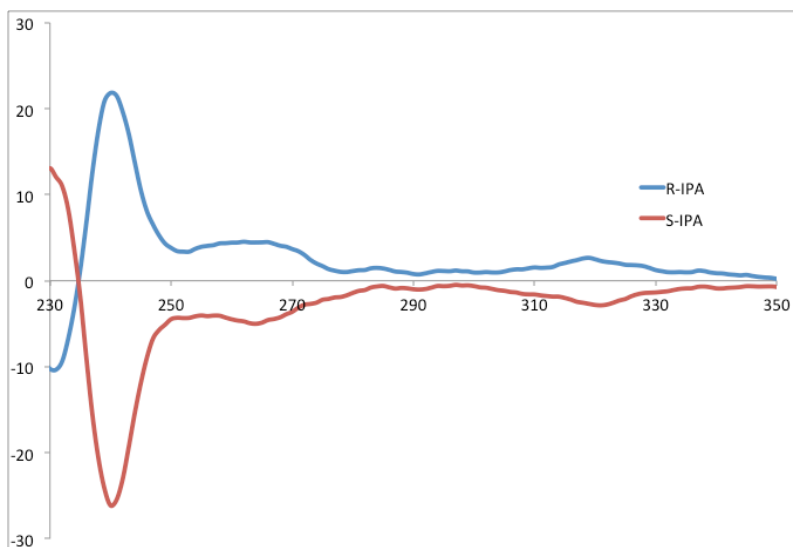


Figure 2.9. The CD spectrum of **2.1-IPA**

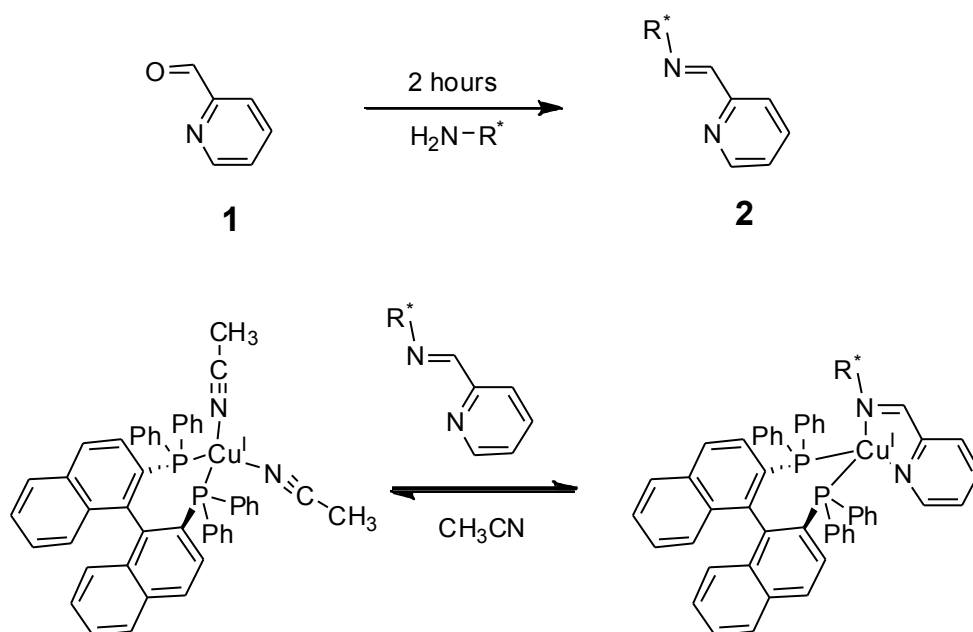
## 2.5 REFERENCES

- (1) Nieto, S.; Dragna, J. M.; Anslyn, E. V. *Chemistry – A European Journal* 2010, 16, 227.
- (2) Benohoud, M.; Leman, L.; Cardoso, S. H.; Retailleau, P.; Dauban, P.; Thierry, J.; Dodd, R. H. *The Journal of Organic Chemistry* 2009, 74, 5331.
- (3) Boeckman, R. K.; del Rosario Rico Ferreira, M.; Mitchell, L. H.; Shao, P. *Journal of the American Chemical Society* 2001, 124, 190.
- (4) Takamura, H.; Murata, T.; Asai, T.; Kadota, I.; Uemura, D. *The Journal of Organic Chemistry* 2009, 74, 6658.
- (5) Wu, H.; Xue, F.; Xiao, X.; Qin, Y. *Journal of the American Chemical Society* 2010, 132, 14052.
- (6) Kim, H.; So, S. M.; Yen, C. P.-H.; Vinhato, E.; Lough, A. J.; Hong, J.-I.; Kim, H.-J.; Chin, J. *Angewandte Chemie International Edition* 2008, 47, 8657.
- (7) Iwaniuk, D. P.; Wolf, C. *Journal of the American Chemical Society* 2011, 133, 2414.
- (8) Huang, X.; Rickman, B. H.; Borhan, B.; Berova, N.; Nakanishi, K. *Journal of the American Chemical Society* 1998, 120, 6185.
- (9) Zhang, J.; Holmes, A. E.; Sharma, A.; Brooks, N. R.; Rarig, R. S.; Zubieta, J.; Canary, J. W. *Chirality* 2003, 15, 180.
- (10) Holmes, A. E.; Zahn, S.; Canary, J. W. *Chirality* 2002, 14, 471.

## Chapter 3: Iron(II) and Aldehyde Sensing Ensemble for the Determination of Enantiomeric Excess and Absolute Configuration of $\alpha$ -Chiral Primary Amines

### 3.1 INTRODUCTION

As discussed in chapter 2, host **2.1** required synthetic effort and the host **2.1**-amine adduct absorbed in the ultraviolet region of the spectrum, which limits the utility of the assay in sensing chirality. Also, discussed in Chapter 1, we recently reported a CD protocol to determine *ee* and absolute configuration in  $\alpha$ -chiral primary amines using a carbonyl based derivatization and an organometallic receptor (Scheme 3.1).<sup>4</sup> This system also had several limitations. First, the imine formation was slow – it took two hours to go to completion. Second, the CD signal appeared in the UV and was of low intensity, resulting in a low signal-to-noise ratio. This led to moderately high errors in *ee* of  $\pm 12\%$ . Third, the system was not based on ECCD. Thus, while it was useful for determining *ee*, it was limited in its utility in the determination of absolute configuration. Lastly, the calibration curves were concentration dependent, and thus required the use of an artificial neural network to relate the CD data to *ee* values. However, this last problem likely could have been circumvented, if the assay was run above saturation. Herein we describe a CD method for the determination of *ee* and absolute configuration of primary amines that overcomes the limitations of our previous protocols.



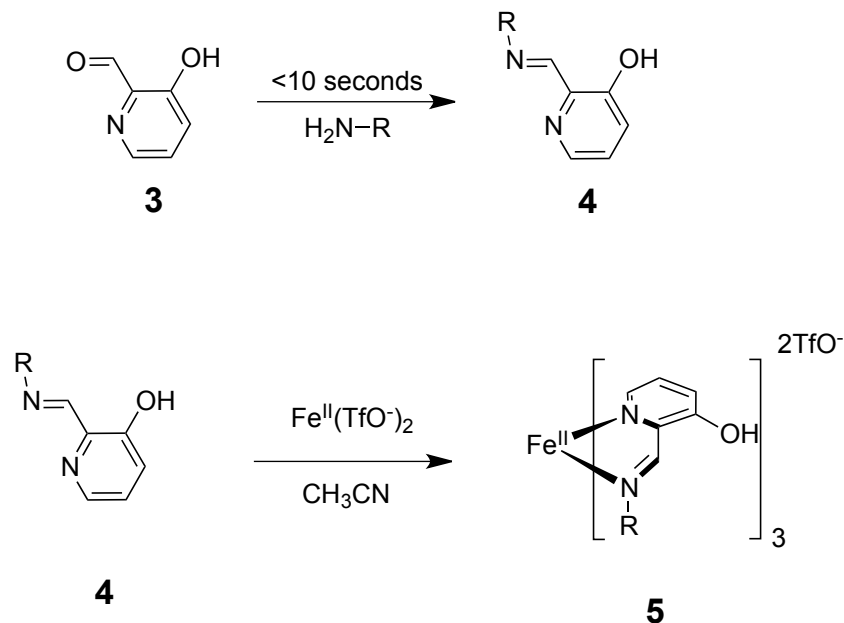
Scheme 3.1. The chiral Cu(I) receptor **3.1** and imine binding scheme for our previously reported protocol. A CD active charge transfer band is present in the receptor and is modulated upon binding of the imine.

### 3.1.1 Design Criteria

One goal was to develop an ECCD based assay that used commercially available components for the determination of absolute configuration and *ee* of  $\alpha$ -chiral primary amines in a rapid and accurate manner. The use of commercially available materials would eliminate the need for host synthesis, which would increase the assays' utility to the chemistry community at large. To this end, we envisioned an assay composed of a metal, Fe(II), used as a scaffold and colorimetric indicator; and an aldehyde, **3.2**, used as a chromophoric derivatizing agent that converts a monodentate amine to bidentate imine **3.3** (Scheme 3.2). Fe(II) was chosen because it has six binding sites, and thus, could potentially bring three equivalents of bidentate imine **3.3** into proximity to form **3.4**. We predicted that this would allow for coupling of the  $\pi$ - $\pi^*$  transitions giving an ECCD couplet in the UV, which could be used to determine absolute configuration. But in addition, Fe(II) is known to form CD active metal-to-ligand charge transfer

bands in the visible range of the spectrum, which could conceivably be used in conjunction with calibration curves to calculate the *ee* of unknown samples.

By using Fe(II) to bring several chromophoric imines into proximity, the envisioned system would overcome each of the limitations associated with our previously reported system, as now described.



Scheme 3.2. Aldehyde **3.2** is used to convert a chiral amine into bidentate imine **3.3**. The imine is complexed to Fe(II) to form the octahedral complex **3.4**.

## 3.2 RESULTS AND DISCUSSION

### 3.2.1 Increasing the Rate of Imine Formation

In our previous assay pyridine carboxaldehyde was allowed to react with a chiral primary amine to form a bidentate imine (Scheme 3.1). The reaction was quantitative, but required molecular sieves and took 2 hours to go to completion.<sup>4</sup> In the interest of speeding up this reaction we switched to aldehyde **3.2** (Scheme 3.2). Based on the research of Chin and Wolf,<sup>2,3</sup>

we hypothesized that the presence of the hydroxyl group ortho to the aldehyde would increase the rate of imine formation *via* hydrogen bonding and/or general acid catalysis. Indeed, the addition of the hydroxyl group greatly enhanced the reactivity of the aldehyde towards amines, because the reaction of **3.2** is finished in less than 10 seconds to yield imines **3.3**. Further, no molecular sieves are required to drive the reaction with **3.2** to completion.

### 3.2.2 Choice of Analytes and Derivatization Method

The chiral amines **MBA**, **CEA**, and **HPA** (Figure 3.1) were chosen for study to span a range of chemical space representing aromatic, cyclic, and aliphatic moieties, respectively. The amines were converted to imines (Figure 3.2), and *in situ* were allowed to complex with Fe(II) as shown in scheme 3.2. The resulting inorganic coordination complexes **3.4** were colored with a corresponding broad MLCT charge-transfer band with a  $\lambda_{\text{max}}$  between 572nm and 577nm, depending on the imine (Figure 3.3). No UV-*vis* or CD bands were seen in this region for **3.3** or Fe(II) alone.

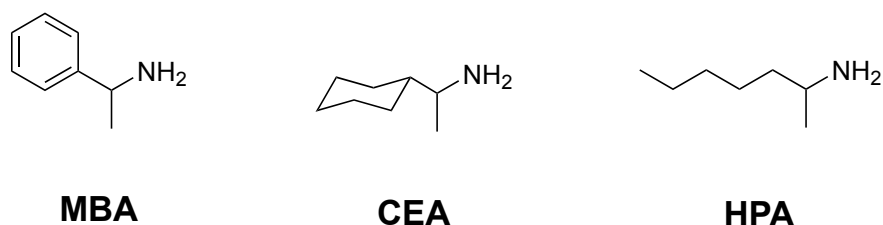


Figure 3.1. The three amines studied.

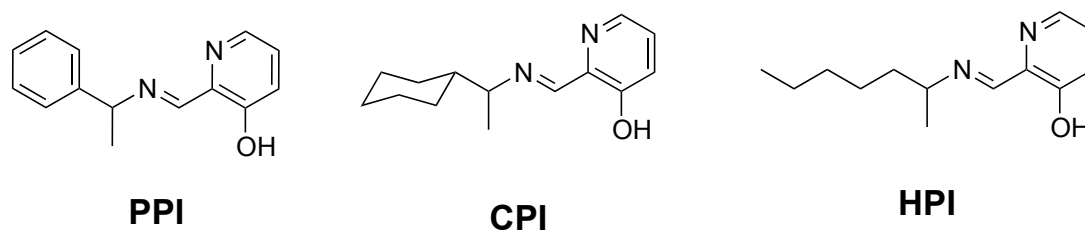


Figure 3.2. The imines formed after reaction of the amines with aldehyde **3.3**.

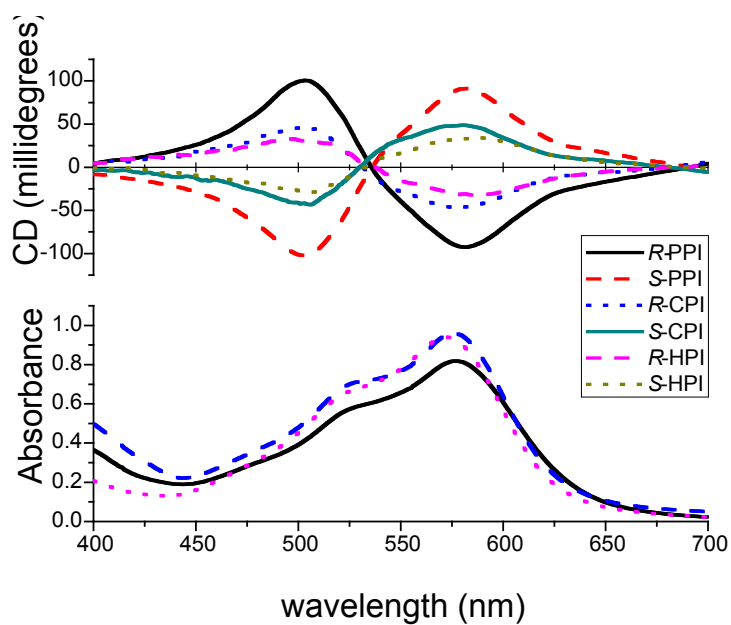


Figure 3.3. UV-*vis* and CD spectra of the MLCT bands of **3.4** for the three different imines studied, **PPI** (3mM), **CPI** (6mM), and **HPI** (7mM), at 100% *ee* in acetonitrile at 1mM Fe(II) in a 0.1cm quartz cell.



### 3.2.3 Determining Saturation *via* UV-vis Titrations

Titrations were performed to determine the proper ratios of **3.3** to Fe(II) required to reach signal saturation (Figure 3.4). Saturation is important because it allows for the development of concentration independent calibration curves. As long as the assay is performed above saturation, *ee* calibration curves developed at a single concentration can be used to analyze unknowns at any concentration. Saturation also yields the maximum signal-to-noise ratio and minimizes 2:1 and 1:1 imine to ligand species, which thereby simplifies the stereochemical analysis of the CD data. The titrations revealed saturation at three equivalents for **PPI** and **HPI**, but nearly five equivalents were required for **CPI** because it has a lower affinity for the metal. The sigmoidal shapes of the curves reflect the high order stoichiometry of the system (3:1). The imines, **PPI**, **HPI**, and **CPI**, show approximately the same overall change in absorption at 575nm, 577nm, and 570nm, respectively.

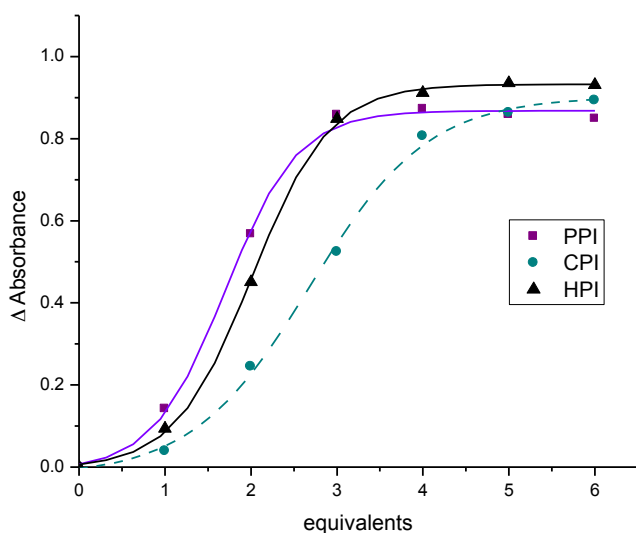


Figure 3.4. The change in absorbance as a function of equivalents of imine titrated into an acetonitrile solution of 1mM Fe(II) at 575nm, 577nm, and 570nm for **PPI**, **CPI**, and **HPI**, respectively. Equivalents of imine is defined as the concentration of imine divided by the concentration of Fe(II).

### 3.2.4 Stereoisomerism

As discussed, working above saturation minimizes 2:1 and 1:1 species. Thus, the dominant complex present is the 3:1 complex of imine **3.3** with Fe(II). There are two helical isomers ( $\Delta$  and  $\Lambda$ ), and two geometric isomers (*fac* and *mer*).<sup>5</sup> Thus, for an enantiomerically pure sample, there are four possible stereoisomers. For amines that are not enantiomerically pure, there are 8 possible stereoisomers for the *fac* isomer and 16 possible isomers for the *mer* isomer, giving a total of 24 possible stereoisomers. Figure 3.5 shows all stereoisomers broken up into sets based on the distribution of *R* and *S* stereogenic amines around Fe(II). The large number of stereoisomers present when mixtures of *R* and *S* amines are added to a solution of Fe(II) could result in a level of complexity that circumvents the ability to accurately determine the *ee* of the chiral amines. However, as long as all the complexes are in equilibria, and the same distribution of complexes can be reproducibly obtained, the CD spectra will be consistent and indicative of *ee* values.

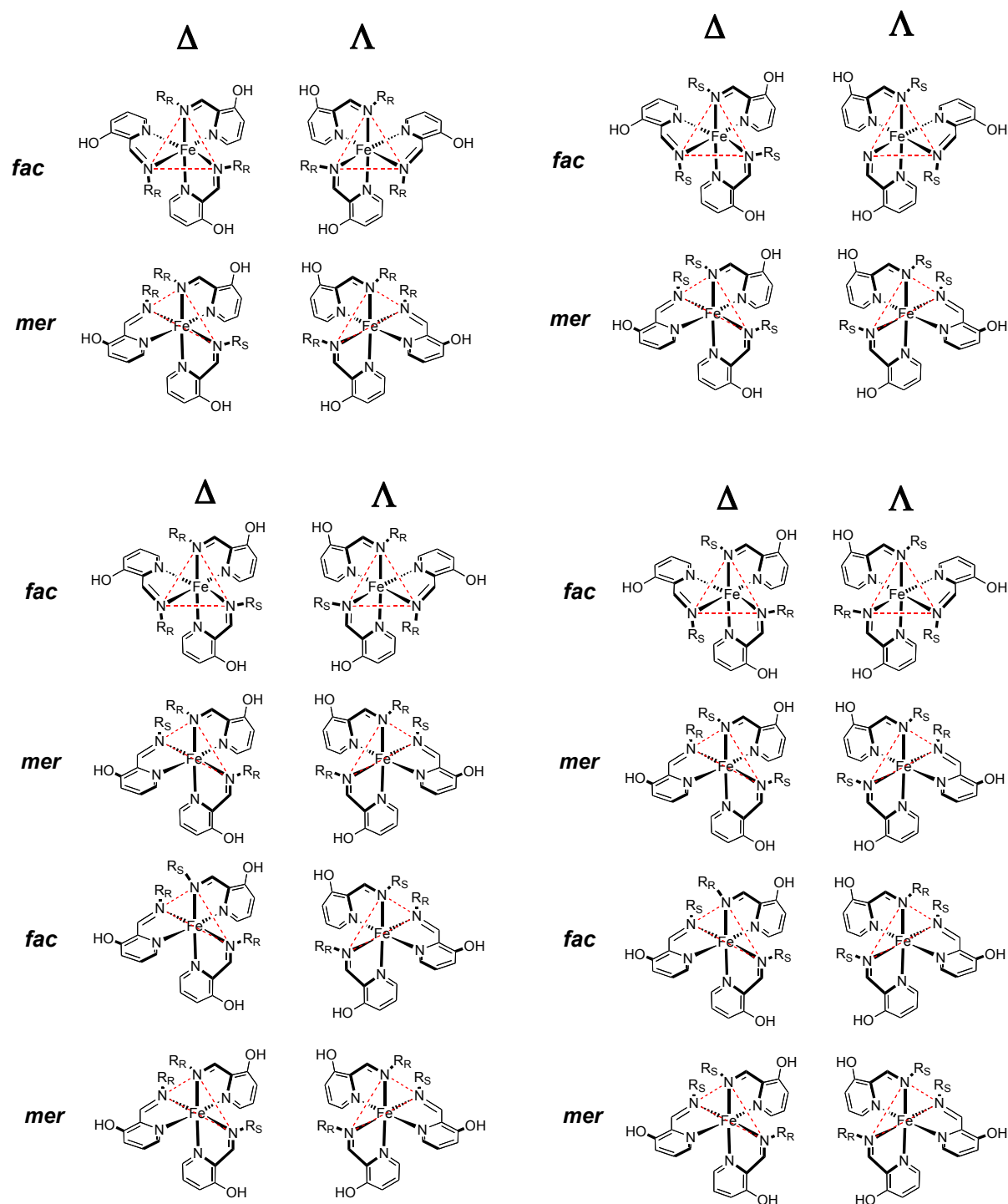


Figure 3.5. The 24 possible stereoisomers that can form upon mixing of enantiomers of **3.3** with Fe(II). In this figure, the isomers are organized by the mixture of stereogenic centers on each complex, the geometry isomerism (*fac* and *mer*), and the helical isomerism (D and L). The red dotted lines trace out the 'face' and 'meridian' defined by the three imine nitrogens for the *fac* and *mer* isomers, respectively.

### 3.2.5 Constructing Calibration Curves

Calibration curves were made by plotting the ellipticity at a single wavelength from 517-525nm, depending on the imine, as a function of *ee* at constant concentration of Fe(II) and **3.3**. To demonstrate that the calibration curves were independent of the concentration of **3.3** above saturation, curves were developed for **PPI** and **CPI** at multiple concentrations. As can be seen from Figures 3.6 and 3.7, there is little difference between ellipticities at different concentrations.

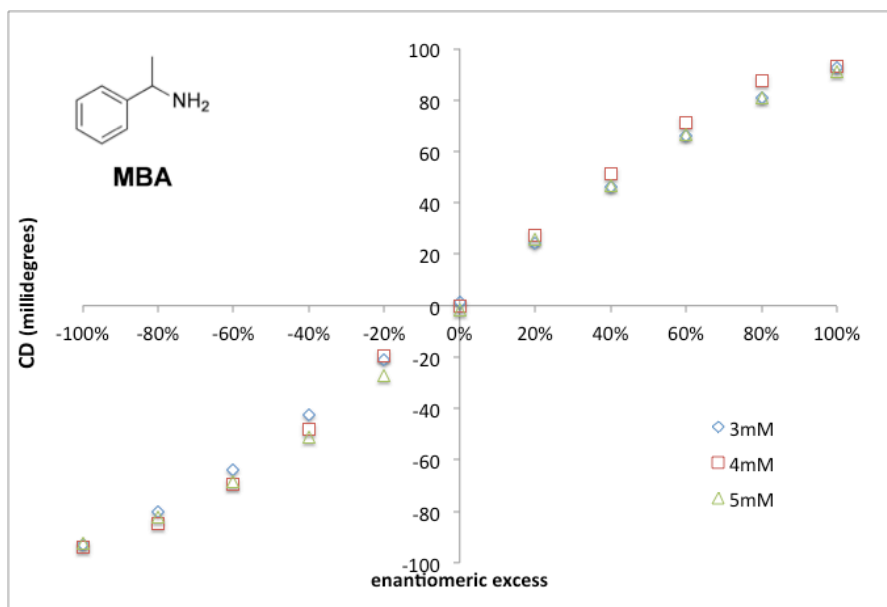


Figure 3.6. A plot of the ellipticity at 519nm as a function of *ee* with 1mM Fe(II), 2mM **3.3**, and 3mM, 4mM, and 5mM of **PPI** (derived from **MBA**) in acetonitrile in a 0.1cm cell.

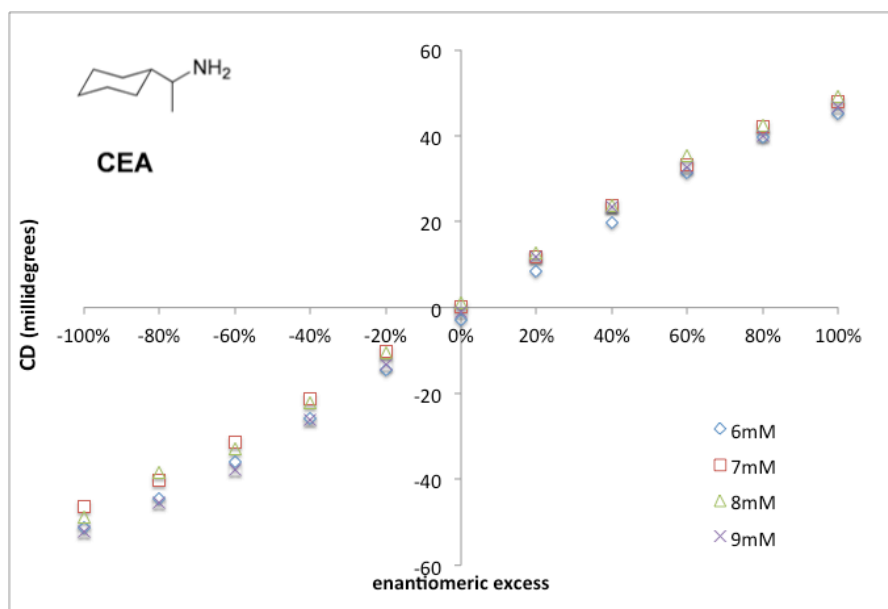


Figure 3.7. A plot of the ellipticity at 525nm as a function of *ee* with 1mM Fe(II), 2mM **3.3**, and 6mM, 7mM, 8mM, and 9mM of **CPI** (derived from **CEA**) in acetonitrile in a 0.1cm cell.

The shapes of the calibration curves are sigmoidal, which we postulated could arise from some form of cooperativity between chiral imines with the same stereogenic center for binding to Fe(II). However, this was ruled out. If there was such cooperativity, the shapes of the calibration curves above saturation would vary with concentration because there would be excess imines, which would thermodynamically sort to achieve the most stable isomers. As previously discussed, this is not observed. Thus, if there is no thermodynamic preference, the mixtures of chiral imines are most likely distributed statistically around Fe(II).

In order to test whether the imines were statistically distributed around Fe(II), theoretical calibration curves were developed using a probabilistic model. The first step in developing the model was to calculate the statistical distribution of isomer sets at a variety of *ee* values (Table 3.1). A 100% *ee* is defined as 1 and a -100% *ee* is defined as -1. Thus, for example, at 80% *ee* the distribution of complexes belonging to set (*R,R,R*) is 0.73, which means 73% of the total concentration of complex has the configuration (*R,R,R*); whereas the distribution of complexes belonging to (*S,S,S*) is only 0.00074. In order to account for the equal and opposite nature of CD

signals arising from enantiomeric pairs, a positive sign was assigned to isomers that are predominantly *R* and a negative sign was assigned to isomers that are predominantly *S*. Thus, at 80% *ee* the (*R,R,R*) set has a positive value of 0.73 and the (*S,S,S*) set has a negative value of -0.00074. The signs were assigned based on the signs of the CD spectra of enantiomerically pure solutions of the complexes. Negative and positive values were assigned to the probabilities with predominantly *S* and *R* stereogenic centers, respectively, as a means of predicting the shape of the *ee* calibration curves. Finally, because CD signals arising from enantiomeric pairs cancel, the assigned probabilities were summed to give the overall shape of the calibration curves.

% <i>ee</i>	( <i>R,R,R</i> )	( <i>R,R,S</i> )	( <i>S,S,R</i> )	( <i>S,S,S</i> )	sum
100	1	0	0	0	1
80	0.73	0.25	-0.025	-0.00074	0.95
60	0.51	0.39	-0.094	-0.0071	0.80
40	0.34	0.45	-0.19	-0.025	0.58
20	0.21	0.44	-0.29	-0.061	0.30
0	0.12	0.38	-0.38	-0.12	0
-20	0.061	0.29	-0.44	-0.21	-0.30
-40	0.025	0.19	-0.45	-0.34	-0.58
-60	0.0071	0.094	-0.39	-0.51	-0.80
-80	0.00074	0.025	-0.25	-0.73	-0.95
-100	0	0	0	-1	-1

Table 3.1. A table of the calculated probabilities spanning 100% *ee* to -100% *ee* for different mixtures of chiral imine stereogenic centers surrounding Fe(II).

A normalized plot of the experimental calibration curve with an overlay of the calculated calibration curve shows that the probabilistic model does predict the shape of the curve in each case (Figures 3.8, 3.9, 3.10). However, the sigmoidal shape of the calculated curve is more pronounced than that of the experimental curve. We postulated that the disagreement between the calculated and experimental curves arises from an assumption in the probabilistic model that the CD signal of isomers from sets (*R,R,R*) and (*S,S,S*) are equal in intensity to the signals of isomers from sets (*R,R,S*) and (*S,S,R*), respectively.

To correct for this assumption and refine the probabilistic model, the differences in the signal magnitudes were calculated from the experimental CD data. The signal magnitudes of the sets of Fe(II) complexes for the pure isomers (*R,R,R*) and (*S,S,S*) were measured directly *via* CD data by taking the spectra at 100% *ee* and -100% *ee*, respectively. Using the calculated probabilities, the signal magnitudes for sets (*R,R,S*) and (*S,S,R*) were calculated at each point on the calibration curve by subtracting the contributions from the pure (*R,R,R*) and (*S,S,S*) isomer sets using their distribution as given in Table 3.1. For instance, at 80% *ee*, the mean and standard deviation of the signals calculated for the isomer sets (*R,R,S*) or (*S,S,R*) at concentrations above saturation are  $66.9 \pm 6.6$  millideg,  $30.0 \pm 2.9$  millideg, and  $15.8 \pm 7.1$  millideg for **PPI**, **CPI**, and **HPI**, respectively. By dividing the pure isomer ellipticity by the mixed isomer ellipticities, the fractional decrease in signal in going from a pure isomer set to mixed isomer sets was found to be 0.75, 0.62, and 0.45 for **PPI**, **CPI**, and **HPI**, respectively. The values can be incorporated into the probabilistic calibration curve model by multiplying the probabilities for sets (*R,R,S*) and sets (*S,S,R*) by this fractional decrease. Plotting this calculated signal greatly improved the agreement with experimentally determined calibration curves, as can be seen in Figures 3.8, 3.9 and 3.10.

To summarize this section, it is unlikely that the sigmoidal shapes of the calibration curves arise from cooperativity since the curves are not concentration dependent. If cooperativity is not present, then the sigmoidal shapes of the curves most likely arise from a statistical distribution of the enantiomers around Fe(II). To test this hypothesis a model was developed in the following way. (1) the statistical distribution of isomer sets at various *ee* values were calculated and tabulated; (2) A positive and negative sign was assigned to the calculated *ee* values of sets that are predominantly R and S, respectively; (3) Because CD signals arising from enantiomeric pairs cancel, the signed calculated *ee* values were summed; (4) The signal magnitudes of isomer sets (*R,R,S*) and (*S,S,R*) were calculated using experimental and statistical data.; (5) The signal magnitudes of isomer sets (*R,R,S*) and (*S,S,R*) were incorporated into the model. The overlay of the experimental and calculated calibration curves (Figures 3.8, 3.9, 3.10)

demonstrate how well the model agrees with the experimental data. This provides good evidence that the sigmoidal shape of the calibration curves arise from a statistical distribution of enantiomers around Fe(II).

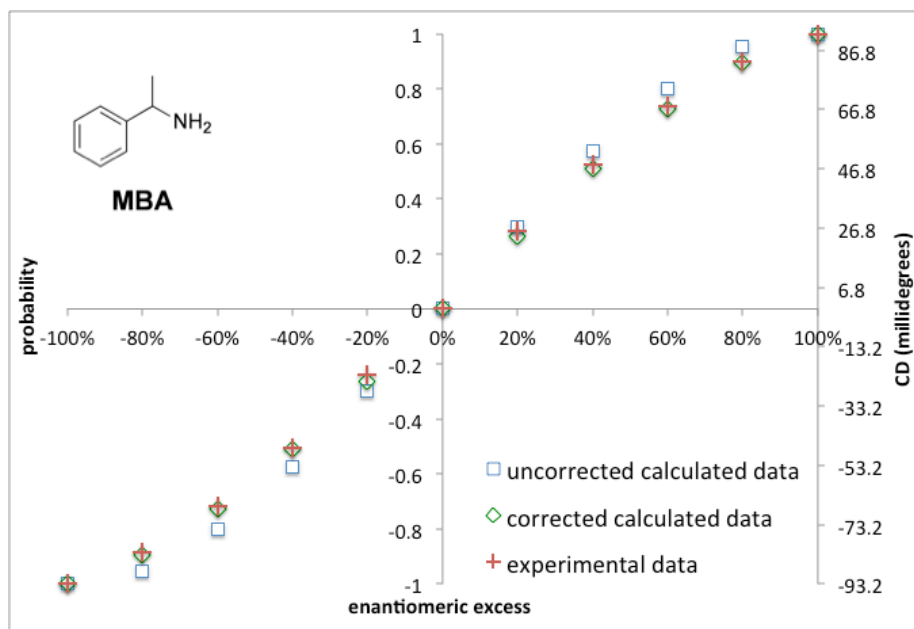


Figure 3.8. The overlay of the uncorrected calculated data, corrected calculated data, and experimental data for **MBA**.



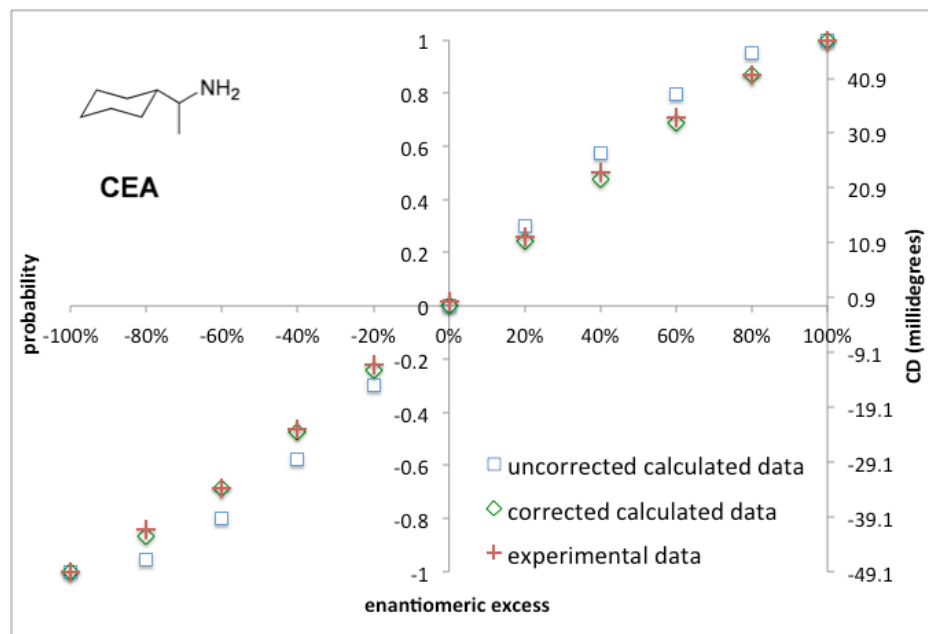


Figure 3.9. The overlay of the uncorrected calculated data, corrected calculated data, and experimental data for **CEA**.

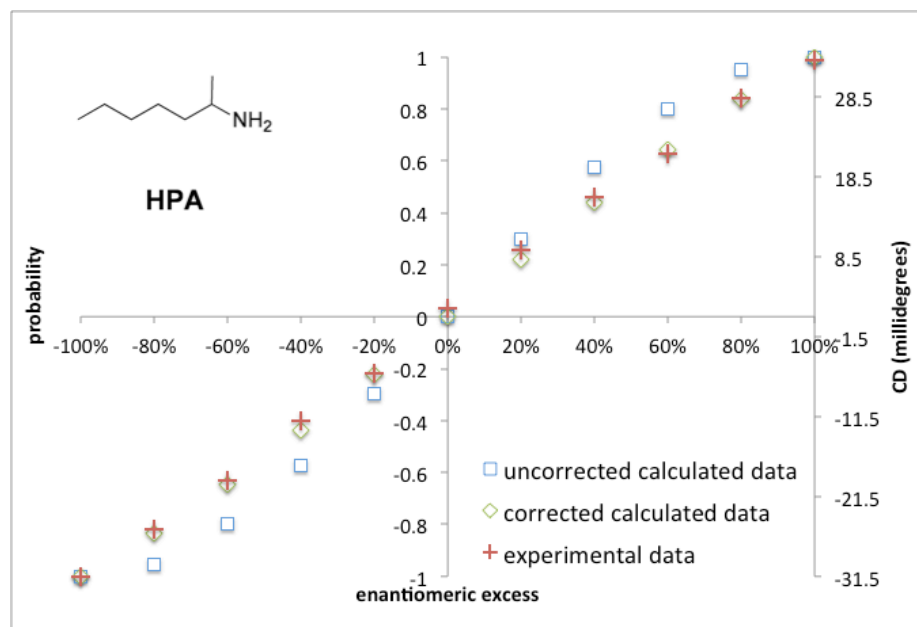


Figure 3.10. The overlay of the uncorrected calculated data, corrected calculated data, and experimental data for **HPA**.

### 3.2.6 Crystal Structure

A crystal structure of the *S*-**PPI**- $\Delta$ -*fac* Fe(II) complex was obtained by slow diffusion of diethyl ether into an acetonitrile solution of the complex. As can be seen in Figure 3.11, there is  $\pi$ - $\pi$  stacking between the benzyl group that is attached to the stereogenic center of the imine and the phenolic moiety of the parent aldehyde derivatizing agent. This crystal structure is in agreement with those obtained for a similar complex obtained by Howson *et al.*<sup>5</sup> The  $\pi$ - $\pi$  stacking in this complex would be absent in the **CPI**-Fe(II) complex, and explains the lower affinity of **CPI** for the metal in comparison to **PPI**.

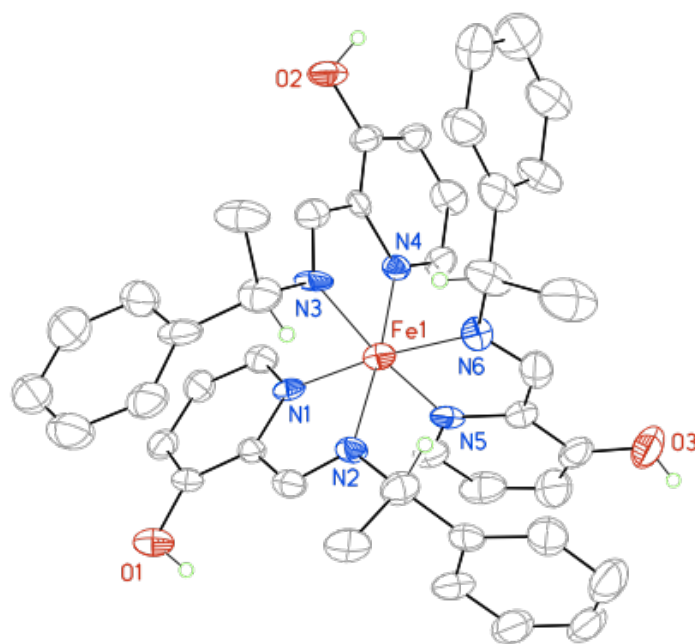


Figure 3.11. A crystal structure of the *S*-**PPI**- $\Delta$ -*fac* Fe(II) showing a partial atom labeling scheme. Displacement ellipsoids are scaled to the 50% probability level. Most hydrogen atoms were removed for clarity.

### 3.2.7 NMR Experiments to Determine the Diastereomeric Bias

In order to better understand the *fac/mer* diastereomeric bias of the Fe(II) complexes, <sup>1</sup>H NMR experiments were performed on the **PPI**-Fe(II) complex. Figure 3.12 shows the peaks corresponding to the benzylic proton of this complex at -100% *ee* (only the *S* isomer of **PPI**). Based on the <sup>1</sup>H NMR and crystallographic studies done by Howson *et al.*,<sup>5</sup> the largest peak in the spectrum can be assigned to the *S*-**PPI**- $\Delta$ -*fac* Fe(II) isomer.. Integration of the peaks allows for a calculation of 35% diastereomeric excess for the *S*-**PPI**- $\Delta$ -*fac* Fe(II). The two multiplets between 4.70 and 4.90 belong to the two inequivalent protons of the *mer* isomer. The 2:1 ratio and poor resolution of the two multiplets suggests that they arise from the two inequivalent protons of the *S*-**PPI**- $\Delta$ -*mer* Fe(II) and *S*-**PPI**- $\Lambda$ -*mer* Fe(II).

<sup>1</sup>H NMR experiments were also done on enantiomerically impure imine samples (see section 3.6.2). However, the complexity of the spectra made it difficult to extract any useful information about the diastereoselectivity. The fact that all four possible isomers involved when an enantiomerically pure amine is used ((*S,S,S*) set in Figure 3.5) lends credence to the notion that all 24 possible isomers of Figure 3.5 would be present with a mixture of enantiomeric imines.

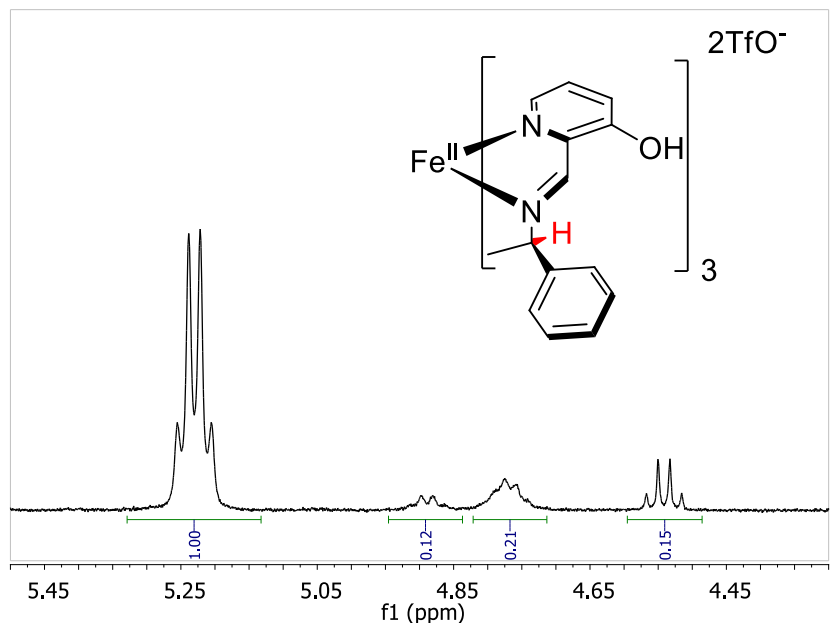


Figure 3.12.  $^1\text{H}$  NMR spectrum of the **PPI-Fe(II)** complex at -100% *ee*. The four quartets correspond to the benzylic proton (in red) for the four different diastereomers

### 3.2.8 Exciton Coupling.

The proximity and dissymmetric orientation of the three ligands surrounding Fe(II) allows for ECCD. In the UV region of the spectrum in Figure 3.14, the null values of the bisignate CD signals correspond to the  $\lambda_{\text{max}}$  of the UV-vis spectrum, which is typical of exciton coupling.

The sign of the Cotton effect allows us to conclude that imines with an *R* or *S* stereogenic center induce a  $\Lambda$  or  $\Delta$  helicity around Fe(II), respectively, which leads to a predictable ECCD couplet (Figure 3.13). It can be seen in Figure 3.14 that the signs of the ECCD in the UV region correlate with the identity of the stereogenic center of the imine. Complexes containing imines with the *R* stereogenic center have a negative ECCD couplet and those with *S* stereogenic center have a positive ECCD couplet.

Imines derived from amines with similar functionality should follow the same pattern and, as previously mentioned, the three amines span a range of chemical space representing aromatic, cyclic, and acyclic moieties. Thus, it is reasonable to assume the system will be applicable in the determination of the absolute configuration of most simple chiral amines.

The CD signals corresponding to charge transfer bands in the visible portion of the spectrum are also bisignate and possibly arise from ECCD. By analogy, if the  $\pi$ - $\pi^*$  transition in the UV is exciton coupled, the d- $\pi^*$  transition should also be coupled since the  $\pi^*$  molecular orbital of the exciton would be virtually the same.

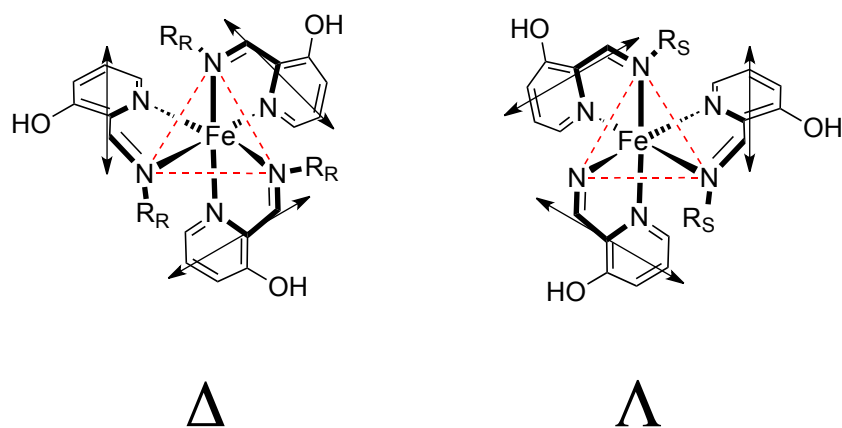


Figure 3.13. The helical arrangement of the transition dipoles that couple giving rise to the positive and negative ECCD couplets for the  $\Delta$ -*R* and  $\Lambda$ -*S* fac isomers, respectively.

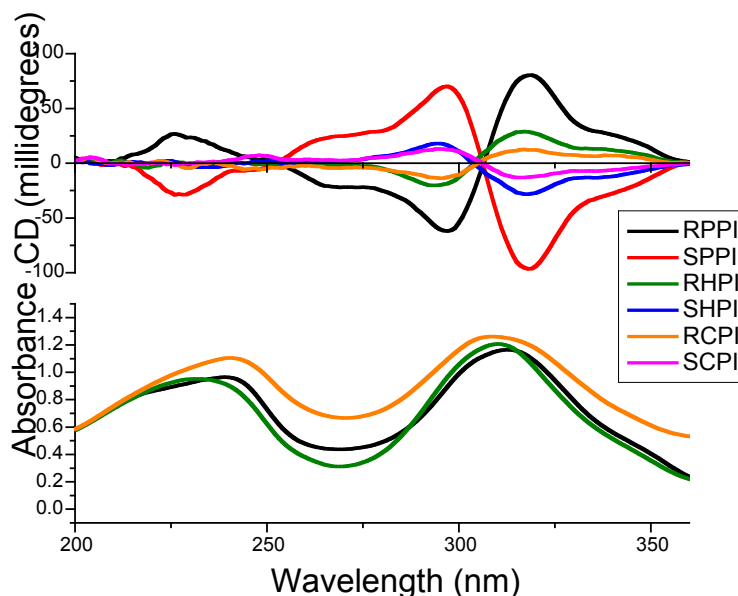


Figure 3.14. The ECCD spectra for the **PPI**, **CPI**, and **HPI** Fe(II) complexes at 0.3mM in a 0.1cm cuvette.

### 3.2.9 Enantiomeric Excess Determination

As discussed above, calibration curves were constructed by varying the *ee* at concentrations above saturation for all three imines. The curves were fit using the spreadsheet software Microsoft® Excel®. Because the shapes of the curves were sigmoidal, a third degree polynomial regression was used for fitting.

Unknowns for all three imines at a variety of *ee* values and concentrations were prepared. The primary optical data was input into the third degree polynomial and used to solve for *ee*. The results, summarized in Table 3.2, further demonstrate the concentration independence of the calibration curves. If the calibration curves were concentration dependent, it would be expected that the error would be lowest for the calculation of *ee* at or near the concentration the calibration curve was developed at. However, this is not observed. For example, the calibration curve for

**HPI** was developed at 6mM, and the absolute error is lower for test samples not done at 6mM (Table 3.2).

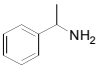
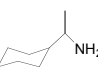
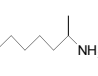
Analyte	Concentration (mM)	Actual <i>ee</i>	Experimental <i>ee</i>	Absolute error
 PPI	3.2	-51.0	-48.9	2.1
	3.2	32.0	30.3	1.7
	3.5	-58.0	-52.6	5.4
	3.5	38.0	35.0	3.0
	4.1	-56.0	-48.7	7.3
	4.1	75.6	68.7	6.9
	4.3	-51.0	-46.2	4.8
	4.3	22.0	20.2	1.8
	5	-30.0	-25.4	4.6
	5	52.0	47.3	4.7
Analyte	Concentration (mM)	Actual <i>ee</i>	Experimental <i>ee</i>	Absolute error
 CPI	7.2	-75.0	-62.0	13.0
	7.2	45.0	38.5	6.5
	7.5	-66.2	-58.7	7.5
	7.5	-68.6	-61.2	7.4
	8.3	-28.2	-28.5	0.3
	8.3	84.8	79.6	5.2
	8.6	10.4	9.0	1.4
	8.6	100	100.4	0.4
	9	30.0	30.4	0.4
	9	-52.0	-60.3	8.3
Analyte	Concentration (mM)	Actual <i>ee</i>	Experimental <i>ee</i>	Absolute error
 HPI	4.2	-57.2	-63.5	6.3
	4.2	71.4	60.9	10.5
	4.6	-11.6	-14.9	3.3
	4.6	35.0	28.8	6.2
	5.3	-77.2	-78.0	0.8
	5.3	47.8	42.3	5.5
	5.6	-57.0	-62.3	5.3
	5.6	29.0	21.8	7.2
	6.0	-10.0	-18.5	8.5
	6.0	-80.0	-85.6	5.6

Table 3.2. A list of the actual *ee* values as calculated from enantiomerically pure solutions and those determined using the assay (Experimental *ee*).



The average absolute error for the assay was calculated and determined to be  $\pm 5\%$ . As discussed in previously published work, we consider an absolute error even as large as  $\pm 15\%$  to be useful in a rapid screening protocol. The accuracy of this system is well within this limit.

### 3.3 CONCLUSIONS

There were several shortcomings with our previously reported assay.<sup>4</sup> Namely, the imine formation was slow, there was a need for host synthesis, the error was moderately high, and it required the use of an artificial neural network to calculate *ee* at different concentrations. In order to overcome the slow imine formation, aldehyde **3.2** was used instead of pyridine carboxaldehyde, which reduced the time for imine formation from several hours to 10 seconds. The need for host synthesis was replaced by using self-assembly to bring together several chromophores with Fe(II). The moderately high error associated with our previous system was overcome by increasing the signal-to-noise by using a strongly absorbing charge transfer band present in **3.4** to develop calibration curves and analyze unknowns. Lastly, an artificial neural network was not necessary because the assay is concentration independent above saturation, as determined by UV-*vis* titrations.

Calibration curves developed for the system had a sigmoidal shape, and it was shown that the shape most likely arises from a probabilistic distribution of stereogenic centers around Fe(II). A UV active band could be used to determine the absolute configuration of amines by correlating the sign of the ECCD with the identity of the stereogenic center. A charge transfer band in the visible region could be used to develop calibration curves for the determination of *ee* of unknown samples with an average accuracy of  $\pm 5\%$ .

Future studies will focus on the development of chromophoric aldehydes that absorb in the visible region, where interference from solvent and chromophores inherent to the analytes are unlikely, which would increase the utility of the system for absolute configuration determination.

Additionally, the use of other metals as scaffolds could decrease the amount of time needed for equilibration.

Currently, the protocol is being transitioned to aid in the discovery of asymmetric catalysts in collaboration with synthetic methodology chemists.

### **3.4 EXPERIMENTAL DETAILS**

#### **3.4.1 General**

All reagents were purchased from commercial sources and used as received with the exception of aldehyde **3.2**. Aldehyde **3.2** was purified by sublimation under high vacuum with mild heat (60-70oC) using a cold finger apparatus before use in the assay. HPLC grade acetonitrile purged for 2 hours with nitrogen was used throughout. An automated Varian Mercury 400MHz spectrometer was used to collect <sup>1</sup>H NMR spectra. Solutions were dispensed into Microamp<sup>®</sup> optical 96-well reaction plates purchased from applied biosystems using multichannel and single channel eppendorf research pipettes. CD spectra measurements were taken on a JASCO-815 CD spectrometer outfitted with an autosampler. 96-well reaction plates were sealed during equilibration periods using viewseal advanced sealing tapes purchased from E&K Scientific.

#### **3.4.2 UV-Visible Titrations**

#### **3.4.3 Calibration Curves and Test Sample Experimental for PPI**

A solution of aldehyde **3.2** at 18mM was transferred in 100 microL aliquots to a 96-well plate. To this was added 100 microL aliquots of a solution of 15mM **MBA** for the calibration curve developed at 5mM, 12mM **MBA** for calibration curve developed at 4mM, and 9mM for

the calibration curve developed at 3mM. 100microL of a 3mM Fe(TfO)<sub>2</sub> solution was then aliquoted into each well and the plate was sealed for 3 hours before being placed on the autosampler for spectral measurements. Test samples were prepared and run in an analogous manner from a 15mM stock solution of **MBA** and diluted accordingly.

#### **3.4.4 Calibration Curves and Test Sample Experimental for CPI**

A solution of aldehyde 3.2 at 36mM was transferred in 100 microL aliquots to a 96-well plate. To this was added 100 microL aliquots of a solution of 27mM **CEA** for the calibration curve developed at 9mM, 24mM **CEA** for the calibration curve developed at 8mM, 21mM for the calibration curve developed at 7mM and 18mM for the calibration curve developed at 6mM. 100microL of a 3mM Fe(TfO)<sub>2</sub> solution was then aliquoted into each well and the plate was sealed for 3 hours before being placed on the autosampler for spectral measurements. Test samples were prepared in an analogous manner from a 36mM stock solution of **CEA** and diluted accordingly.

#### **3.4.5 Calibration Curves and Test Sample Experimental for HPI**

A solution of aldehyde 3.2 at 18mM was transferred in 100 microL aliquots to a 96-well plate. To this was added 100 microL aliquots of a solution of 18mM **HPA** for the calibration curve developed at 6mM. 100microL of a 3mM Fe(TfO)<sub>2</sub> solution was then aliquoted into each well and the plate was sealed for 3 hours before being placed on the autosampler for spectral measurements. Test samples were prepared in an analogous manner from a 36mM stock solution of **HPA** and diluted accordingly.

## 3.5 PROBABILITY CALCULATIONS

### 3.5.1 General

The probability (P) was calculated for a pool of 100 molecules.

### 3.5.2 Probability Calculations at 100% *ee*

Isomer set (*R,R,R*) has a probability, P, where:

$$P = \left(\frac{100}{100}\right)\left(\frac{99}{99}\right)\left(\frac{98}{98}\right) = 1$$

Because the sum of the probabilities must equal 1, isomer sets (*R,R,S*), (*S,S,R*), and (*S,S,S*) must equal 0.

### 3.5.3 Probability Calculations at 80% *ee*

At 80% *ee* there are 90 imines with R stereogenic centers and 10 imines with S stereogenic centers.

Isomer set (*R,R,R*) has a probability, P, where

$$P = \left(\frac{90}{100}\right)\left(\frac{89}{99}\right)\left(\frac{88}{98}\right) = 0.73$$

Isomer set (*R,R,S*) has a probability, P, where

$$P = 3 \left(\frac{90}{100}\right)\left(\frac{89}{99}\right)\left(\frac{10}{98}\right) = 0.25$$

Isomer set (S,S,R) has a probability, P, where

$$P = 3 \left( \frac{10}{100} \right) \left( \frac{9}{99} \right) \left( \frac{90}{98} \right) = 0.0083$$

Isomer set (S,S,S) has a probability, P, where

$$P = \left( \frac{10}{100} \right) \left( \frac{9}{99} \right) \left( \frac{8}{98} \right) = 0.00074$$

The probabilities for the remaining *ee* values are calculated in an analogous manner, and are summarized in Table 3.2. A graph of the probabilities for the different isomer sets is shown in Figure 3.15.

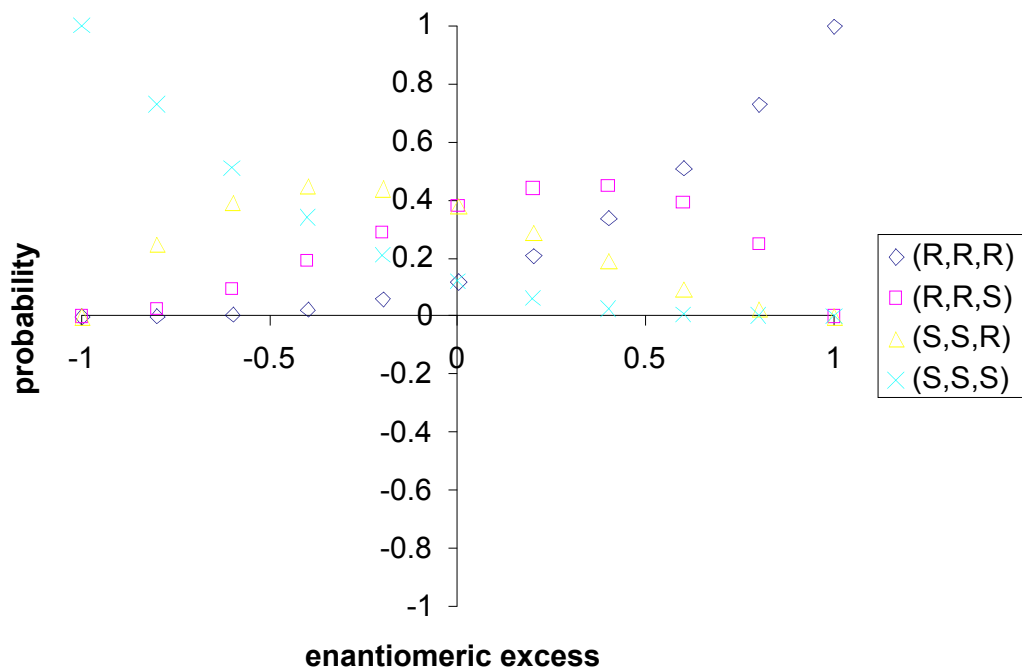


Figure 3.15. A graph of the probability of the four different isomer sets as functions of enantiomeric excess.

Enantiomers have equal and opposite CD signals. In order to reflect this in the probabilistic model, a negative sign is introduced for isomer sets that are predominantly *S* as seen in Table 3.3. This is based on the sign of CD signal observed for -100% *ee* (all *S* imines) at the wavelength the calibration curves were taken at. A graph of how the probabilities vary with *ee* for the various isomer sets is shown in Figure 3.16.

ee	(R,R,R)	(R,R,S)	(S,S,R)	(S,S,S)
1	1	0	0	0
0.8	0.73	0.25	-0.025	-0.0022
0.6	0.51	0.39	-0.094	-0.0071
0.4	0.34	0.45	-0.19	-0.025
0.2	0.21	0.44	-0.29	-0.061
0	0.12	0.38	-0.38	-0.12
-0.2	0.061	0.29	-0.44	-0.21
-0.4	0.025	0.19	-0.45	-0.34
-0.6	0.0071	0.094	-0.39	-0.51
-0.8	0.0022	0.025	-0.25	-0.73
-1	0	0	0	-1

Table 3.3. A summary of the calculated probabilities for populations of different isomer sets at different *ee* values. A negative sign is introduced for the probabilities for (S,S,R) and (S,S,S) to reflect the equal and opposite nature of CD signals for different enantiomers.

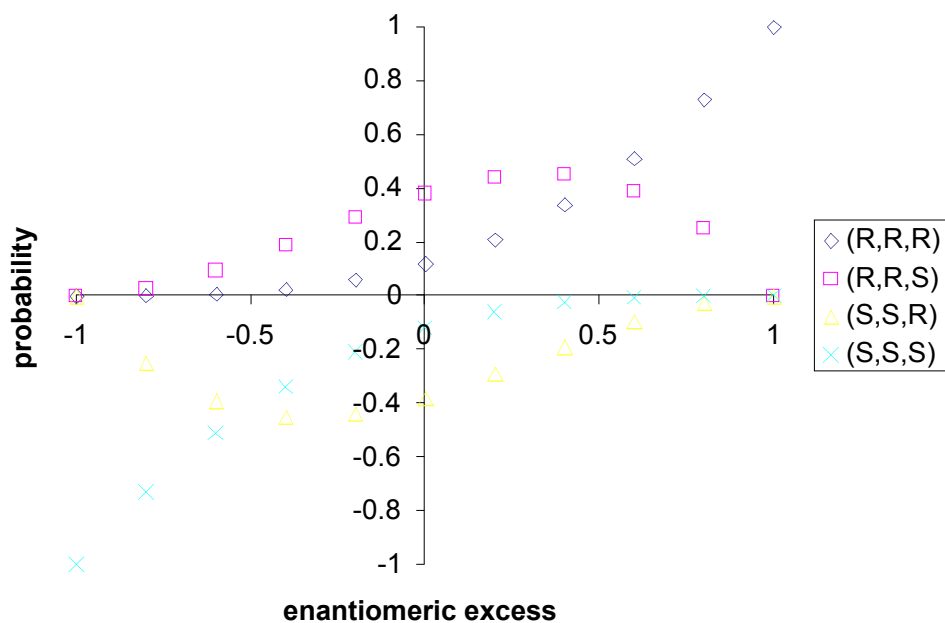


Figure 3.16. A graph of the four different isomer sets as a functions of *ee* with the introduction of a sign change for predominantly *S* isomer sets.

## 3.6 NMR SPECTRA

### 3.6.1 <sup>1</sup>H NMR Spectra for PPI, CPI, and HPI

The <sup>1</sup>H NMR for **PPI**, **CPI**, and **HPI** were done in CD<sub>3</sub>CN at the concentrations they would be used at in the assay (Figure 3.17, 3.18, 3.19). An excess of the amines was added to demonstrate that no side reactions take place when the ratio between **3.2** and the amines are not stoichiometric, to emulate the conditions in the assay.

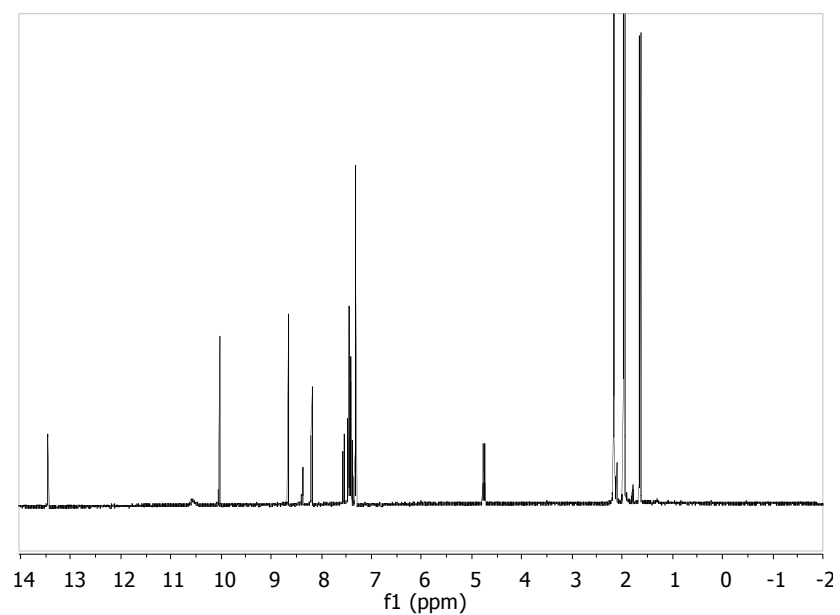


Figure 3.17. <sup>1</sup>H NMR of 10mM aldehyde **3.2** and 6mM **MBA**.



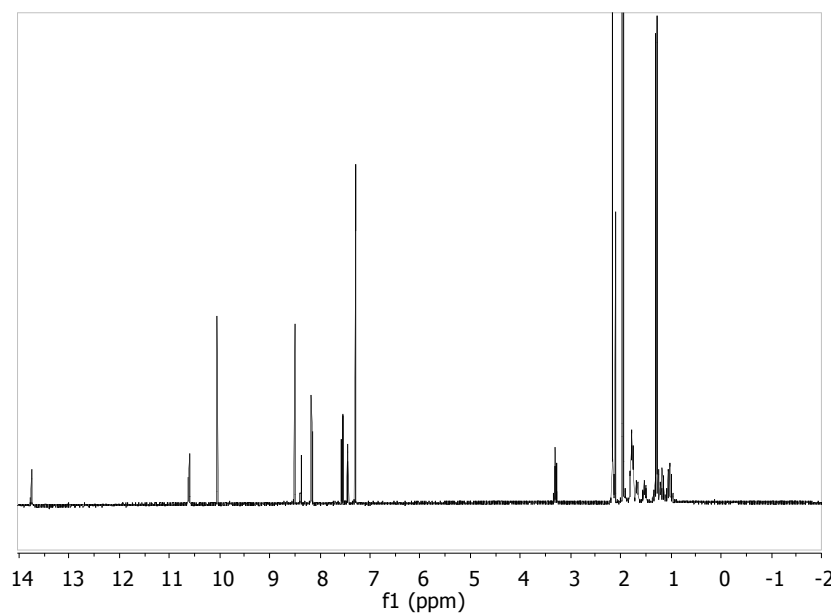


Figure 3.18.  $^1\text{H}$  NMR of 10mM aldehyde **3.2** and 6mM **CEA**.

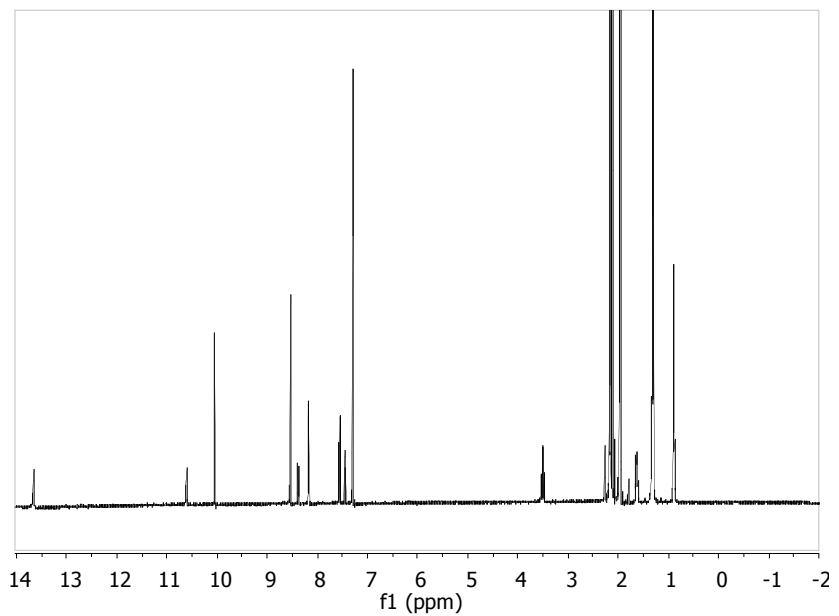


Figure 3.19.  $^1\text{H}$  NMR of 10mM aldehyde **3.2** and 6mM **HPA**.

### 3.6.2 $^1\text{H}$ NMR Spectra for Enantiomerically Impure Solutions of PPI-Fe(II)

$^1\text{H}$  NMR were taken for **PPI**-Fe(II) at 60%, 20%, 0%, -20%, and -60% *ee* in  $\text{CD}_3\text{CN}$  at 3mM using a 400Mhz Varian NMR fitted with a robotic autosampler (Figures 3.20, 3.21, 3.22, 3.23, 3.24).

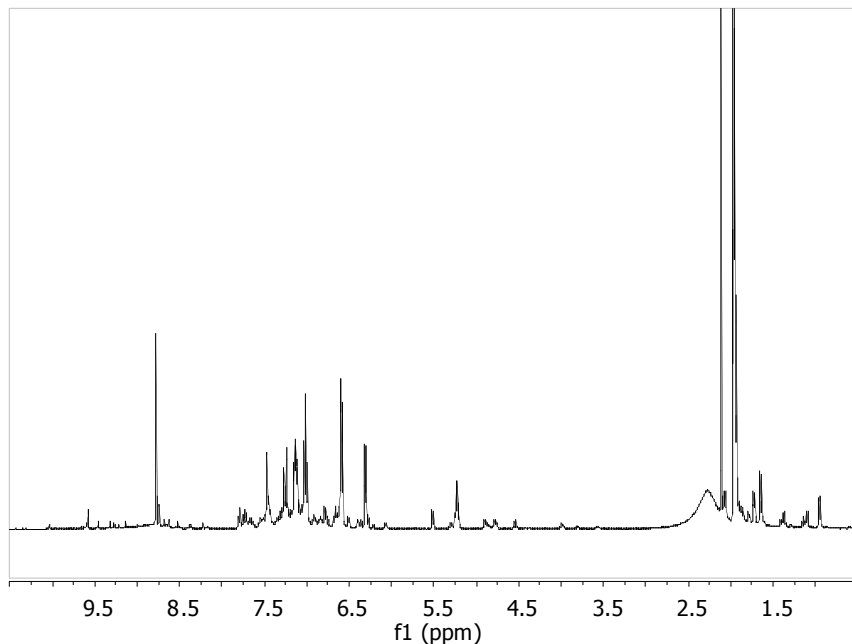


Figure 3.20. The  $^1\text{H}$  NMR of the **PPI**-iron(II) complex at -60% *ee*.

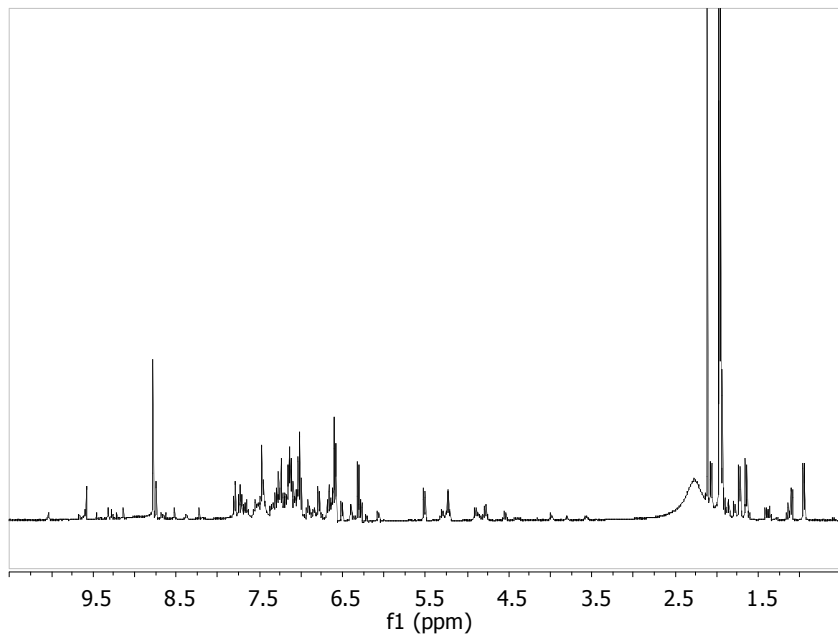


Figure 3.21. The <sup>1</sup>H NMR of the **PPI**-iron(II) complex at -20% *ee*.

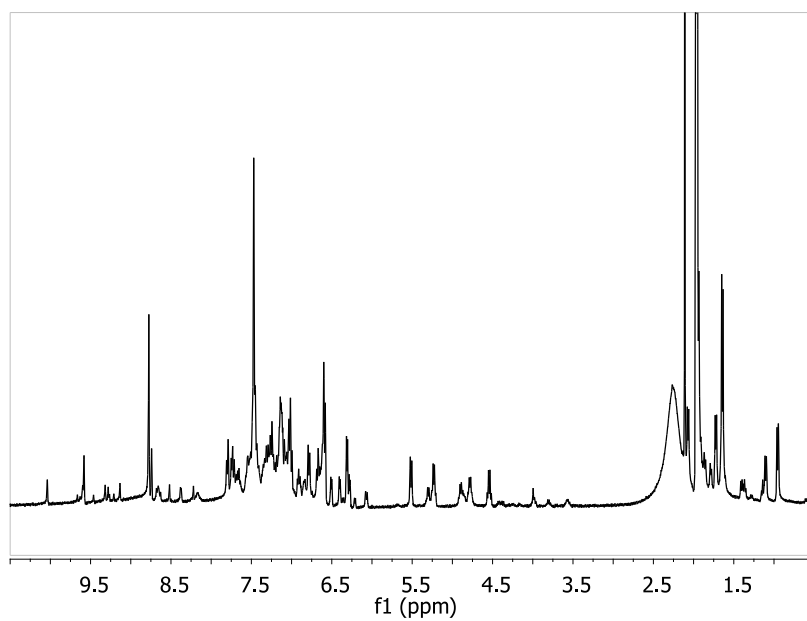


Figure 3.22. The <sup>1</sup>H NMR of the **PPI**-iron(II) complex at 0% *ee*.

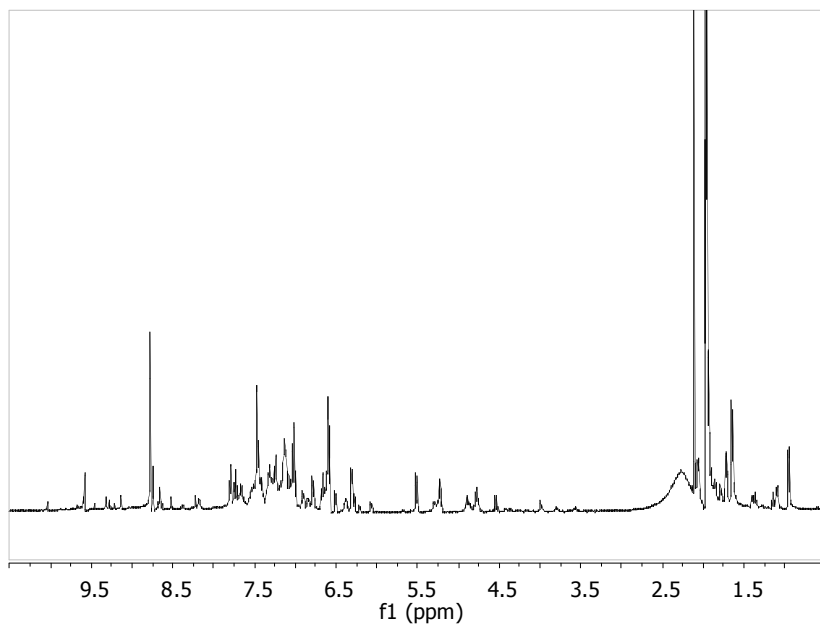


Figure 3.23. The <sup>1</sup>H NMR of the **PPI**-iron(II) complex at 20% *ee*.

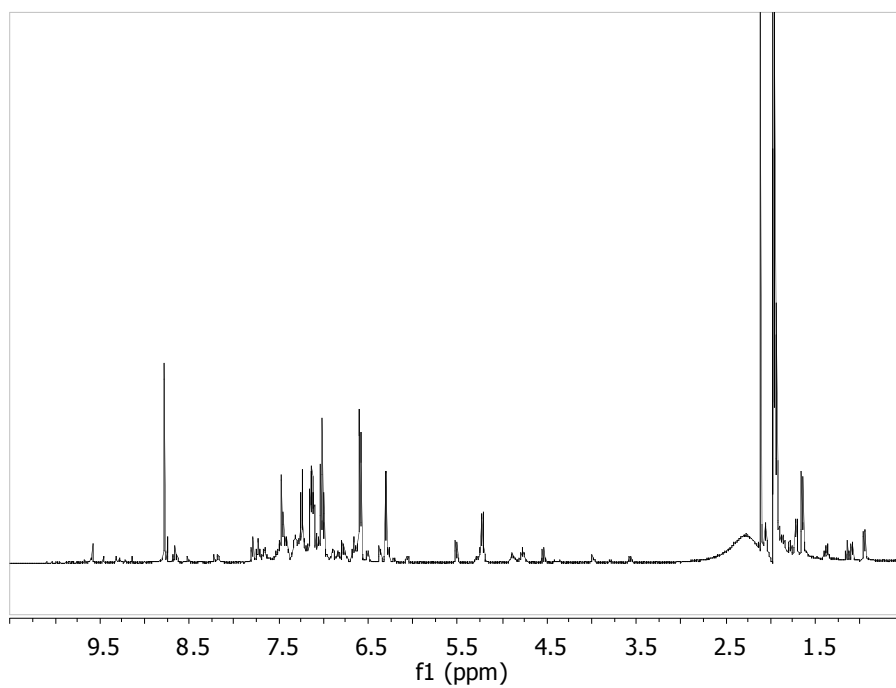


Figure 3.24. The <sup>1</sup>H NMR of the **PPI**-iron(II) complex at 60% *ee*.

Empirical formula	C47 H50 F6 Fe N6.50 O9.50 S2
Formula weight	1091.91
Temperature	153(2) K
Wavelength	0.71069 Å
Crystal system	Orthorhombic
Space group	P21212
Unit cell dimensions	a = 30.495(2) Å $\alpha = 90^\circ$ . b = 12.5164(9) Å $\beta = 90^\circ$ . c = 13.3325(12) Å $\gamma = 90^\circ$ .
Volume	5088.8(7) Å <sup>3</sup>
Z	4
Density (calculated)	1.425 Mg/m <sup>3</sup>
Absorption coefficient	0.461 mm <sup>-1</sup>
F(000)	2262
Crystal size	0.45 x 0.32 x 0.04 mm
Theta range for data collection	1.67 to 25.03°.
Index ranges	-36 ≤ h ≤ 36, 0 ≤ k ≤ 14, 0 ≤ l ≤ 15
Reflections collected	8743
Independent reflections	8743
Completeness to theta = 25.03°	98.8 %
Absorption correction	Semi-empirical from equivalents
Max. and min. transmission	1.12 and 0.929
Refinement method	Full-matrix least-squares on F <sup>2</sup>
Data / restraints / parameters	8743 / 1050 / 790
Goodness-of-fit on F <sup>2</sup>	1.373
Final R indices [I > 2σ(I)]	R1 = 0.0948, wR2 = 0.1570
R indices (all data)	R1 = 0.1689, wR2 = 0.1752
Absolute structure parameter	0.00(3)
Largest diff. peak and hole	0.703 and -0.395 e.Å <sup>-3</sup>

Table 3.4. Crystal data and structure refinement for *S-PPI-Δ-fac* Fe(II)

	x	y	z	U(eq)
Fe1	3142(1)	1649(1)	7490(1)	26(1)
O1	1628(2)	1159(4)	9089(3)	40(1)
O2	3281(2)	1136(4)	3626(3)	41(1)
O3	4534(2)	1068(5)	9532(4)	62(2)
N1	2600(2)	802(4)	7578(4)	21(1)
N2	2846(2)	2445(4)	8578(4)	24(1)
N3	2881(2)	2483(5)	6389(4)	29(2)
N4	3390(2)	835(4)	6352(4)	24(1)
N5	3458(2)	761(5)	8474(4)	28(2)
N6	3681(2)	2496(4)	7559(5)	29(1)
C1	2485(2)	-62(6)	7044(5)	30(2)
C2	2077(2)	-547(6)	7168(5)	35(2)
C3	1783(2)	-161(6)	7839(5)	33(2)
C4	1895(2)	720(6)	8406(5)	31(2)
C5	2303(2)	1172(5)	8247(5)	25(2)
C6	2469(2)	2095(5)	8791(5)	29(2)
C7	3036(2)	3366(6)	9183(5)	34(2)
C8	3327(2)	2899(6)	9986(5)	35(2)
C9	3210(3)	2039(6)	10577(5)	42(2)
C10	3484(3)	1663(7)	11309(6)	50(2)
C11	3875(3)	2084(7)	11482(6)	50(2)
C12	4007(3)	2943(8)	10945(7)	58(3)
C13	3732(3)	3340(7)	10201(6)	47(2)
C14	2686(2)	4086(6)	9660(5)	38(2)
C15	3681(2)	37(6)	6360(6)	34(2)
C16	3850(3)	-402(6)	5479(6)	40(2)
C17	3723(2)	-56(6)	4588(6)	35(2)
C18	3416(2)	763(6)	4549(5)	32(2)
C19	3264(2)	1215(5)	5437(5)	23(2)
C20	2972(2)	2120(6)	5517(6)	34(2)
C21	2573(2)	3382(6)	6469(5)	41(2)

C22	2107(3)	3007(6)	6641(5)	40(2)
C23	1923(3)	2242(6)	6036(6)	45(2)
C24	1491(3)	1940(8)	6160(7)	61(3)
C25	1226(3)	2422(7)	6882(7)	57(2)
C26	1414(3)	3201(7)	7493(7)	61(2)
C27	1857(3)	3502(6)	7377(6)	47(2)
C28	2587(3)	4128(6)	5572(5)	47(2)
C29	3333(3)	-150(6)	8893(5)	37(2)
C30	3607(3)	-735(7)	9551(6)	53(2)
C31	4007(3)	-332(8)	9793(6)	54(3)
C32	4144(3)	610(7)	9371(6)	41(2)
C33	3866(2)	1146(6)	8688(5)	32(2)
C34	3967(2)	2117(6)	8179(6)	38(2)
C35	3775(3)	3483(6)	6971(5)	40(2)
C36	3957(2)	3198(6)	5955(6)	39(2)
C37	4253(2)	2375(6)	5791(6)	44(2)
C38	4427(3)	2177(7)	4835(7)	57(3)
C39	4310(3)	2808(9)	4059(7)	68(3)
C40	4017(3)	3650(8)	4201(7)	63(3)
C41	3840(3)	3843(7)	5147(6)	47(2)
C42	4112(3)	4226(6)	7513(7)	66(3)
S1B	2731(1)	6800(2)	7553(3)	40(1)
F1B	3343(3)	6017(8)	6424(7)	60(4)
F2B	3560(3)	6484(10)	7890(7)	87(5)
F3B	3428(3)	7671(6)	6774(7)	80(3)
O1B	2497(4)	7074(11)	6645(8)	45(5)
O2B	2738(3)	7638(9)	8291(8)	41(4)
O3B	2645(4)	5749(6)	7934(9)	55(4)
C1B	3285(3)	6732(7)	7144(7)	68(4)
S1BA	2879(2)	6299(5)	6915(5)	45(2)
F1BA	3333(5)	8012(12)	7330(13)	68(5)
F2BA	3469(6)	6673(17)	8303(13)	63(6)
F3BA	2882(6)	7541(18)	8511(14)	50(6)
O1BA	2709(8)	5515(12)	7601(14)	44(6)
O2BA	3201(6)	5911(17)	6221(14)	59(8)
O3BA	2556(7)	7000(20)	6485(16)	44(9)

C1BA	3145(5)	7160(11)	7791(10)	58(6)
S1A	4521(1)	6549(3)	10892(3)	43(1)
F1A	4458(3)	6091(8)	8999(5)	88(3)
F2A	5071(3)	6762(8)	9409(6)	86(3)
F3A	4925(4)	5143(8)	9807(6)	104(4)
O1A	4192(4)	5741(10)	11083(10)	50(6)
O2A	4883(3)	6536(7)	11576(6)	53(3)
O3A	4346(3)	7585(6)	10669(7)	61(3)
C1A	4753(3)	6127(8)	9738(7)	83(5)
S1C	5130(1)	641(3)	11949(3)	40(1)
F1C	4861(2)	-69(8)	13680(4)	57(3)
F2C	4891(3)	-1257(5)	12535(7)	70(3)
F3C	4377(2)	-94(8)	12522(8)	69(3)
O1C	4958(3)	1676(5)	12228(7)	57(3)
O2C	5570(2)	440(9)	12255(8)	50(3)
O3C	5026(4)	318(6)	10940(4)	39(3)
C1C	4807(3)	-238(7)	12695(6)	61(3)
N1E	4240(7)	5677(16)	11419(19)	47(6)
C2E	4538(7)	5666(15)	11891(15)	57(5)
C3E	4897(5)	5725(13)	12516(15)	57(4)

---

Table 3.5. Bond lengths [ $\text{\AA}$ ] and angles [ $^\circ$ ] for *S-PPI- $\Delta$ -fac* Fe(II).



Fe1-N6	1.958(5)	C16-C17	1.323(9)
Fe1-N1	1.968(5)	C17-C18	1.388(10)
Fe1-N3	1.970(6)	C18-C19	1.392(9)
Fe1-N5	1.971(6)	C19-C20	1.443(9)
Fe1-N2	1.978(5)	C21-C28	1.517(9)
Fe1-N4	1.978(6)	C21-C22	1.515(10)
O1-C4	1.339(8)	C22-C23	1.372(10)
O2-C18	1.380(8)	C22-C27	1.388(10)
O3-C32	1.336(9)	C23-C24	1.379(11)
N1-C1	1.341(8)	C24-C25	1.394(11)
N1-C5	1.352(8)	C25-C26	1.394(12)
N2-C6	1.264(8)	C26-C27	1.413(11)
N2-C7	1.522(9)	C29-C30	1.416(10)
N3-C20	1.279(8)	C30-C31	1.359(11)
N3-C21	1.469(9)	C31-C32	1.372(12)
N4-C15	1.336(8)	C32-C33	1.415(10)
N4-C19	1.365(8)	C33-C34	1.426(10)
N5-C29	1.326(9)	C35-C36	1.507(10)
N5-C33	1.365(9)	C35-C42	1.562(10)
N6-C34	1.292(9)	C36-C37	1.387(10)
N6-C35	1.490(9)	C36-C41	1.394(11)
C1-C2	1.394(9)	C37-C38	1.402(10)
C2-C3	1.355(9)	C38-C39	1.350(12)
C3-C4	1.380(9)	C39-C40	1.394(12)
C4-C5	1.385(9)	C40-C41	1.393(11)
C5-C6	1.455(9)	S1B-O3B	1.434(6)
C7-C8	1.509(10)	S1B-O2B	1.438(6)
C7-C14	1.534(9)	S1B-O1B	1.446(6)
C8-C13	1.382(10)	S1B-C1B	1.778(9)
C8-C9	1.381(10)	F1B-C1B	1.325(8)
C9-C10	1.369(10)	F2B-C1B	1.338(8)
C10-C11	1.322(10)	F3B-C1B	1.347(8)
C11-C12	1.353(11)	S1BA-O2BA	1.433(7)
C12-C13	1.391(11)	S1BA-O1BA	1.439(7)
C15-C16	1.395(10)	S1BA-O3BA	1.441(7)

S1BA-C1BA	1.783(10)	F3A-C1A	1.343(8)
F1BA-C1BA	1.358(9)	S1C-O2C	1.424(6)
F2BA-C1BA	1.347(10)	S1C-O3C	1.440(6)
F3BA-C1BA	1.338(10)	S1C-O1C	1.446(6)
S1A-O2A	1.432(6)	S1C-C1C	1.779(9)
S1A-O3A	1.434(6)	F1C-C1C	1.340(8)
S1A-O1A	1.447(7)	F2C-C1C	1.318(8)
S1A-C1A	1.775(9)	F3C-C1C	1.344(8)
F1A-C1A	1.335(8)	N1E-C2E	1.11(3)
F2A-C1A	1.328(8)	C2E-C3E	1.38(2)
N6-Fe1-N1	173.9(3)	C15-N4-Fe1	129.3(5)
N6-Fe1-N3	95.1(2)	C19-N4-Fe1	113.5(4)
N1-Fe1-N3	89.4(2)	C29-N5-C33	118.6(6)
N6-Fe1-N5	82.2(2)	C29-N5-Fe1	128.7(5)
N1-Fe1-N5	93.8(2)	C33-N5-Fe1	112.7(5)
N3-Fe1-N5	173.1(2)	C34-N6-C35	120.7(6)
N6-Fe1-N2	94.4(2)	C34-N6-Fe1	113.4(5)
N1-Fe1-N2	81.0(2)	C35-N6-Fe1	125.9(5)
N3-Fe1-N2	95.5(2)	N1-C1-C2	121.4(6)
N5-Fe1-N2	91.1(2)	C3-C2-C1	120.9(7)
N6-Fe1-N4	89.6(2)	C2-C3-C4	118.9(7)
N1-Fe1-N4	95.1(2)	O1-C4-C3	123.4(6)
N3-Fe1-N4	81.7(2)	O1-C4-C5	118.9(6)
N5-Fe1-N4	91.9(2)	C3-C4-C5	117.6(6)
N2-Fe1-N4	175.3(2)	N1-C5-C4	124.3(6)
C1-N1-C5	116.9(6)	N1-C5-C6	111.7(6)
C1-N1-Fe1	128.5(5)	C4-C5-C6	124.0(6)
C5-N1-Fe1	114.6(4)	N2-C6-C5	118.6(6)
C6-N2-C7	119.3(6)	C8-C7-N2	107.8(6)
C6-N2-Fe1	114.0(5)	C8-C7-C14	110.0(6)
C7-N2-Fe1	126.7(4)	N2-C7-C14	113.6(5)
C20-N3-C21	118.5(6)	C13-C8-C9	115.1(8)
C20-N3-Fe1	113.6(5)	C13-C8-C7	121.2(7)
C21-N3-Fe1	127.6(4)	C9-C8-C7	123.7(7)
C15-N4-C19	117.1(6)	C10-C9-C8	121.1(8)

C11-C10-C9	122.6(9)	N6-C35-C42	112.2(6)
C10-C11-C12	119.5(8)	C36-C35-C42	108.3(6)
C11-C12-C13	118.8(8)	C37-C36-C41	118.4(7)
C8-C13-C12	123.0(9)	C37-C36-C35	123.9(7)
N4-C15-C16	122.3(7)	C41-C36-C35	117.6(7)
C17-C16-C15	121.2(7)	C36-C37-C38	121.4(8)
C16-C17-C18	118.3(7)	C39-C38-C37	119.6(9)
O2-C18-C17	119.0(6)	C38-C39-C40	120.4(9)
O2-C18-C19	121.4(6)	C41-C40-C39	120.3(9)
C17-C18-C19	119.6(6)	C40-C41-C36	120.0(8)
N4-C19-C18	121.6(6)	O3B-S1B-O2B	115.5(5)
N4-C19-C20	112.4(6)	O3B-S1B-O1B	115.1(5)
C18-C19-C20	126.0(6)	O2B-S1B-O1B	114.0(5)
N3-C20-C19	118.7(7)	O3B-S1B-C1B	103.8(5)
N3-C21-C28	113.4(6)	O2B-S1B-C1B	103.2(4)
N3-C21-C22	111.9(6)	O1B-S1B-C1B	102.9(5)
C28-C21-C22	109.7(6)	F1B-C1B-F2B	107.3(7)
C23-C22-C27	120.2(8)	F1B-C1B-F3B	106.3(7)
C23-C22-C21	120.8(7)	F2B-C1B-F3B	105.8(7)
C27-C22-C21	118.9(8)	F1B-C1B-S1B	112.5(6)
C22-C23-C24	120.7(8)	F2B-C1B-S1B	112.3(6)
C23-C24-C25	121.2(9)	F3B-C1B-S1B	112.2(6)
C24-C25-C26	117.9(9)	O2BA-S1BA-O1BA	115.2(7)
C25-C26-C27	121.0(8)	O2BA-S1BA-O3BA	114.7(7)
C22-C27-C26	119.0(8)	O1BA-S1BA-O3BA	115.0(7)
N5-C29-C30	122.4(7)	O2BA-S1BA-C1BA	108.5(12)
C31-C30-C29	119.0(8)	O1BA-S1BA-C1BA	99.2(10)
C30-C31-C32	119.8(8)	O3BA-S1BA-C1BA	101.7(13)
O3-C32-C31	125.1(8)	F3BA-C1BA-F2BA	103.7(15)
O3-C32-C33	115.7(8)	F3BA-C1BA-F1BA	107.4(17)
C31-C32-C33	119.2(8)	F2BA-C1BA-F1BA	106.0(16)
N5-C33-C32	121.0(7)	F3BA-C1BA-S1BA	114.4(12)
N5-C33-C34	113.5(7)	F2BA-C1BA-S1BA	113.0(11)
C32-C33-C34	125.5(7)	F1BA-C1BA-S1BA	111.7(11)
N6-C34-C33	118.2(7)	O2A-S1A-O3A	115.5(5)
N6-C35-C36	110.3(6)	O2A-S1A-O1A	114.5(5)

O3A-S1A-O1A	114.2(5)	O3C-S1C-O1C	114.3(5)
O2A-S1A-C1A	104.0(4)	O2C-S1C-C1C	104.5(4)
O3A-S1A-C1A	103.7(4)	O3C-S1C-C1C	103.1(4)
O1A-S1A-C1A	102.8(5)	O1C-S1C-C1C	102.1(4)
F2A-C1A-F1A	105.7(7)	F2C-C1C-F1C	106.7(7)
F2A-C1A-F3A	106.7(7)	F2C-C1C-F3C	106.9(7)
F1A-C1A-F3A	106.5(7)	F1C-C1C-F3C	105.5(7)
F2A-C1A-S1A	113.6(6)	F2C-C1C-S1C	113.6(6)
F1A-C1A-S1A	112.3(6)	F1C-C1C-S1C	112.5(6)
F3A-C1A-S1A	111.7(6)	F3C-C1C-S1C	111.1(6)
O2C-S1C-O3C	115.1(5)	N1E-C2E-C3E	175(2)
O2C-S1C-O1C	115.3(5)		

Table 3.6. Atomic coordinates ( $\times 10^4$ ) and equivalent isotropic displacement parameters ( $\text{\AA}^2 \times 10^3$ ) for *S-PPI- $\Delta$ -fac* Fe(II).  $U(\text{eq})$  is defined as one third of the trace of the orthogonalized  $U^{\text{ij}}$  tensor.

	U <sup>11</sup>	U <sup>22</sup>	U <sup>33</sup>	U <sup>23</sup>	U <sup>13</sup>	U <sup>12</sup>
Fe1	33(1)	24(1)	21(1)	0(1)	1(1)	2(1)
O1	50(3)	44(3)	26(3)	-6(3)	7(3)	2(3)
O2	51(3)	50(3)	21(3)	1(3)	7(3)	-3(3)
O3	41(4)	98(5)	48(4)	-16(3)	-18(3)	4(3)
N1	33(3)	16(3)	15(3)	1(3)	1(3)	4(2)
N2	28(3)	25(3)	20(3)	-5(3)	5(3)	4(3)
N3	41(4)	32(4)	14(3)	-4(3)	11(3)	6(3)
N4	24(3)	26(4)	22(3)	5(3)	3(3)	4(3)
N5	38(4)	28(4)	18(3)	-2(3)	8(3)	-6(3)
N6	28(3)	24(3)	33(3)	-1(3)	0(3)	0(2)
C1	37(4)	25(4)	28(4)	11(3)	4(3)	9(3)
C2	35(4)	37(4)	34(5)	-8(3)	-4(4)	-6(4)
C3	34(4)	38(4)	28(4)	4(3)	-5(3)	-9(3)
C4	31(4)	42(4)	18(4)	5(3)	5(3)	-2(4)
C5	24(4)	31(4)	20(4)	3(3)	2(3)	6(3)
C6	33(4)	31(4)	24(4)	2(3)	6(3)	5(3)
C7	42(4)	30(4)	29(4)	-4(4)	-1(3)	-3(4)
C8	34(4)	47(5)	24(4)	-13(4)	8(3)	1(4)
C9	56(5)	50(5)	22(4)	-4(4)	4(4)	-1(4)
C10	56(5)	64(5)	31(4)	-5(4)	-4(4)	10(5)
C11	51(5)	68(6)	30(4)	-13(4)	-13(4)	10(4)
C12	51(5)	72(6)	50(5)	-26(5)	-15(5)	3(5)
C13	41(4)	56(5)	44(5)	-22(4)	5(4)	7(4)
C14	54(5)	29(5)	30(4)	-23(4)	6(4)	5(4)
C15	37(4)	36(4)	28(4)	-2(4)	-3(4)	0(4)
C16	43(5)	33(5)	44(5)	-13(4)	9(4)	9(4)
C17	40(4)	40(4)	24(4)	-5(4)	0(4)	6(4)
C18	38(4)	35(4)	22(4)	4(4)	-2(4)	-7(4)
C19	16(4)	27(4)	25(4)	-2(3)	4(3)	-2(3)
C20	38(4)	37(4)	27(4)	6(4)	1(3)	1(4)
C21	52(5)	35(4)	35(4)	11(4)	4(4)	15(4)

C22	57(5)	43(5)	19(4)	10(4)	7(4)	19(4)
C23	45(5)	50(5)	41(5)	9(4)	8(4)	18(4)
C24	60(5)	66(6)	58(5)	13(5)	-2(5)	8(5)
C25	51(5)	74(6)	48(5)	27(5)	4(4)	14(5)
C26	65(5)	79(5)	39(4)	9(5)	14(5)	34(4)
C27	53(4)	56(5)	32(4)	10(4)	-2(4)	23(4)
C28	75(6)	32(5)	34(5)	11(4)	18(4)	20(4)
C29	47(4)	38(5)	26(4)	4(4)	-1(4)	6(4)
C30	78(6)	46(5)	35(5)	12(4)	4(5)	10(5)
C31	44(5)	69(6)	49(5)	2(5)	-5(4)	25(5)
C32	39(5)	56(5)	27(4)	-14(4)	-6(4)	17(4)
C33	35(4)	39(4)	22(4)	-4(4)	0(3)	0(4)
C34	29(4)	43(5)	40(4)	-20(4)	1(4)	5(4)
C35	53(5)	25(4)	42(4)	-5(4)	18(4)	-8(4)
C36	44(4)	30(4)	44(5)	-11(4)	8(4)	-21(4)
C37	50(5)	34(5)	49(5)	3(4)	23(4)	-8(4)
C38	56(5)	56(5)	58(5)	-10(5)	20(5)	-10(4)
C39	67(6)	85(6)	51(5)	-32(5)	4(5)	-14(5)
C40	45(5)	86(6)	56(6)	6(5)	-11(4)	-14(5)
C41	45(5)	55(5)	42(5)	-3(4)	9(4)	-1(4)
C42	93(6)	50(5)	54(5)	-10(6)	18(6)	-41(5)
S1B	42(2)	38(2)	39(2)	5(2)	-2(2)	-7(1)
F1B	66(6)	57(6)	57(6)	-42(5)	13(6)	-3(5)
F2B	73(7)	110(9)	78(9)	-26(7)	-14(6)	29(6)
F3B	93(7)	57(6)	91(8)	-6(6)	30(6)	-33(5)
O1B	51(8)	42(8)	43(8)	6(6)	-12(7)	-11(6)
O2B	49(8)	39(6)	35(7)	-17(5)	-8(6)	6(6)
O3B	79(8)	41(7)	45(8)	9(6)	11(6)	-17(6)
C1B	73(8)	64(7)	67(8)	-15(7)	-1(7)	-4(7)
S1BA	51(4)	42(4)	40(3)	-6(3)	3(3)	7(3)
F1BA	76(9)	59(9)	70(10)	7(9)	-6(9)	-27(7)
F2BA	54(9)	80(11)	55(10)	-27(9)	-32(8)	20(8)
F3BA	48(10)	57(10)	45(10)	-21(8)	-15(9)	7(8)
O1BA	69(11)	29(9)	33(11)	-6(9)	3(10)	-11(8)
O2BA	76(14)	47(12)	54(12)	-17(9)	-14(11)	10(10)
O3BA	47(13)	51(15)	35(12)	3(10)	-4(10)	17(11)

C1BA	53(9)	58(9)	63(10)	4(8)	-3(8)	-5(8)
S1A	42(2)	43(3)	44(2)	6(2)	8(2)	-1(2)
F1A	81(7)	130(8)	52(6)	-29(6)	-17(6)	4(6)
F2A	84(7)	95(7)	80(7)	-13(6)	38(6)	-27(6)
F3A	114(10)	105(8)	93(6)	-22(9)	39(8)	25(7)
O1A	45(9)	55(9)	50(10)	5(7)	0(7)	1(7)
O2A	42(6)	58(7)	58(7)	2(6)	-14(5)	-14(6)
O3A	60(7)	41(7)	84(8)	21(6)	4(6)	15(6)
C1A	84(8)	90(8)	75(8)	-11(7)	13(7)	0(7)
S1C	35(2)	48(3)	36(2)	-10(2)	2(2)	0(2)
F1C	66(7)	64(5)	40(4)	-5(5)	16(4)	5(6)
F2C	85(6)	60(5)	64(5)	-7(5)	18(5)	3(5)
F3C	67(5)	65(6)	74(6)	-1(6)	7(5)	-10(5)
O1C	59(6)	55(6)	56(6)	-15(5)	1(5)	4(5)
O2C	38(5)	64(6)	49(6)	5(5)	-3(5)	-2(5)
O3C	40(5)	48(7)	30(4)	1(4)	-4(5)	7(6)
C1C	66(6)	57(5)	58(5)	-7(5)	6(5)	0(5)
N1E	44(11)	40(10)	57(12)	-13(8)	7(9)	1(9)
C2E	56(8)	55(8)	59(9)	-3(7)	-5(8)	1(7)
C3E	52(7)	66(8)	54(8)	-6(8)	-2(8)	3(7)

---

Table 3.7. Hydrogen coordinates ( x 10<sup>4</sup>) and isotropic displacement parameters (Å<sup>2</sup>x 10<sup>3</sup>)for *S-PPI-Δ-fac* Fe(II)

	x	y	z	U(eq)
H1O	1778	1455	9538	60
H2O	3500	1333	3293	61
H3O	4646	813	10055	94
H1	2686	-350	6571	36
H2	2004	-1155	6776	42
H3	1505	-492	7917	40
H6	2297	2428	9296	35
H7	3221	3813	8728	40
H9	2934	1703	10474	51
H10	3390	1077	11708	60
H11	4061	1785	11980	59
H12	4282	3269	11075	69
H13	3827	3940	9824	56
H14A	2469	4286	9152	56
H14B	2825	4732	9927	56
H14C	2541	3700	10206	56
H15	3776	-241	6986	41
H16	4061	-959	5520	48
H17	3838	-360	3990	42
H20	2851	2440	4933	41
H21	2661	3808	7070	49
H23	2094	1918	5525	54
H24	1373	1394	5747	73
H25	927	2226	6954	69
H26	1241	3535	7997	74
H27	1982	4036	7795	56
H28A	2893	4290	5405	70
H28B	2432	4792	5735	70
H28C	2445	3784	4997	70
H29	3049	-419	8747	44
H30	3512	-1400	9819	63
H31	4190	-701	10252	65



H34	4237	2476	8293	45
H35	3495	3886	6876	48
H37	4340	1937	6338	53
H38	4625	1602	4734	68
H39	4429	2679	3411	81
H40	3938	4093	3652	75
H41	3639	4414	5240	57
H42A	4019	4339	8208	98
H42B	4126	4915	7165	98
H42C	4402	3890	7505	98

---

Table 3.8. Anisotropic displacement parameters ( $\text{\AA}^2 \times 10^3$ ) for *S-PPI- $\Delta$ -fac* Fe(II). The anisotropic displacement factor exponent takes the form:  $-2\pi^2 [h^2 a^{*2} U_{11} + \dots + 2 h k a^* b^* U_{12}]$

### 3.7 REFERENCES:

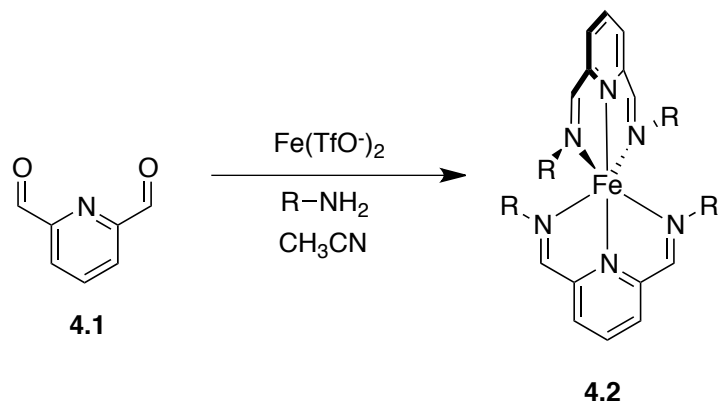
- (1) Iwaniuk, D. P.; Wolf, C. *Journal of the American Chemical Society* 2011, 133, 2414.
- (2) Kim, H.; So, S. M.; Yen, C. P.-H.; Vinhato, E.; Lough, A. J.; Hong, J.-I.; Kim, H.-J.; Chin, J. *Angewandte Chemie International Edition* 2008, 47, 8657.
- (3) Ghosn, M. W.; Wolf, C. *Journal of the American Chemical Society* 2009, 131, 16360.
- (4) Nieto, S.; Dragna, J. M.; Anslyn, E. V. *Chemistry – A European Journal* 2010, 16, 227.
- (5) Howson, S. E.; Allan, L. E. N.; Chmel, N. P.; Clarkson, G. J.; van Gorkum, R.; Scott, P. *Chemical Communications* 2009, 1727.

## Chapter 4: Chiral Amine Sensing via Iron(II) Templated Imine Formation

### 4.1 INTRODUCTION:

#### 4.1.1 Design Criteria:

As in our previous assay (see chapter 3), we employ Fe(II) as a scaffold and colorimetric indicator. Aldehyde **4.1** is used as a chromophoric derivatizing agent that converts the primary amine into a tridentate imine. Fe(II) can then be used to bring the two equivalents of tridentate imine into proximity (Scheme 4.1). We predicted that this would result in coupling of the  $\pi$ - $\pi^*$  transitions giving an ECCD couplet in the UV, which would be useful in the determination of absolute configuration. Additionally, it was expected that Fe(II) would form a CD active metal-to-ligand charge transfer band in the visible spectrum, which could be useful in the determination of *ee*.

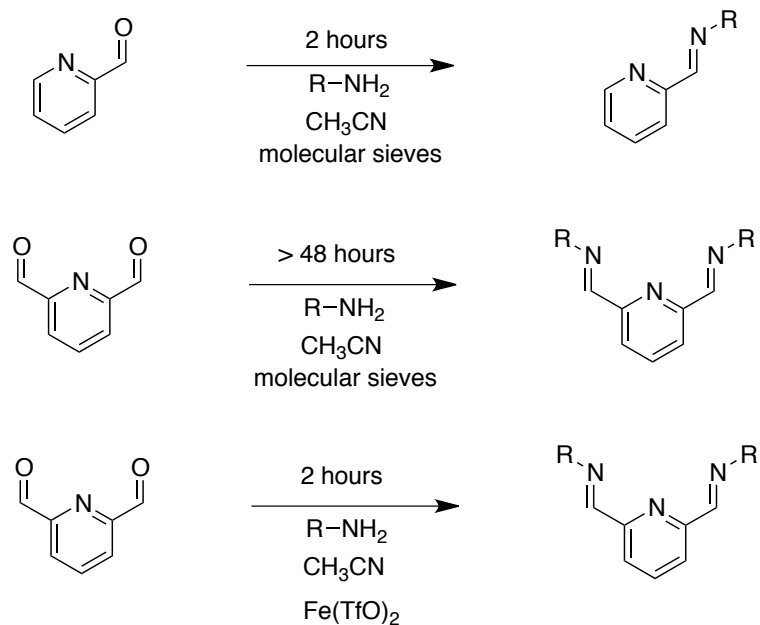


Scheme 4.1. Aldehyde **4.1** reacts with primary amines in the presence of Fe(II) to form complex **4.2**.

## 4.2 RESULTS AND DISCUSSION

### 4.2.1 Imine Formation

We attempted to preform the imine by mixing aldehyde **4.1** with amines in acetonitrile. Based on the similarities between the aldehyde **4.1** and pyridine carboxaldehyde, which was used in our previous assay,<sup>1</sup> it was expected that they would have similar reactivity. However, whereas amines mixed with pyridine carboxaldehyde over 4Å molecular sieves form imines quantitatively in 2 hours, the reaction of amines with aldehyde **4.1** over 4Å molecular sieves takes greater than 48 hours to go to completion. In order to speed up the reaction, 0.5 equivalents of Fe(II) were added to a solution of the aldehyde and amine, which decreased the reaction time to approximately 2 hours (see supporting information Figures 4.34-4.38 for NMR spectra). The increased reactivity of aldehyde **4.1** towards amines in the presence of Fe(II) likely results from an increase in the electrophilicity of the aldehyde moiety upon binding to Fe(II).



Scheme 4.2. A comparison of the reactivity of aldehyde **4.1** with amines in the absence and presence of Fe(II) and with the reactivity of pyridine carboxaldehyde in the presence of amines.

#### 4.2.2 Choice of Analytes

Chiral amines **MBA**, **CEA**, **HPA**, **dMBA**, **AMB**, and **SBA** were chosen to span the aliphatic, aromatic, and cyclic aliphatic range of chemical space (Figure 4.1).

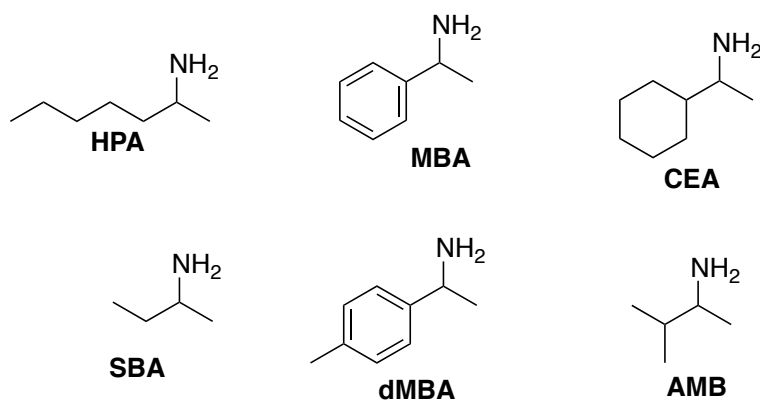


Figure 4.1. The different chiral amines chosen for study.

### 4.2.3 Titrations

In order to assess the concentration dependence of the reaction, titrations were performed (Figure 4.2). A 2:1 ratio of aldehyde **4.1** to amine was increased in concentration, while Fe(II) was held at a constant concentration of 2mM. Measurements were taken in the visible region (600nm) where imine complex **4.2** absorbs, but not Fe(II), dialdehyde **4.1**, the amine analytes, or the imine. The reactions were allowed to run overnight, and UV measurements showed that after 24 hours the signals remained stable over several hours suggesting that all of the reactions had reached equilibrium. The maximum signal occurs between 2 and 3 equivalents (equivalents is defined as the ratio of aldehyde **4.1** to Fe(II)) for all of the analytes). Before 2-3 equivalents, there is still Fe(II) left in solution, and as the aldehyde-amine concentration increases more of complex **4.2** forms and thus the signal continues to increase. However, after 2-3 equivalents the signal decreases. This may result from the presence of an excess of imine. Fe(II) forms a 1:3 complex with the imine as opposed to the 1:2 complex shown in Scheme 4.1. The 1:2 complex would be expected to have a different absorption than the 1:3 complex, which would explain why the signal decreases after 2-3 equivalents.

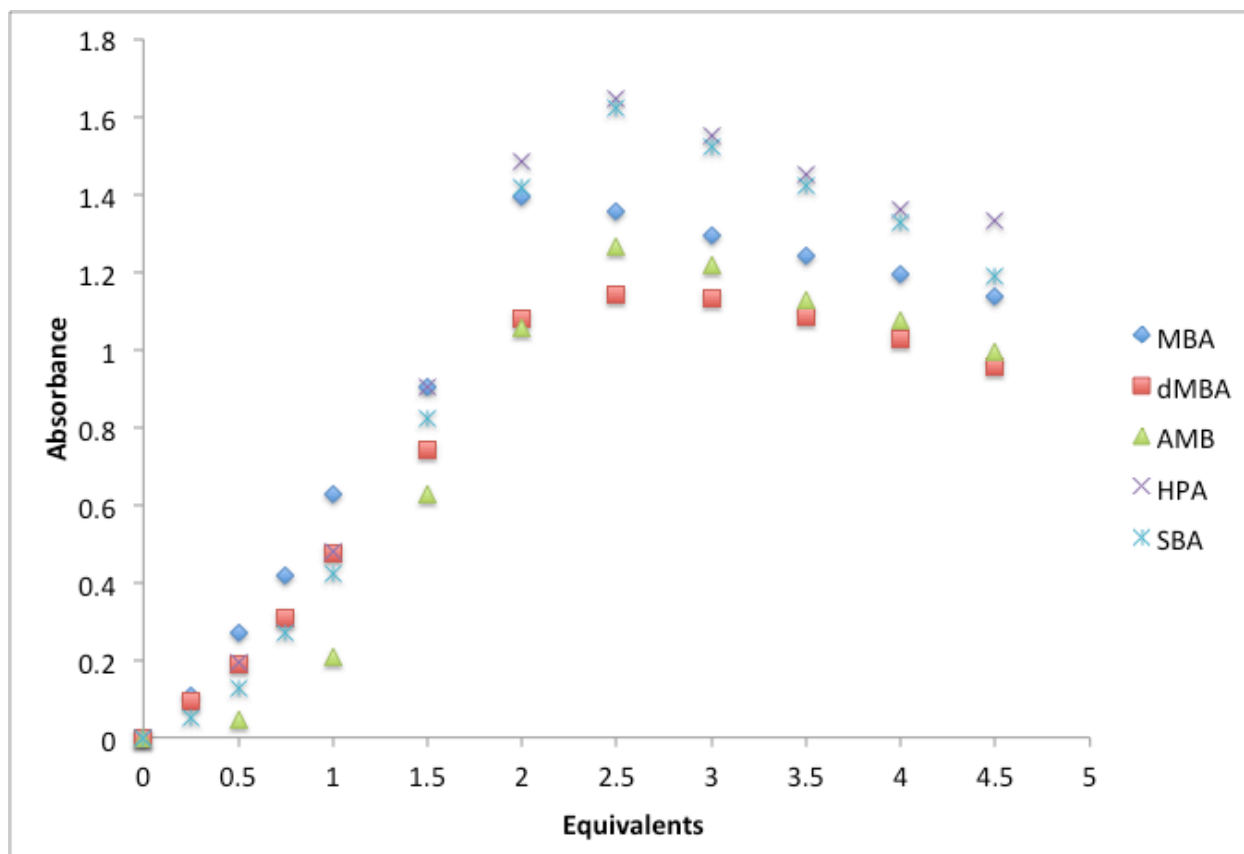


Figure 4.2. The change in absorbance at 600nm as a function of equivalents of aldehyde for the different amine analytes.

#### 4.2.4 Stereoisomerism

Because we were interested in using this system for enantiomeric excess determination, we considered all the possible imine complex stereoisomers that could form from an enantiomerically impure mixture of amines. For a complex of **4.2**, an enantiomerically pure sample can only exist as a single stereoisomer. However, if the sample contains a mixture of enantiomeric amines there are seven potential stereoisomers - three sets of enantiomers and one meso compound. Although there are seven potential stereoisomers, as long as the signal from the system is reproducible it should be useful in the determination of *ee*.

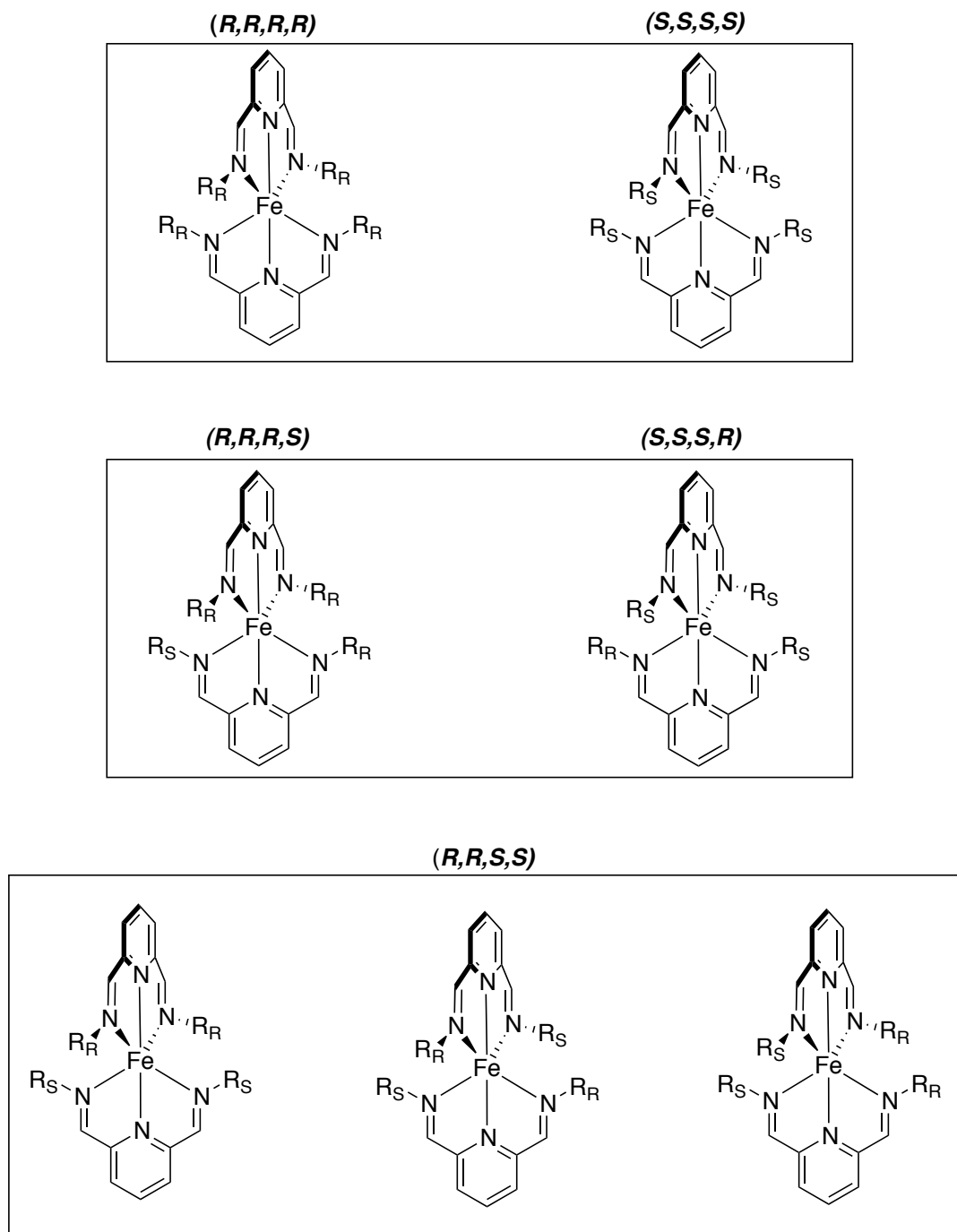


Figure 4.3. The possible stereoisomers that can exist for enantiomerically impure solutions of complex **4.2**.



#### 4.2.5 Absolute Configuration and Exciton Coupling

A bisignate CD curve in the ultraviolet region, that most likely results from the  $\pi\text{-}\pi^*$  transitions of the diimines, varies predictably with the identity of the stereogenic center of the amine. Amines with an *R* stereogenic center or an *S* stereogenic center always have a positive or negative first Cotton effect, respectively (Table 4.1).

Analyte	1st Cotton Effect: wavelength , CD	2nd Cotton Effect: wavelength , CD
R-MBA	335nm, 113 millidegrees	310nm, -50 millidegrees
S-MBA	335nm, -116 millidegrees	310nm, 52 millidegrees
R-CEA	334nm, 172 millidegrees	307nm, -170 millidegrees
S-CEA	334 nm, -157 millidegrees	307nm, 157 millidegrees
R-HPA	331nm, 103 millidegrees	300nm, -59 millidegrees
S-HPA	331nm, -96 millidegrees	300nm, 56 millidegrees
R-dMBA	336nm, 64 millidegrees	302nm, -20 millidegrees
S-dMBA	336nm, -70 millidegrees	302nm, 24 millidegrees
R-AMB	329nm, 196 millidegrees	299nm, -196 millidegrees
S-AMB	329nm, -186 millidegrees	299nm, 183 millidegrees
R-SBA	328nm, 75 millidegrees	305nm, -64 millidegrees
S-SBA	328nm, -57 millidegrees	305nm, 49 millidegrees

Table 4.1. A summary of how the sign of the CD signals vary predictably with the handedness of the amines.

The proximity of the diimines and the bisignate shape of the CD spectra suggests that the signal may result from ECCD. Coincidence of the null of the bisignate CD curve and the absorption maxima of the UV absorption is diagnostic of ECCD. However, the UV spectrum shows no absorption maxima within the wavelength range of the null for the CD curve (Figures 4.4-4.7). The lack of absorption maxima at the wavelength of the null of the CD curve does not provide evidence for the hypothesis that the CD signals arise from ECCD, but it does not completely rule out the possibility of ECCD. It is still possible that the CD signal arises from exciton coupling, but it may be from coupling of weaker transitions that are not observable in the UV spectrum because they are hidden underneath the signals from the stronger transitions.

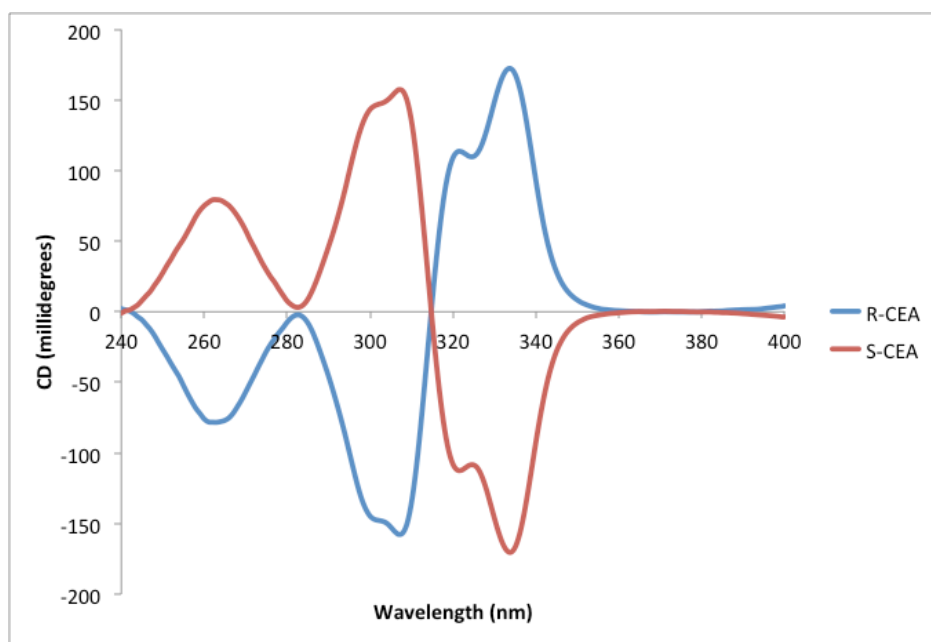


Figure 4.4. The CD curve for complex **4.2** derived from **CEA**.

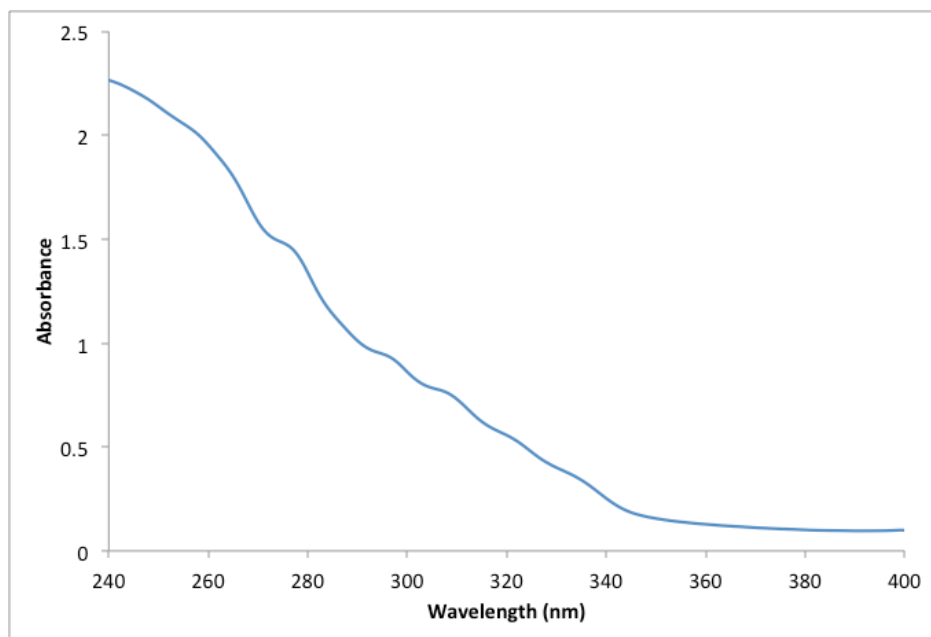


Figure 4.5 The UV-*vis* spectrum for complex **4.2** derived from **CEA**.

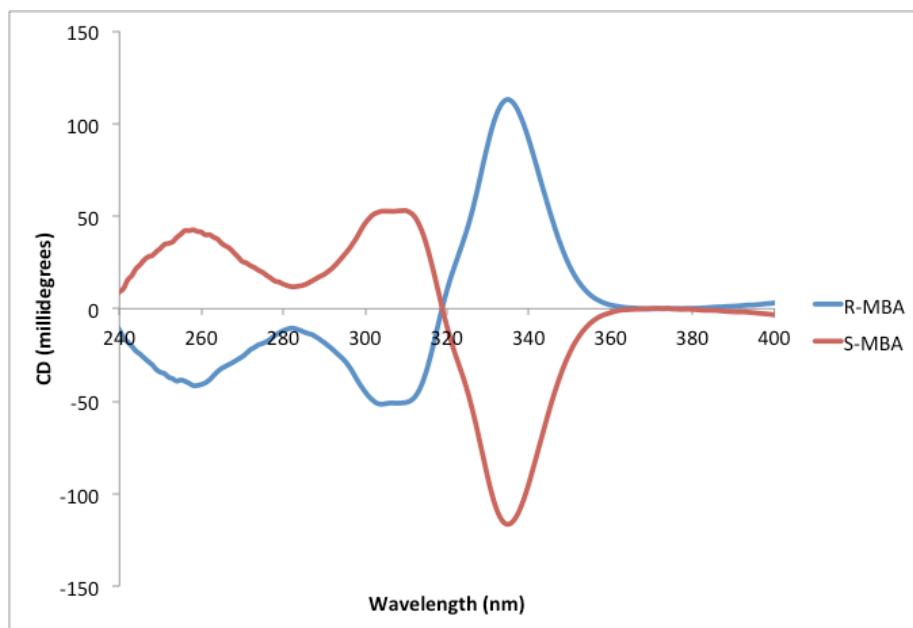


Figure 4.6. The CD curve for complex **4.2** derived from **MBA**.

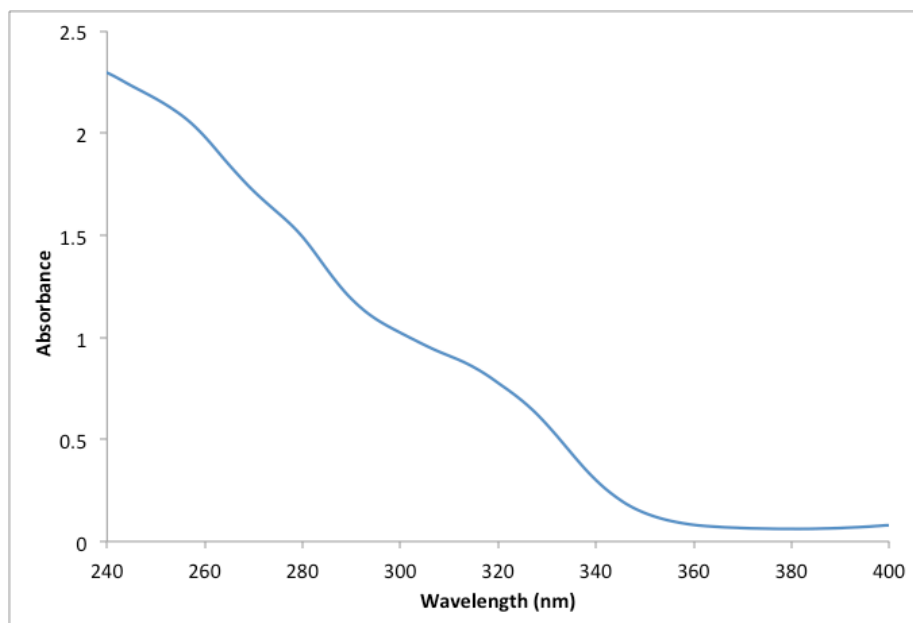


Figure 4.7. The UV-*vis* spectrum for complex **4.2** derived from **MBA**.

In order to further assess whether the CD signal was the result of exciton coupling, crystal structures were obtained for the imine complex derived from **CEA** (Figure 4.8) and **MBA**

(Figure 4.9). The angle between the planes defined by the three  $sp^2$  hybridized nitrogens on the two diimines was measured using Mercury<sup>®</sup>.

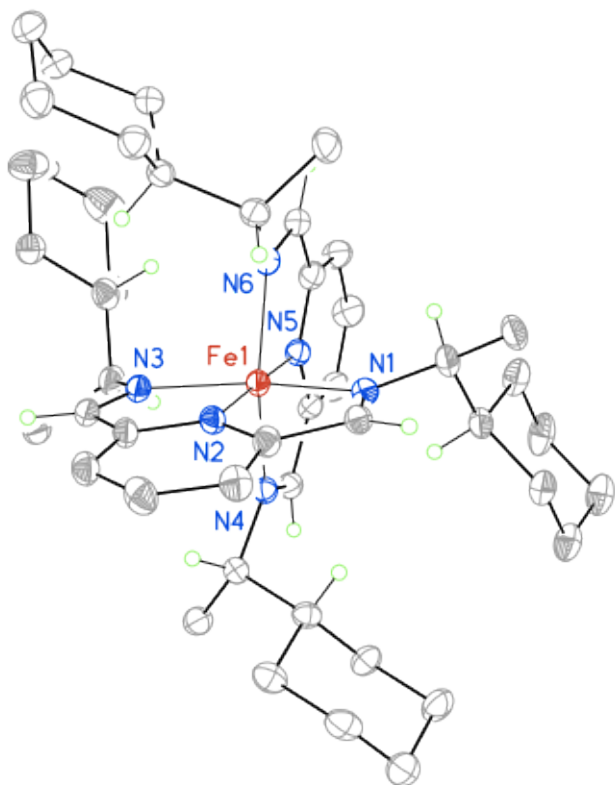


Figure 4.8. A crystal structure of the *S*-CEA derivative of complex **4.2** showing a partial atom labeling scheme. Displacement ellipsoids are scaled to the 50% probability level. Most hydrogen atoms were removed for clarity.

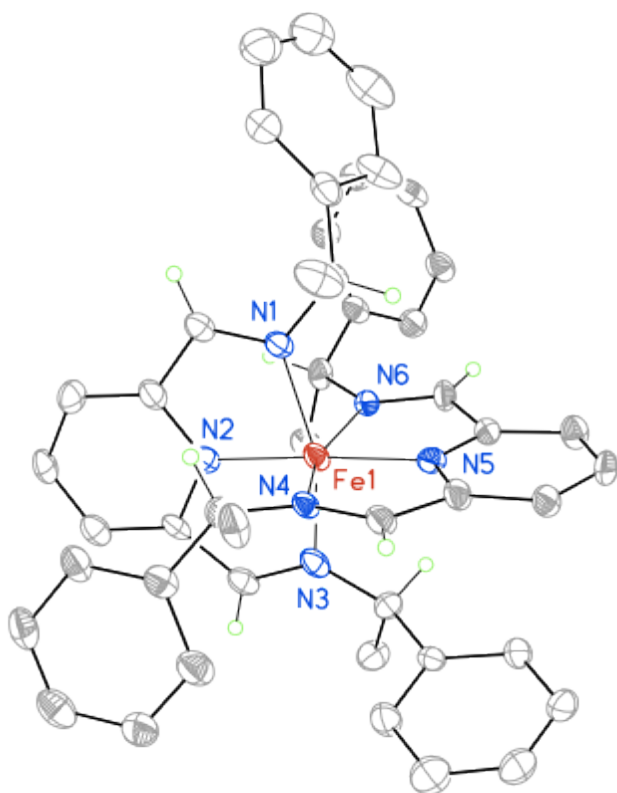


Figure 4.9. A crystal structure of the *R*-MBA derivative of complex **4.2** showing a partial atom labeling scheme. Displacement ellipsoids are scaled to the 50% probability level. Most hydrogen atoms were removed for clarity.

In the case of *S*-CEA, the dihedral angle between the imines is negative. If the CD curve is the result of ECCD, the negative dihedral angle should give a negative first Cotton effect. Indeed, the first Cotton effect is negative for the imine complex derived from *S*-CEA, which provides evidence that the signal may be the result of ECCD.

The imine complex derived from *R*-MBA, has a negative dihedral angle between the imines. If the CD curve is the result of ECCD, the imine complex derived from *R*-MBA should have a negative first Cotton effect, which is not the case. As previously mentioned, imine complexes derived from *R* enantiomers always result in a positive first Cotton effect. Thus, this provides evidence that the CD signal may not be the results of ECCD. However, the CD signal

could still be the result of ECCD, since the solid state may not be representative of the solution state of the complex. It is possible that in the solution state the dihedral angle is positive.

To summarize, the first Cotton effect in the UV region of the spectrum varies predictably with the absolute configuration of the imines. The proximity of the two diimines, and the bisignate nature of the CD curves make it possible that the CD signals are the result of ECCD. However, no absorption maxima in the UV spectrum aligns with the null of the bisignate CD curve, which is evidence against the CD curve arising from exciton coupling. However, it is also possible that the transition leading to the ECCD arises from a weak transition that cannot be seen in the UV spectrum. A crystal structure of the imine complex derived from *S*-**CEA** shows that the dihedral angle between the imines agrees with the sign of the first Cotton effect in the CD spectrum. However, the crystal structure of the imine complex derived from *R*-**CEA** has a dihedral angle that does not agree with the sign of the first Cotton effect in the CD spectrum.

Because of the proximity of the two dimines in space, and the chiral environment of the two diimines, one would expect to see ECCD. However, apart from the bisignate nature of the CD curves, there is little experimental evidence of ECCD, and thus it is difficult to definitively assign whether the CD curves arise from ECCD.

#### 4.2.6 Linear Discriminant Analysis

Linear discriminant analysis (LDA) is a useful tool for reducing complex multidimensional systems to simple lesser dimensional projections. Here we use it to extract information about the relationship between the primary optical data and the stereogenicity and identity of the amines. LDA could be used to differentiate between the handedness and identity of all the amines studied (Figure 4.10). This is particularly impressive for structurally similar amines such as **dMBA** and **MBA**, which differ only in that **dMBA** has a methyl group ortho to the stereogenic center as opposed to a hydrogen as in the case of **MBA**. It is also clear that while structurally similar amines can be cleanly differentiated by LDA, they also group together. For

example the aliphatic amines **CEA** and **SBA** are clustered around the center of the plot whereas the aromatic amines **MBA** and **dMBA** are clustered further out on the F2 axis.

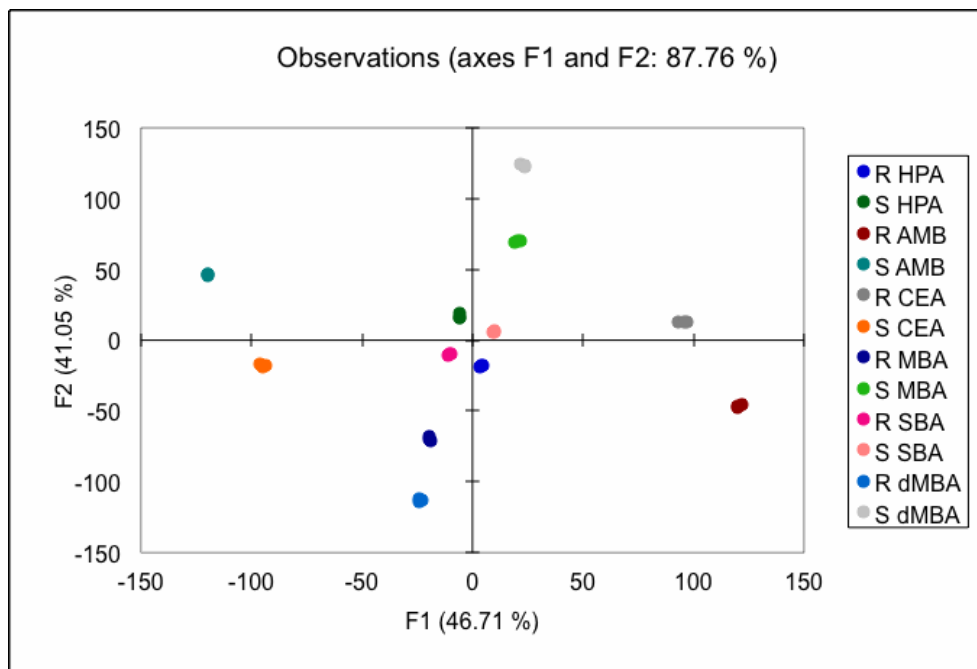


Figure 4.10. An LDA plot of the CD primary optical data from 275-310nm, 320-340nm, 415-435nm, 465-485nm, 540-560nm, 580-600nm, 620-640nm, and 720-740nm for the different amine analytes.

#### 4.2.7 Calibration Curves and Test Samples

Calibration curves were made for each analyte by plotting the ellipticity at a single wavelength as a function of  $ee$ . The resulting data was fit using third degree polynomial regression in Microsoft® Excel®.

Unknowns for all six amines at a variety of  $ee$  values were prepared from enantiomerically pure solutions, and thus their  $ee$  was known. CD spectra were collected and the ellipticity values at the appropriate wavelength were input into the previously calculated third degree polynomial used for fitting the calibration data. The resulting equation could then be

solved for  $ee$ . The results are summarized in Table 4.2. On average, the assay could be used to determine  $ee$  with an absolute error of approximately 6%.

Analyte	Experimental	Actual	Absolute Error
MBA	-76.0	-74.3	1.7
MBA	-34.0	-35.8	1.8
MBA	18.0	17.8	0.2
MBA	40.0	40.0	0.0
MBA	80.0	79.3	0.7
MBA	-50.0	-50.7	0.7
HPA	-38.1	-46.0	7.9
HPA	61.4	72.0	10.6
HPA	-13.7	-16.0	2.3
HPA	-22.5	-28.0	5.5
HPA	7.4	4.0	3.4
HPA	-74.4	-80.0	5.6
CEA	-49.1	-44.0	5.1
CEA	-8.2	-10.0	1.8
CEA	-83.7	-84.0	0.3
CEA	41.3	28.0	13.3
CEA	77.2	54.0	23.2
CEA	114.6	88.0	26.6
dMBA	-51.2	-58.0	6.8
dMBA	-42.7	-48.0	5.3
dMBA	-0.9	-4.0	3.1
dMBA	35.6	38.0	2.4
dMBA	67.1	76.0	8.9
SBA	-72.4	-68.0	4.4
SBA	-43.3	-42.0	1.3
SBA	-13.4	-14.0	0.6
SBA	17.7	16.0	1.7
SBA	50.2	48.0	2.2
AMB	-75.2	-88.0	12.8
AMB	-35.3	-40.0	4.7
AMB	24.9	28.0	3.1
AMB	42.4	44.0	1.6
AMB	80.9	100.0	19.1

Table 4.2. A summary of the experimental, actual  $ee$  values, and absolute errors for the different amines studied.



### 4.3 SUMMARY

In summary, a system was developed for sensing chirality in  $\alpha$ -chiral primary amines. The protocol uses dialdehyde **4.1**, which, in the presence of Fe(II) reacts with primary amines to form imine complex **4.2** in approximately 2 hours. Maximum signal is reached when 2-3 equivalents of aldehyde-amine (1:2 ratio of aldehyde an amine) are reacted in the presence 1 equivalent of Fe(II). After 2-3 equivalents of aldehyde-amine, the signal decreases, which may be the result of the formation of a 3:1 complex.

A bisignate CD curve is seen in the UV region of the CD spectra and the sign of the first Cotton effect varies predictably with the handedness of the amine. While the proximity of imine chromophores responsible for the signal would suggest these signals result from ECCD, there is no absorption maximum coincident with the null of the bisignate curve, which suggests the signals are just induce CD curves. The x-ray crystallographic data shows that the dihedral angle between the imines in the complex derived from *S*-CEA is correlated with the sign of the first Cotton effect in the CD spectrum. However, the dihedral angle between the imines in the complex derived from *R*-MBA does not correlate with the sign of the first Cotton effect in the CD spectrum. Thus, it is not clear whether these signals are the results of CD or ECCD.

Calibration data was collected for all six amines studied. The calibration data was fit with a third degree polynomial. CD spectral data was collected for unknown test samples, input into the polynomial equation, and the equation was solved for *ee*, which allowed for the determination of *ee* with an average absolute error of 6%.

Future studies on this system will focus on exploring the potential of other metals to act as a template for speeding up the reaction of aldehyde **4.1** with chiral amines. Additionally, methods for making the assay concentration independent will be explored.

#### 4.4 EXPERIMENTAL DETAILS AND SUPPLEMENTARY INFORMATION

Separate stock solutions of Fe(II), aldehyde **4.1**, and the appropriate amine were prepared and aliquoted into a 96-well plate. The plate was covered and allowed to sit in the dark for 2 hours, after which, the seal was removed and aliquots of solution were removed from each well and analyzed using a CD spectrometer. All measurements were taken in 0.1cm quartz cuvette.

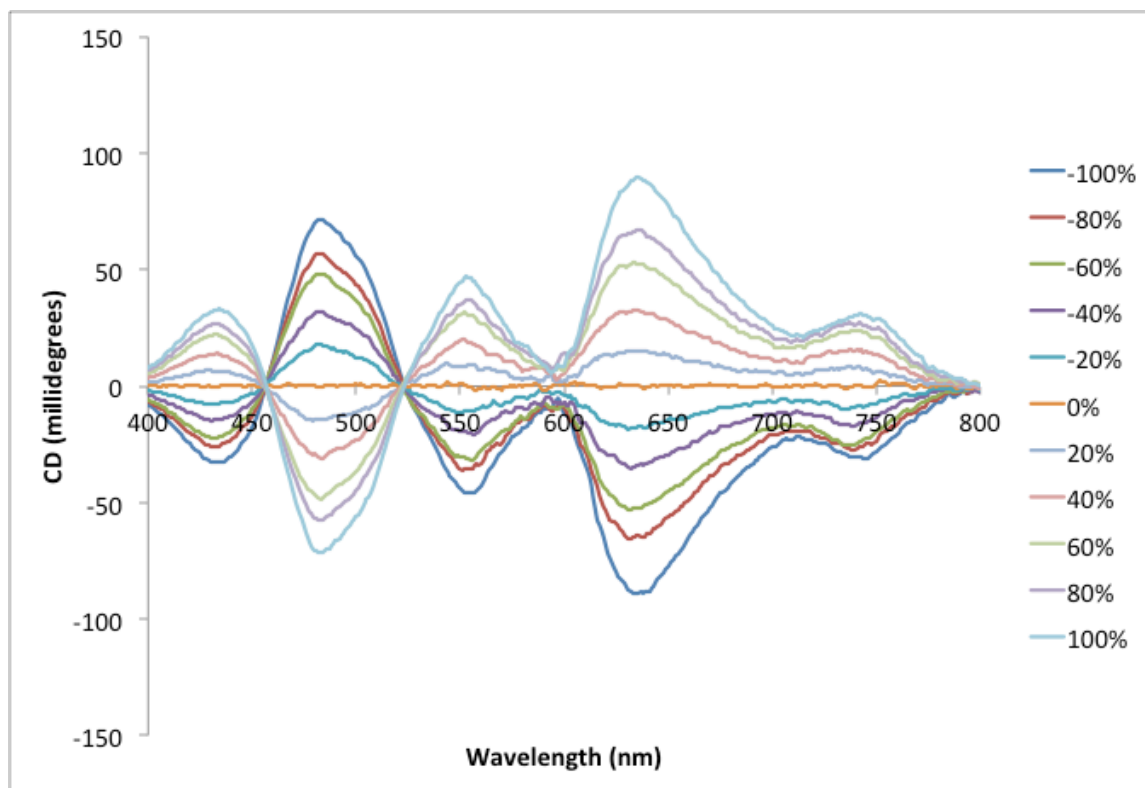


Figure 4.11. The primary CD optical data gathered for calibration curves of **MBA**.

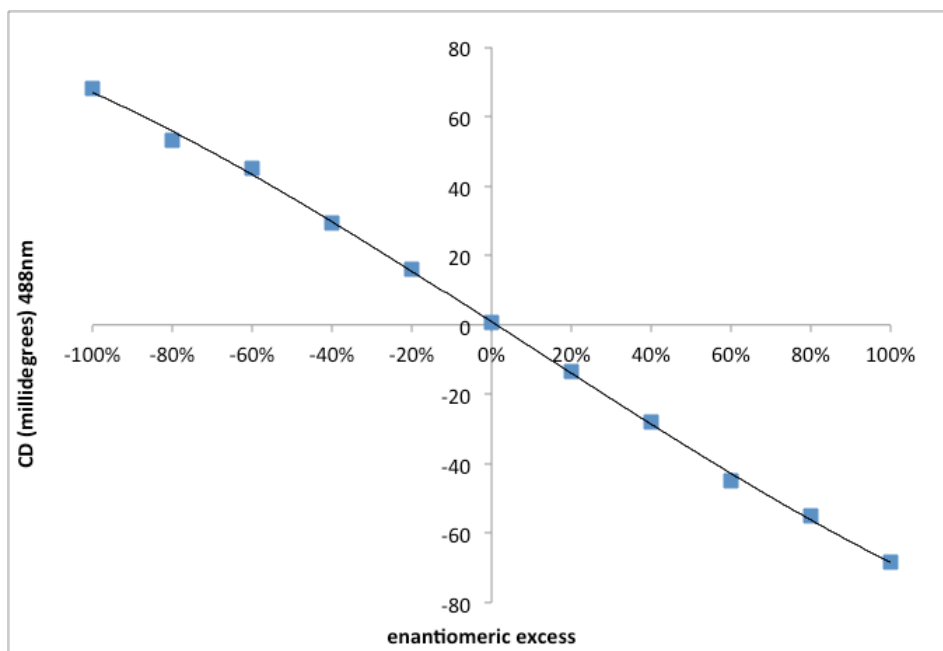


Figure 4.12. The calibration curve for **MBA**.

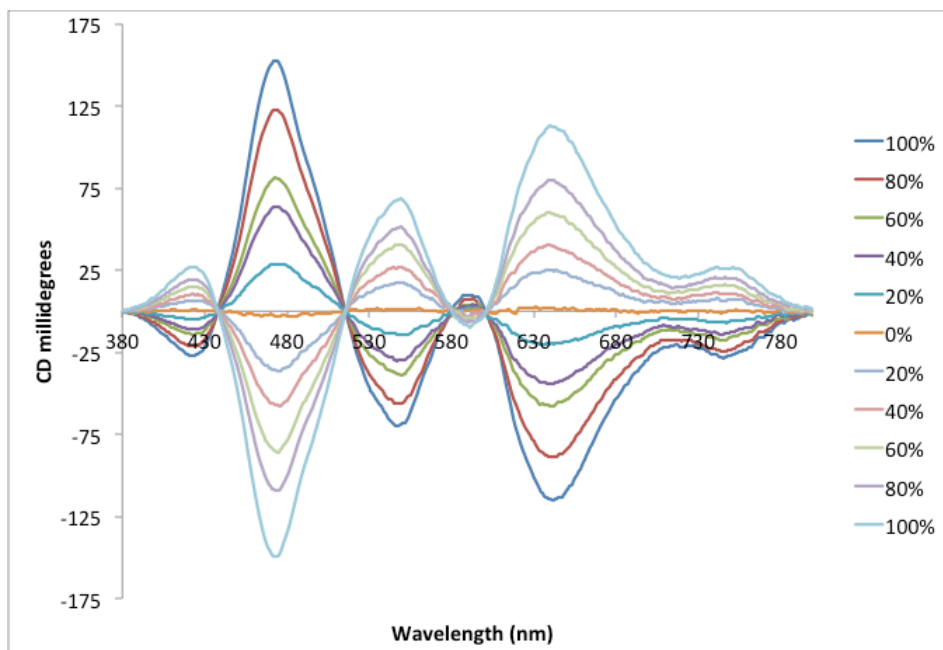


Figure 4.13. The primary CD optical data gathered for calibration curves of **CEA**.

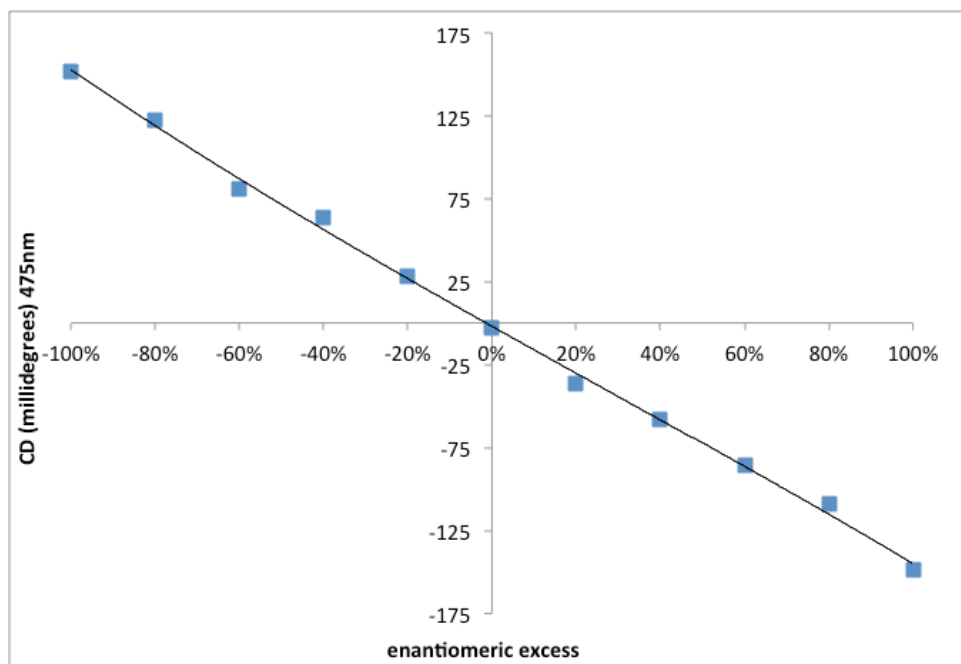


Figure 4.14. The calibration curve for **CEA**.

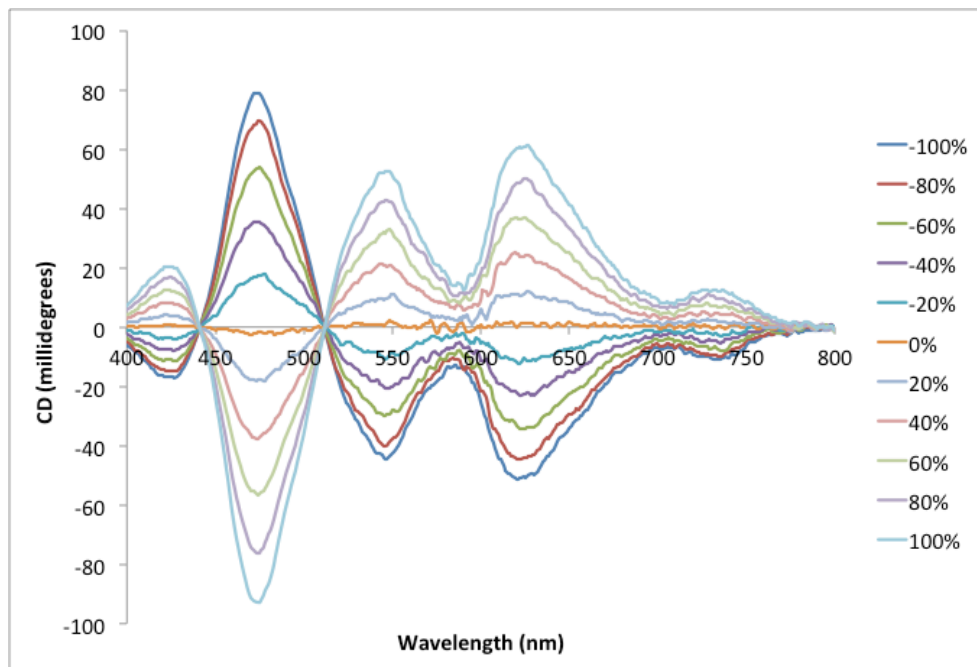


Figure 4.15. The primary CD optical data gathered for calibration curves of **HPA**.

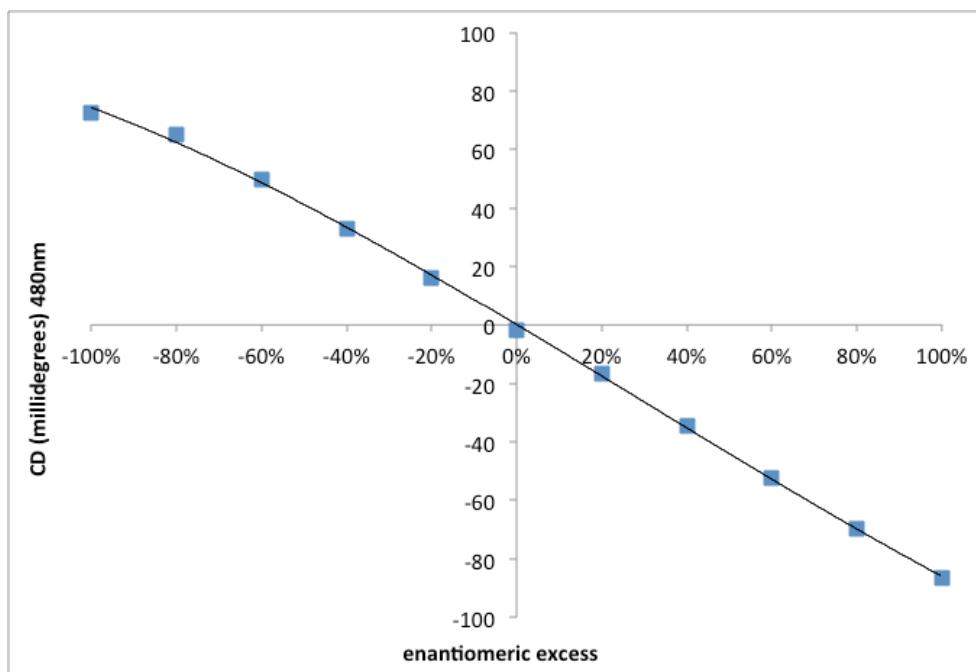


Figure 4.16. The calibration curve for **HPA**.

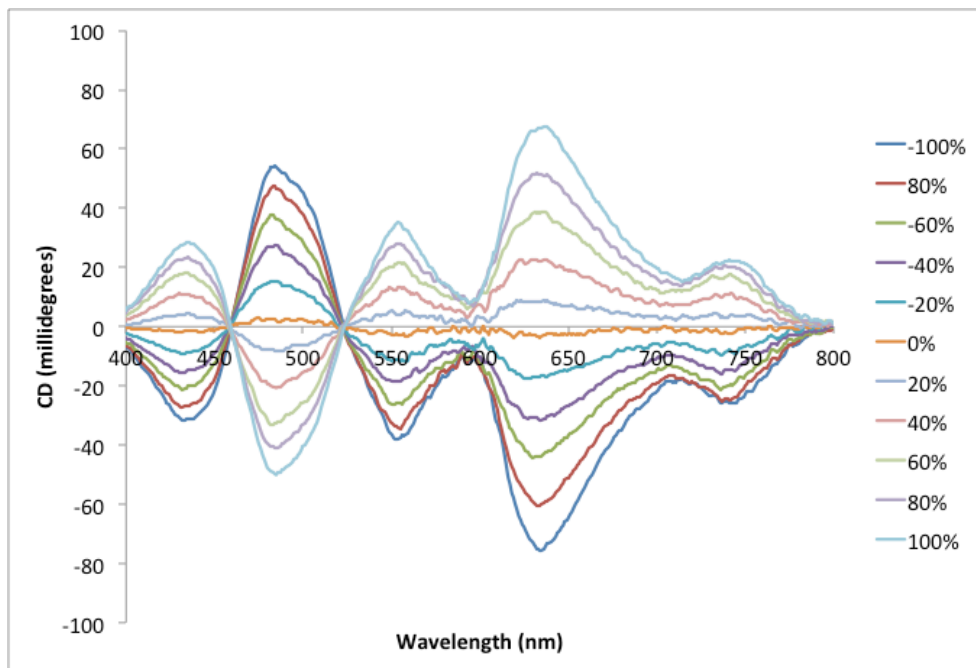


Figure 4.17. The primary CD optical data gathered for calibration curves of **dMBA**.

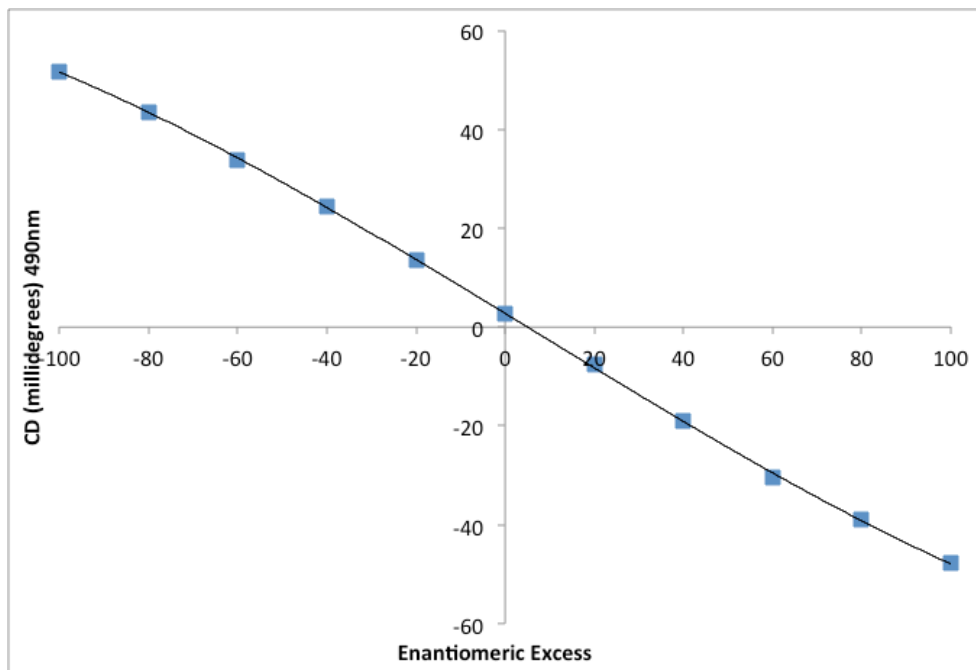


Figure 4.18. The calibration curve for **dMBA**.

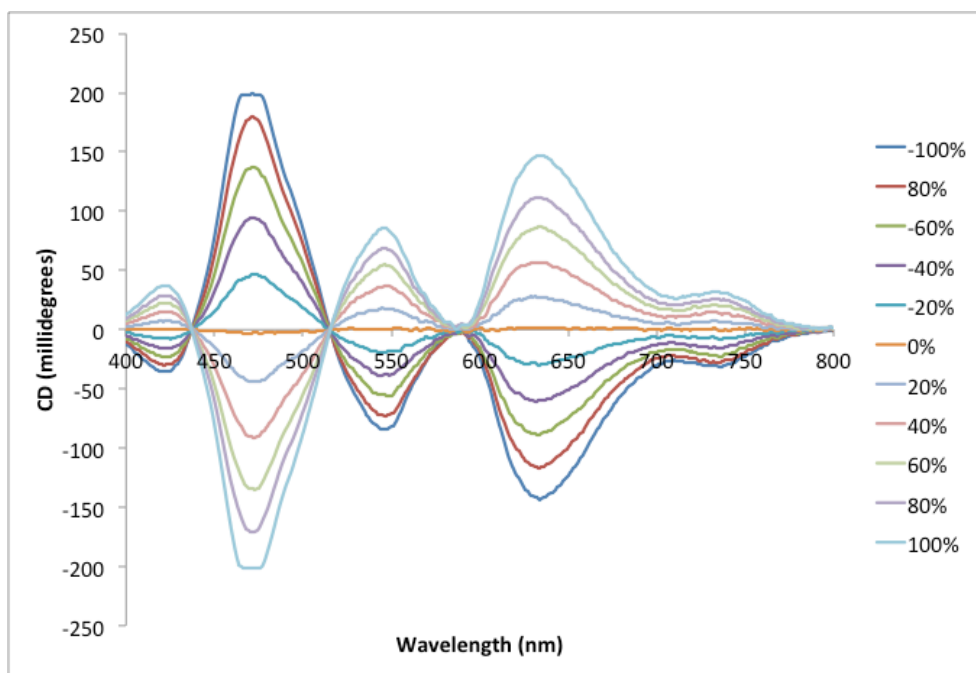


Figure 4.19. The primary CD optical data gathered for calibration curves of **AMB**.

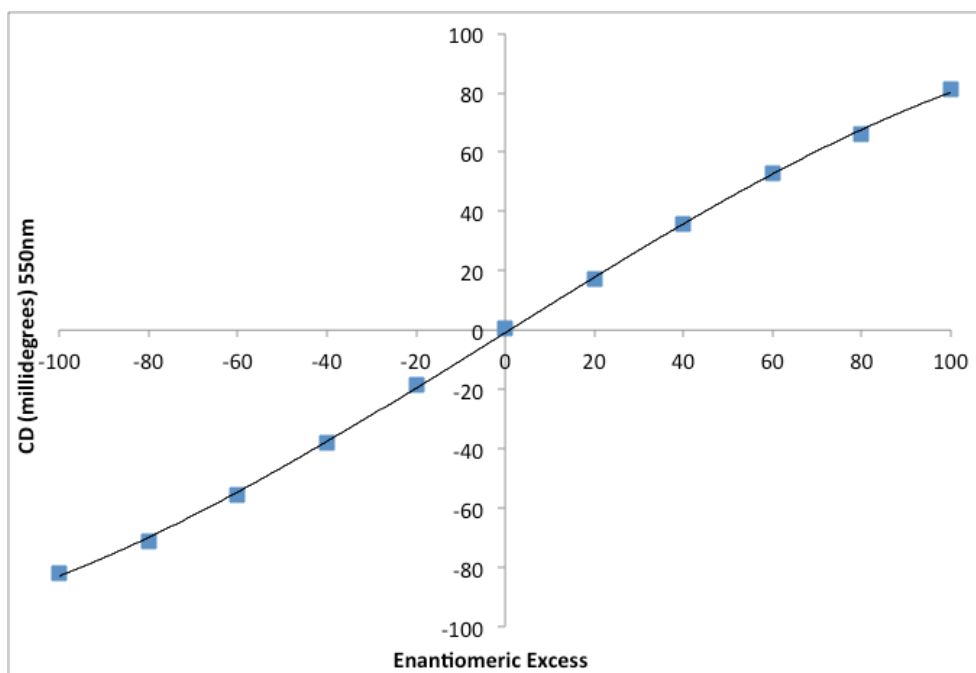


Figure 4.20. The calibration curve for **AMB**.

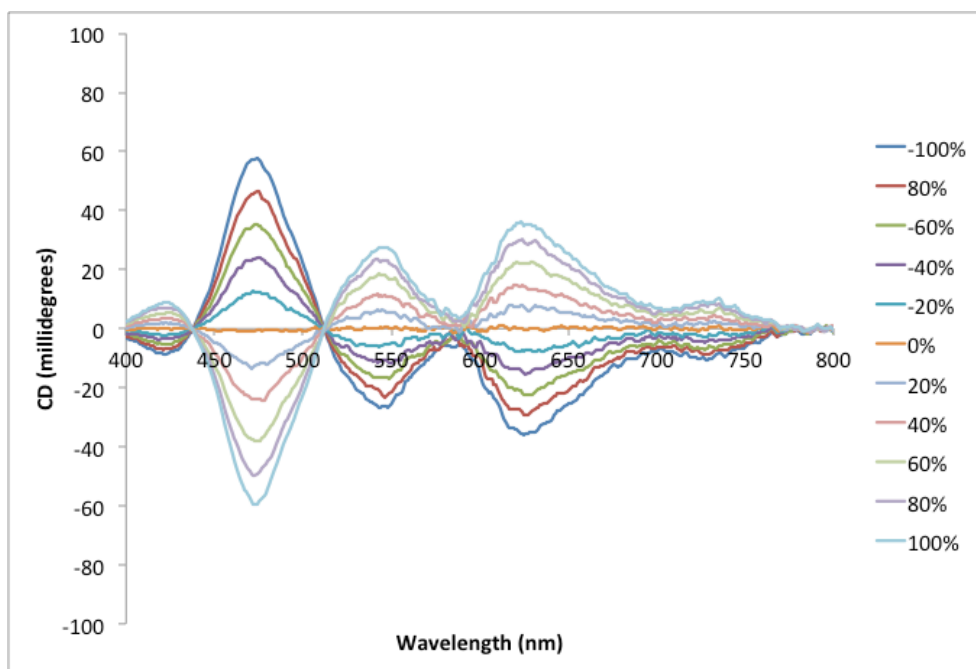


Figure 4.21. The primary CD optical data gathered for calibration curves of **SBA**.

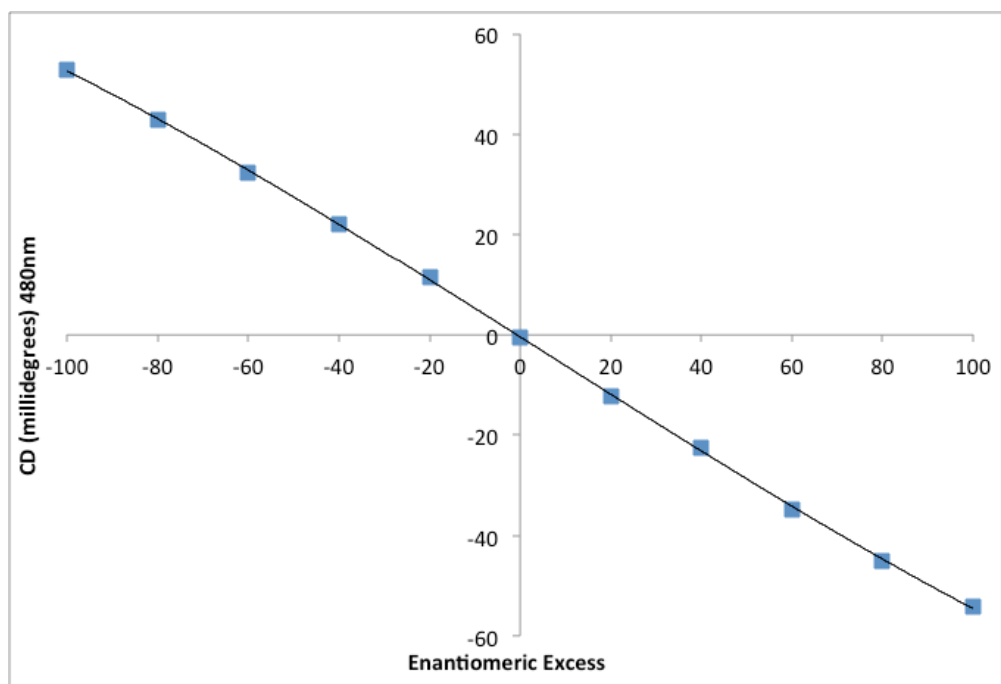


Figure 4.22. The calibration curve for **SBA**.

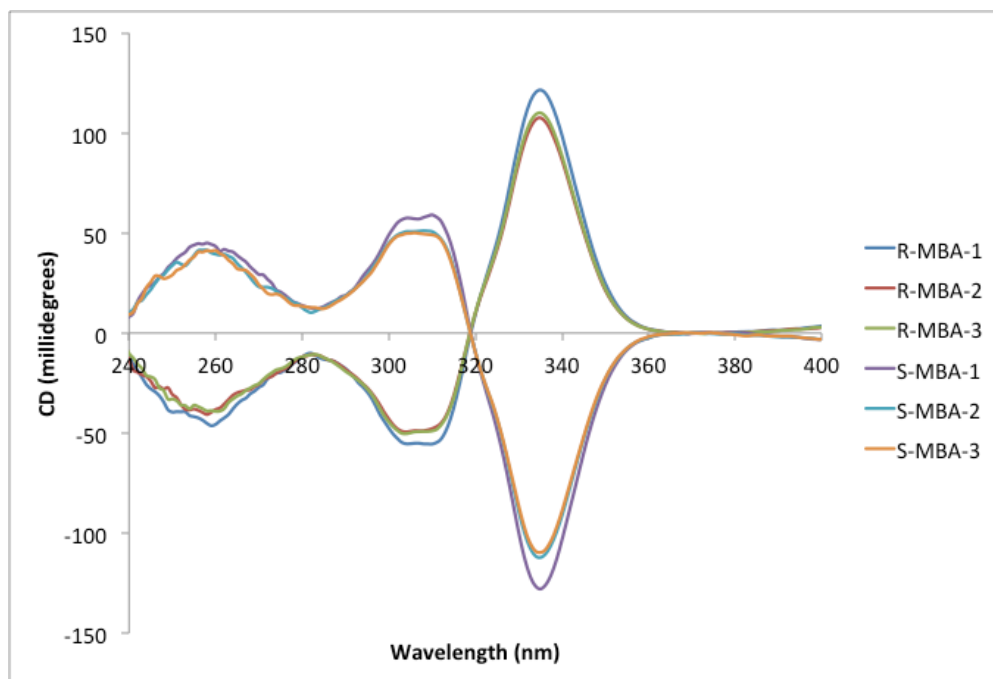


Figure 4.23. The UV-vis data collected for **MBA** for the LDA plot.



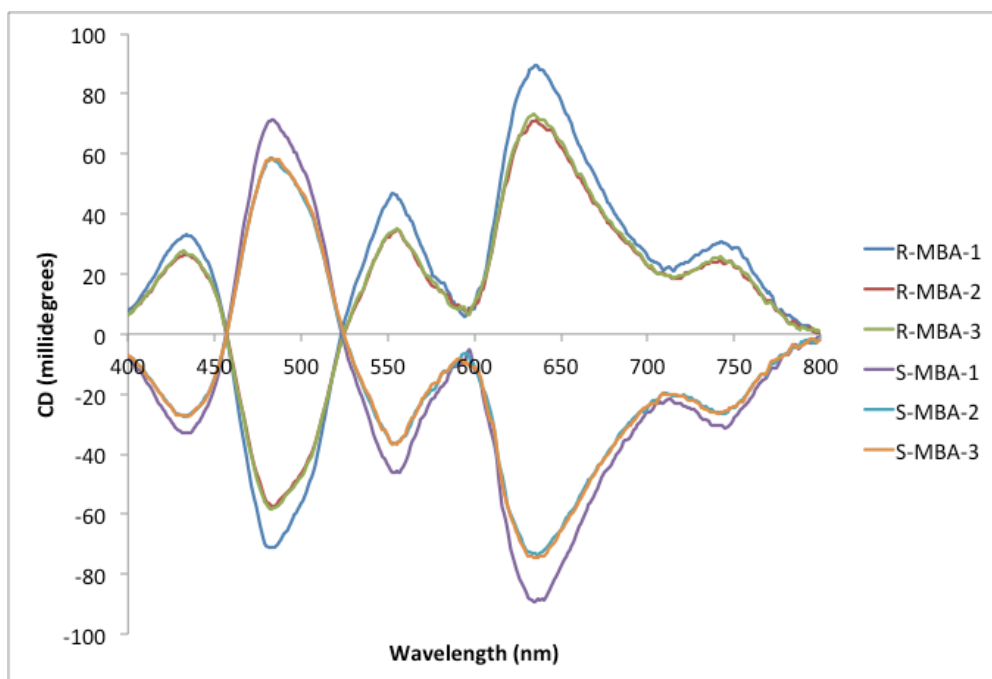


Figure 4.24. The UV-vis data collected for **MBA** for the LDA plot.

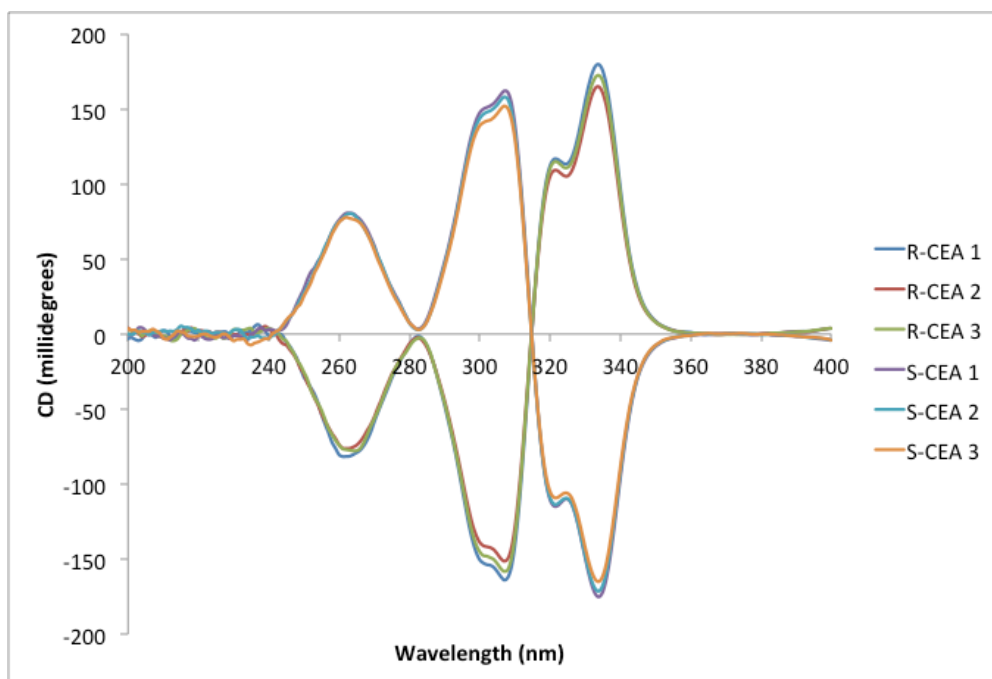


Figure 4.25. The UV-vis data collected for **CEA** for the LDA plot.

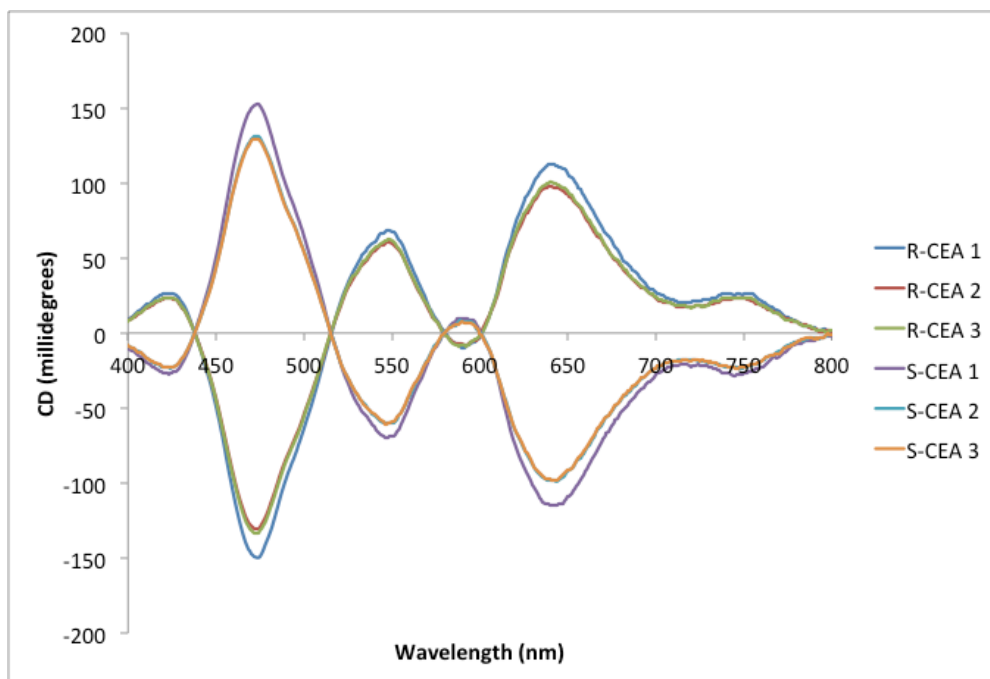
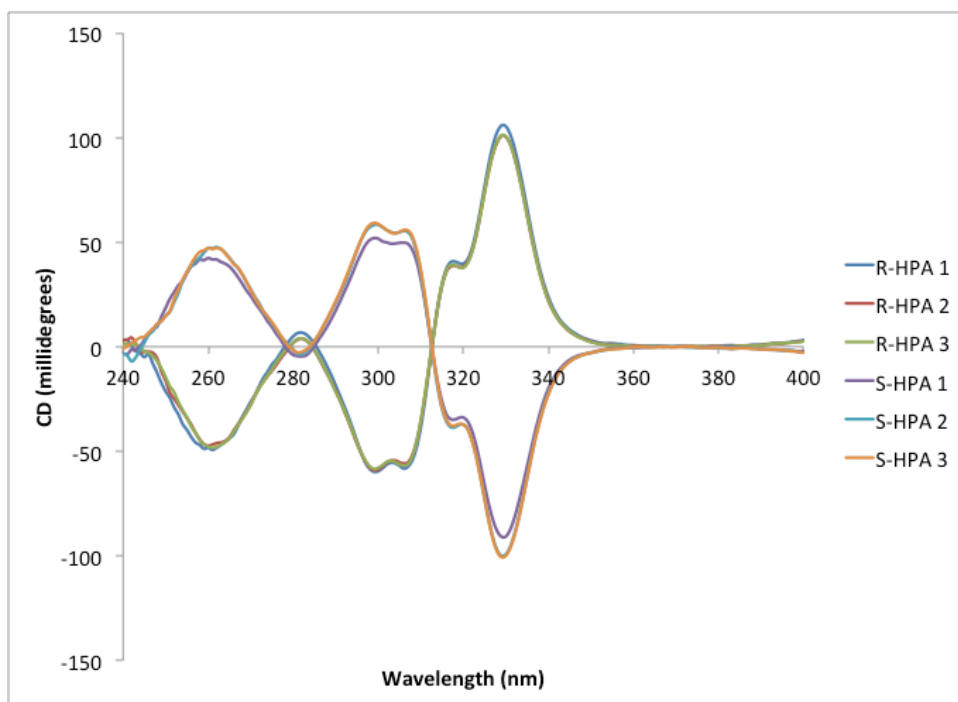


Figure 4.26. The UV-vis data collected for CEA for the LDA plot.



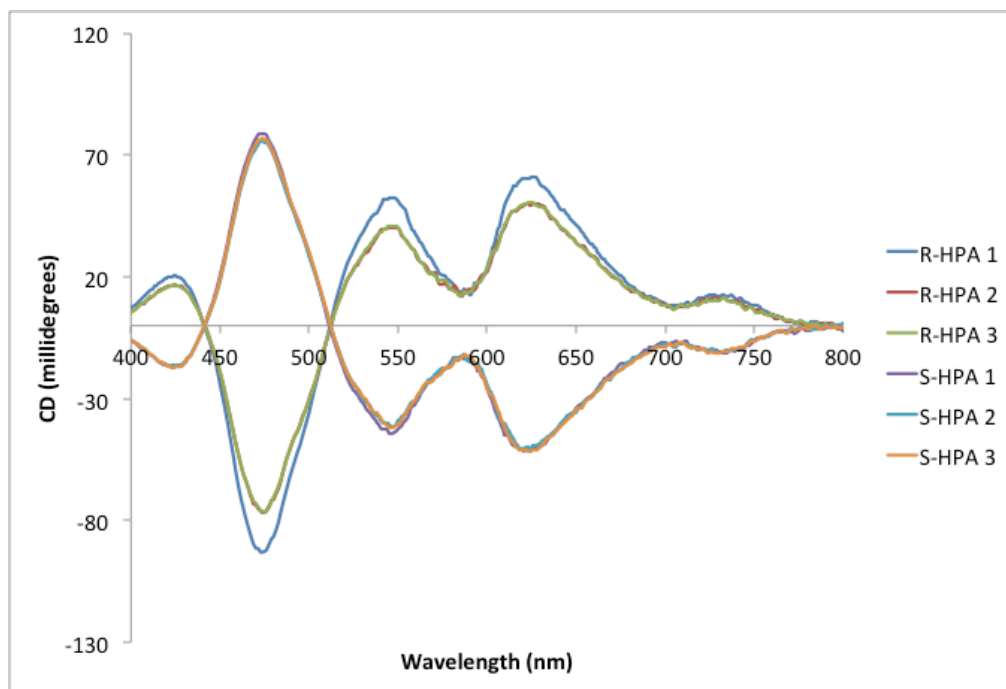


Figure 4.28. The UV-vis data collected for **HPA** for the LDA plot.

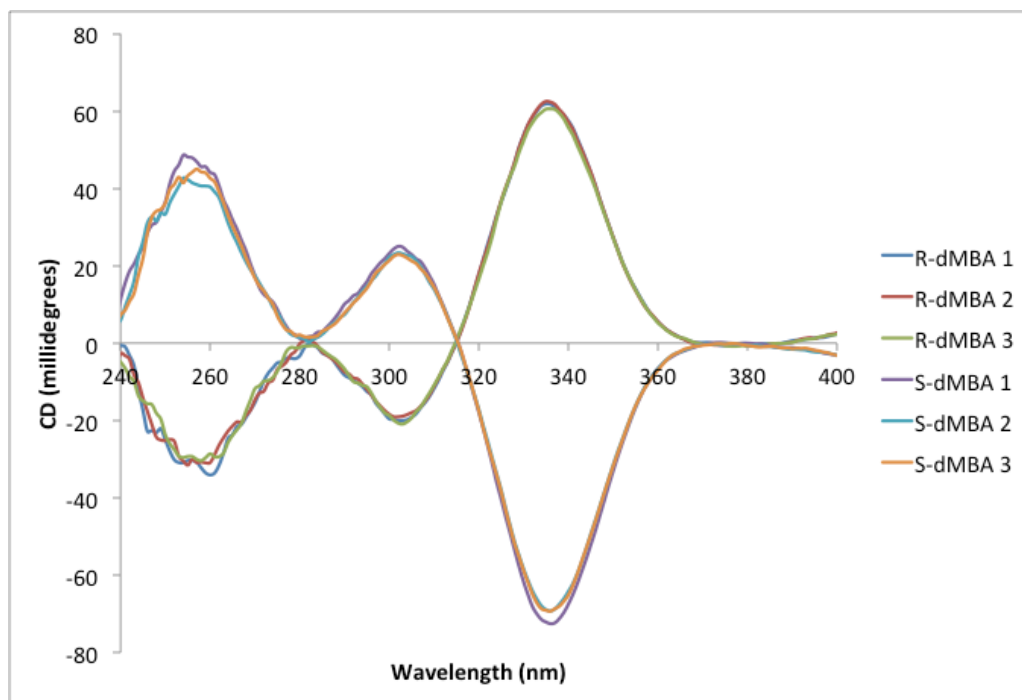


Figure 4.29. The UV-vis data collected for **dMBA** for the LDA plot.

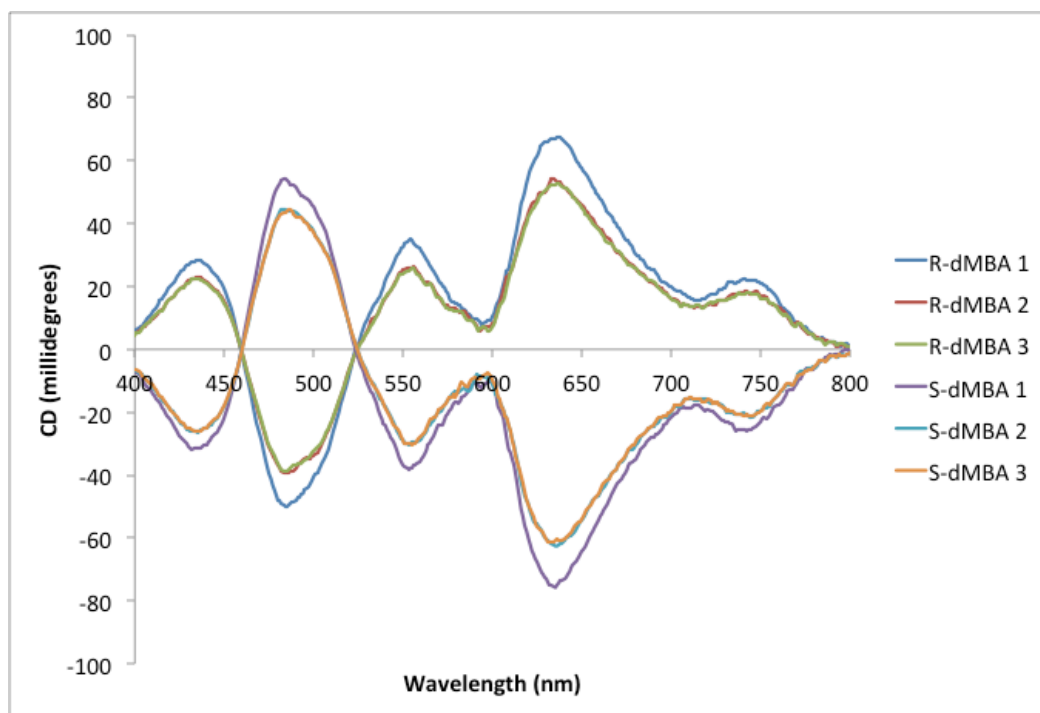


Figure 4.30. The UV-vis data collected for **dMBA** for the LDA plot.

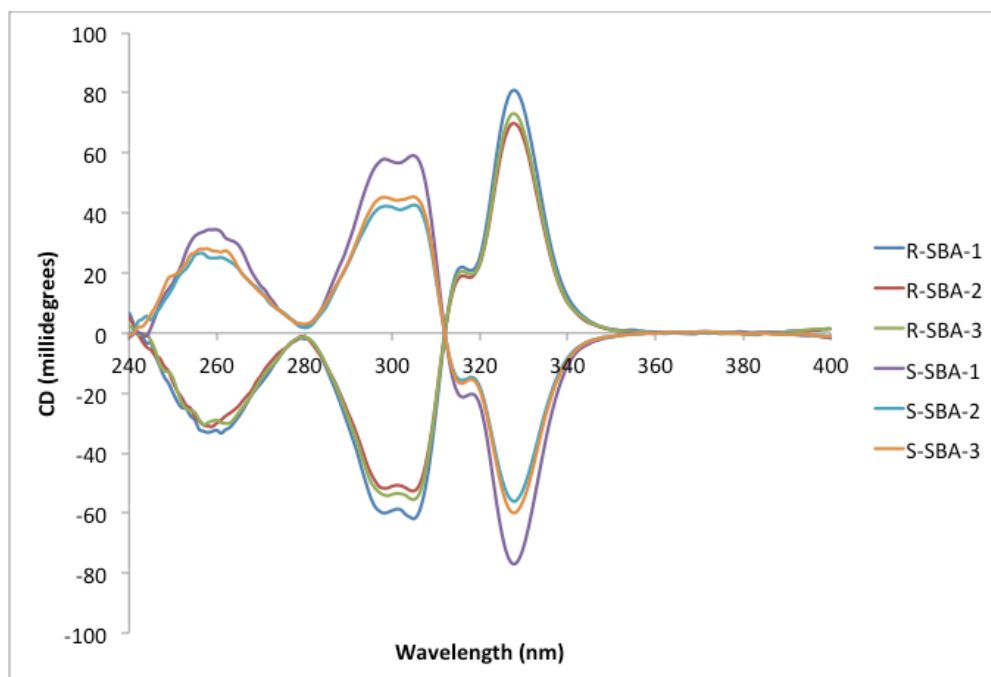


Figure 4.31. The UV-vis data collected for **SBA** for the LDA plot.

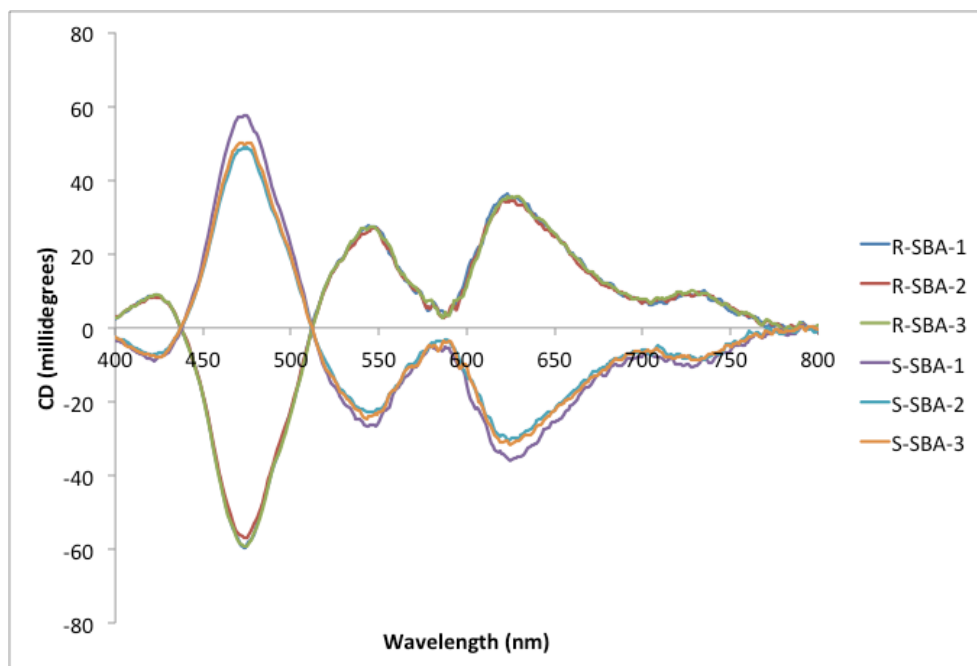


Figure 4.32. The UV-vis data collected for **SBA** for the LDA plot.

jmd\_mba\_1  
STANDARD 1H OBSERVE

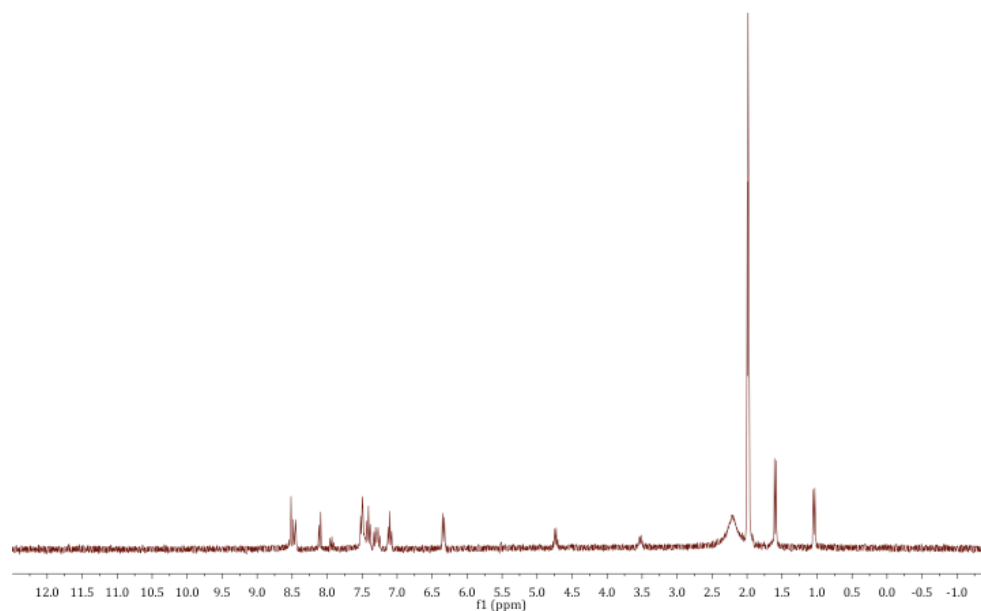


Figure 4.34.  $^1\text{H}$  NMR of the **MBA** derivative of complex **4.2**.

jmd\_dmba\_2  
STANDARD 1H OBSERVE

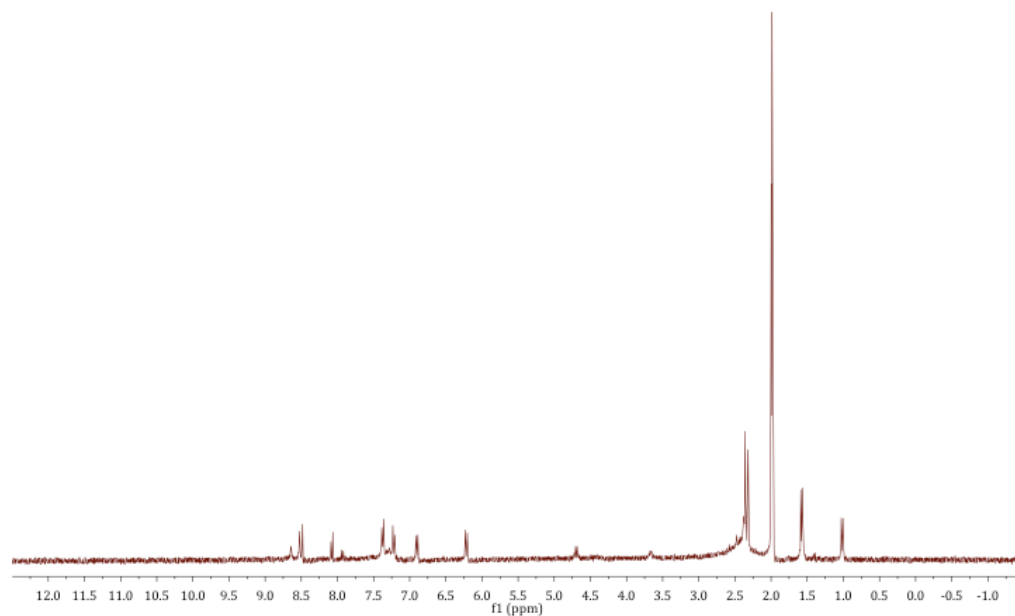


Figure 4.35. <sup>1</sup>H NMR of the **dMBA** derivative of complex **4.2**.

jmd\_cea\_3  
STANDARD 1H OBSERVE

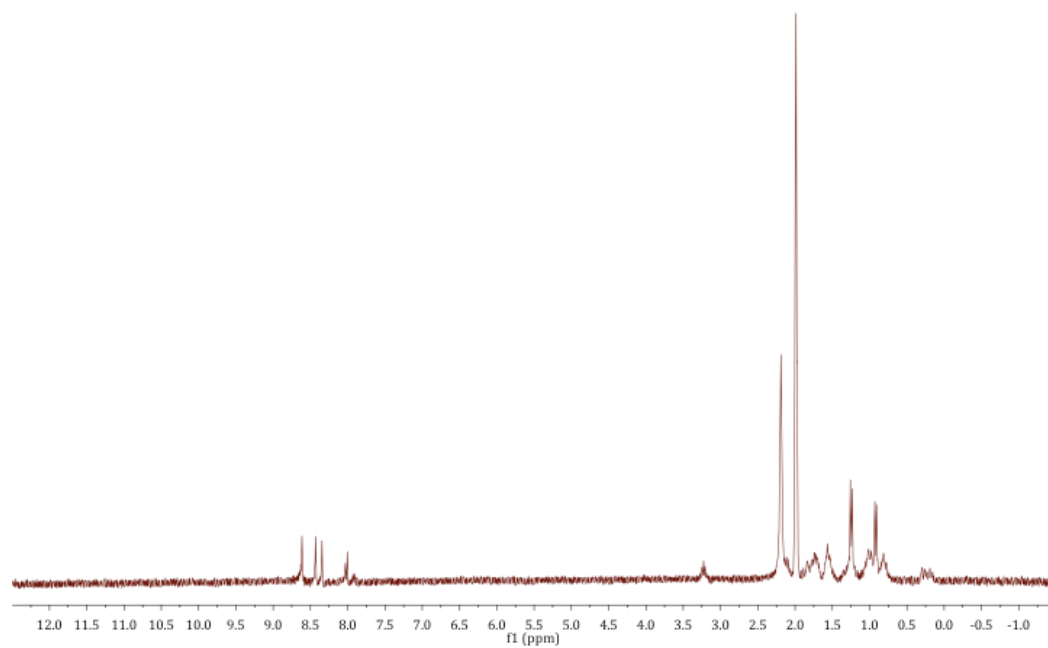


Figure 4.36. <sup>1</sup>H NMR of the **CEA** derivative of complex **4.2**.

jmd\_amb\_4  
STANDARD 1H OBSERVE

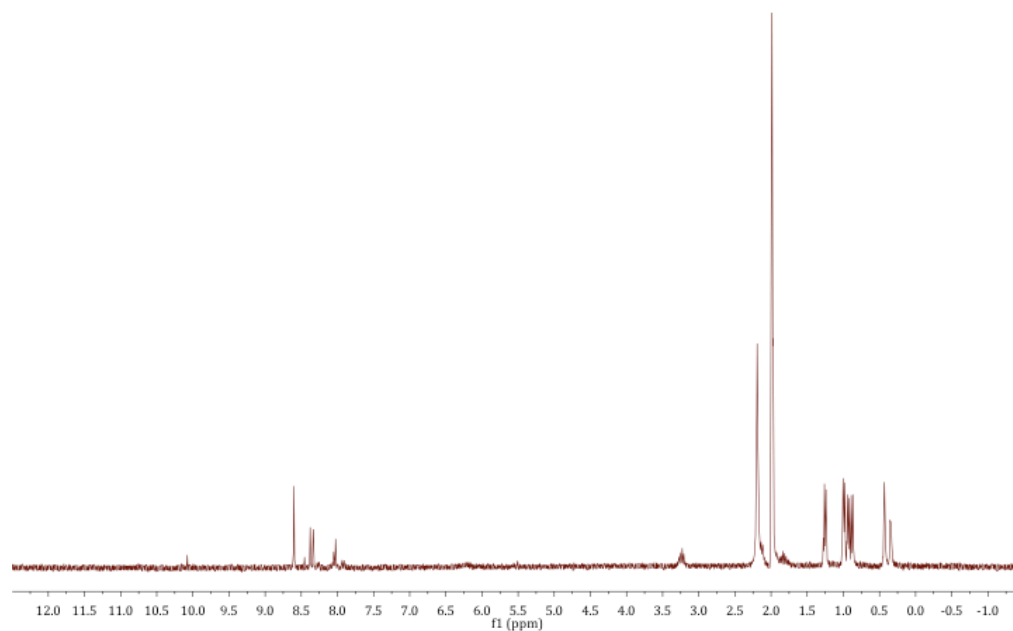


Figure 4.37. <sup>1</sup>H NMR of the **AMB** derivative of complex **4.2**.

jmd\_hpa\_5  
STANDARD 1H OBSERVE

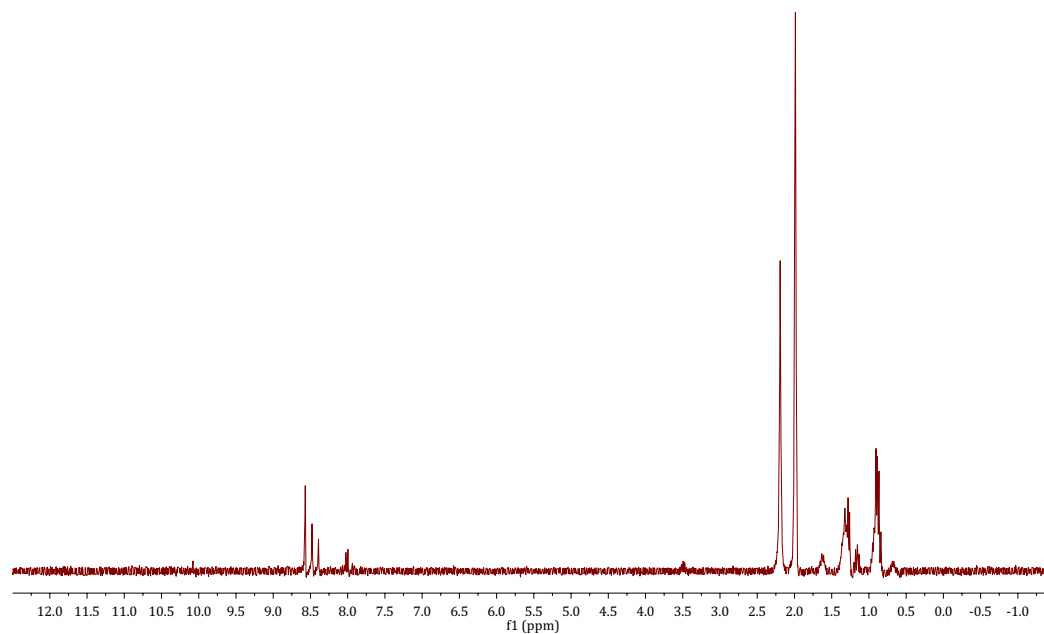


Figure 4.38. <sup>1</sup>H NMR of the **HPA** derivative of complex **4.2**.

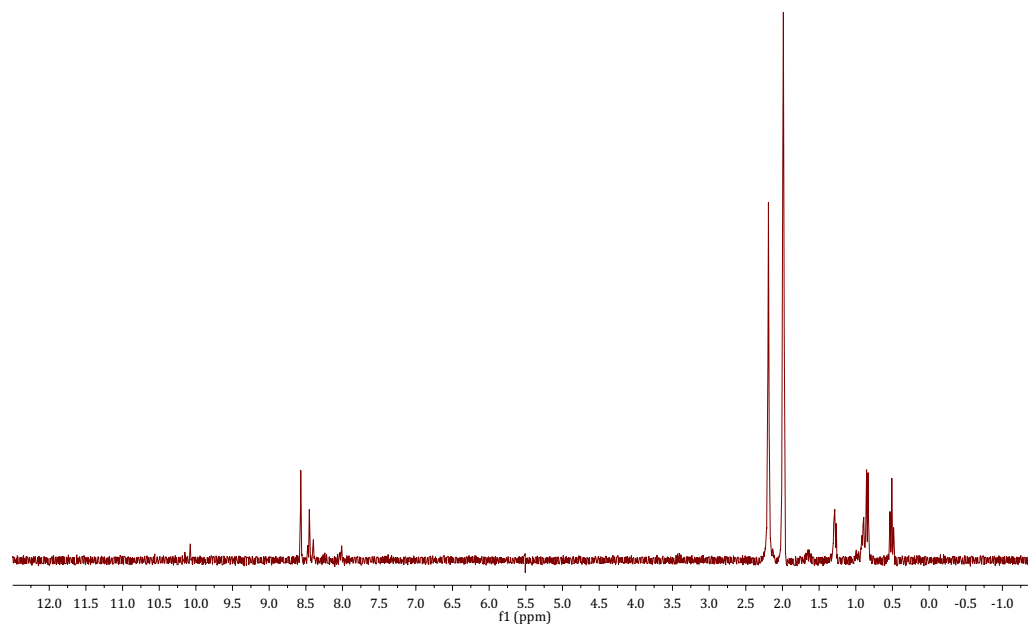


Figure 4.39. <sup>1</sup>H NMR of the **SBA** derivative of complex **4.2**.

Empirical formula	C <sub>50</sub> H <sub>49</sub> F <sub>6</sub> Fe N <sub>7</sub> O <sub>6</sub> S <sub>2</sub>	
Formula weight	1077.93	
Temperature	153(2) K	
Wavelength	0.71075 Å	
Crystal system	Monoclinic	
Space group	P21	
Unit cell dimensions	a = 13.8229(15) Å	α = 90°.
	b = 13.0621(12) Å	β = 97.510(6)°.
	c = 13.8292(13) Å	γ = 90°.
Volume	2475.5(4) Å <sup>3</sup>	
Z	2	
Density (calculated)	1.446 Mg/m <sup>3</sup>	
Absorption coefficient	0.469 mm <sup>-1</sup>	
F(000)	1116	
Crystal size	0.25 x 0.20 x 0.13 mm <sup>3</sup>	



Theta range for data collection	1.49 to 27.50°.
Index ranges	-17<=h<=17, -16<=k<=16, -17<=l<=17
Reflections collected	11211
Independent reflections	11211 [R(int) = 0.0000]
Completeness to theta = 27.50°	99.5 %
Absorption correction	Semi-empirical from equivalents
Max. and min. transmission	1.06 and 0.904
Refinement method	Full-matrix least-squares on F <sup>2</sup>
Data / restraints / parameters	11211 / 19 / 654
Goodness-of-fit on F <sup>2</sup>	1.149
Final R indices [I>2sigma(I)]	R1 = 0.0749, wR2 = 0.1525
R indices (all data)	R1 = 0.1466, wR2 = 0.1970
Absolute structure parameter	-0.04(3)
Largest diff. peak and hole	0.415 and -0.913 e.Å <sup>-3</sup>

Table 4.3. Crystal data and structure refinement for the **R-MBA** derivative of complex **4.2**.

	x	y	z	U(eq)
Fe1	6967(1)	2088(1)	8088(1)	33(1)
N1	5520(6)	1982(6)	7914(5)	33(2)
N2	6636(6)	3419(6)	7685(6)	36(2)
N3	8315(7)	2728(6)	8244(6)	40(2)
N4	6976(5)	1447(6)	6775(5)	30(2)
N5	7364(6)	755(5)	8461(5)	31(2)
N6	6962(6)	2179(6)	9523(6)	33(2)
S1	3599(2)	2955(2)	4933(2)	50(1)
F1	1745(5)	3455(5)	4584(6)	72(2)
F2	2143(5)	2070(6)	3891(5)	84(2)
F3	2019(6)	2073(7)	5404(6)	87(2)
O1	3651(7)	3528(6)	5829(6)	70(2)
O2	3739(6)	3560(5)	4105(6)	65(2)
O3	4092(6)	1987(6)	4991(6)	70(2)
C47	2322(8)	2634(8)	4697(9)	54(3)
S2	9899(2)	1320(2)	1706(2)	51(1)
F4	8807(5)	1448(6)	3113(5)	79(2)
F5	10014(8)	2480(6)	3259(6)	94(3)
F6	10263(6)	890(7)	3555(6)	91(3)
O4	10938(6)	1523(8)	1704(7)	81(3)
O5	9614(9)	280(6)	1580(8)	90(3)
O6	9256(6)	2050(7)	1203(5)	68(2)
C48	9777(11)	1558(10)	3006(11)	70(4)
C1	5052(8)	2802(7)	7619(7)	37(2)
C2	5683(8)	3701(7)	7469(8)	42(3)
C3	5415(8)	4653(7)	7139(8)	44(3)
C4	6160(8)	5364(7)	7062(7)	43(3)
C5	7135(9)	5132(8)	7302(7)	43(3)
C6	7358(8)	4125(7)	7598(7)	34(2)
C7	8299(7)	3680(7)	7970(7)	38(2)
C8	4933(7)	1021(7)	8042(7)	35(2)
C9	4616(10)	524(9)	7068(9)	63(4)

C10	4109(8)	1198(9)	8673(8)	47(3)
C11	3141(9)	1456(9)	8216(11)	64(4)
C12	2384(11)	1566(10)	8758(15)	80(5)
C13	2562(15)	1468(11)	9717(17)	92(5)
C14	3467(17)	1193(13)	10220(11)	104(7)
C15	4303(11)	1070(11)	9655(10)	74(4)
C16	9192(7)	2254(7)	8774(7)	37(2)
C17	9999(7)	3018(8)	9174(8)	49(3)
C18	9630(7)	1443(8)	8201(7)	39(2)
C19	9865(8)	475(7)	8589(8)	43(2)
C20	10271(8)	-264(8)	8056(10)	55(3)
C21	10455(9)	-52(8)	7126(9)	60(3)
C22	10261(11)	877(10)	6730(10)	77(4)
C23	9832(9)	1655(8)	7250(8)	58(3)
C24	7275(8)	503(7)	6787(8)	42(2)
C25	7520(8)	69(7)	7767(8)	39(2)
C26	7836(8)	-914(7)	8006(7)	38(2)
C27	7967(7)	-1209(8)	8982(8)	44(3)
C28	7778(9)	-516(7)	9682(7)	41(2)
C29	7493(7)	497(7)	9399(7)	33(2)
C30	7203(8)	1339(7)	9988(7)	39(2)
C31	6531(8)	1880(7)	5818(7)	41(2)
C32	6363(9)	1086(7)	5016(7)	52(3)
C33	7085(8)	2785(7)	5518(8)	43(3)
C34	6638(9)	3685(8)	5256(7)	50(3)
C35	7163(11)	4512(9)	4954(9)	61(3)
C36	8160(10)	4437(9)	4961(8)	60(3)
C37	8631(10)	3538(10)	5215(9)	66(4)
C38	8110(10)	2682(9)	5489(9)	59(3)
C39	6684(8)	3119(7)	10037(7)	37(2)
C40	7611(8)	3815(8)	10216(8)	50(3)
C41	6275(8)	2944(7)	10972(7)	37(2)
C42	5266(8)	3077(7)	11012(8)	42(2)
C43	4873(9)	2962(8)	11879(9)	52(3)
C44	5466(10)	2749(8)	12719(9)	57(3)
C45	6487(9)	2643(9)	12715(8)	50(3)

C46	6880(8)	2741(8)	11847(8)	45(3)
N1A	6680(12)	-412(13)	11756(12)	110(4)
C2A	7403(15)	-650(13)	12350(14)	97(5)
C3A	8165(16)	-966(16)	12958(15)	136(7)

---

Table 4.4. Atomic coordinates ( $\times 10^4$ ) and equivalent isotropic displacement parameters ( $\text{\AA}^2 \times 10^3$ ) for the **R-MBA** derivative of complex **4.2**.  $U(\text{eq})$  is defined as one third of the trace of the orthogonalized  $U^{ij}$  tensor.

---

Fe1-N2	1.865(8)	C3-C4	1.402(15)
Fe1-N5	1.877(7)	C3-H3	0.95
Fe1-N1	1.988(8)	C4-C5	1.378(15)
Fe1-N6	1.989(8)	C4-H4	0.95
Fe1-N4	2.000(7)	C5-C6	1.401(14)
Fe1-N3	2.029(9)	C5-H5	0.95
N1-C1	1.290(13)	C6-C7	1.455(14)
N1-C8	1.517(11)	C7-H7	0.95
N2-C2	1.363(14)	C8-C9	1.507(15)
N2-C6	1.376(12)	C8-C10	1.541(15)
N3-C7	1.299(12)	C8-H8	1.00
N3-C16	1.469(13)	C9-H9A	0.98
N4-C24	1.299(12)	C9-H9B	0.98
N4-C31	1.497(12)	C9-H9C	0.98
N5-C29	1.329(12)	C10-C15	1.359(18)
N5-C25	1.351(12)	C10-C11	1.443(17)
N6-C30	1.294(12)	C11-C12	1.372(18)
N6-C39	1.494(12)	C11-H11	0.95
S1-O2	1.425(8)	C12-C13	1.32(3)
S1-O3	1.434(8)	C12-H12	0.95
S1-O1	1.443(8)	C13-C14	1.40(3)
S1-C47	1.802(11)	C13-H13	0.95
F1-C47	1.333(12)	C14-C15	1.49(2)
F2-C47	1.332(14)	C14-H14	0.95
F3-C47	1.333(13)	C15-H15	0.95
S2-O5	1.420(9)	C16-C18	1.498(12)
S2-O6	1.421(8)	C16-C17	1.545(13)
S2-O4	1.460(9)	C16-H16	1.00
S2-C48	1.854(14)	C17-H17A	0.98
F4-C48	1.376(15)	C17-H17B	0.98
F5-C48	1.284(14)	C17-H17C	0.98
F6-C48	1.286(16)	C18-C19	1.395(14)
C1-C2	1.493(14)	C18-C23	1.407(14)
C1-H1	0.95	C19-C20	1.378(14)
C2-C3	1.358(14)	C19-H19	0.95

C20-C21	1.373(17)	C35-H35	0.95
C20-H20	0.95	C36-C37	1.366(18)
C21-C22	1.343(17)	C36-H36	0.95
C21-H21	0.95	C37-C38	1.408(16)
C22-C23	1.419(15)	C37-H37	0.95
C22-H22	0.95	C38-H38	0.95
C23-H23	0.95	C39-C41	1.495(13)
C24-C25	1.467(16)	C39-C40	1.564(16)
C24-H24	0.95	C39-H39	1.00
C25-C26	1.382(14)	C40-H40A	0.98
C26-C27	1.393(14)	C40-H40B	0.98
C26-H26	0.95	C40-H40C	0.98
C27-C28	1.376(14)	C41-C46	1.403(16)
C27-H27	0.95	C41-C42	1.413(15)
C28-C29	1.420(13)	C42-C43	1.387(15)
C28-H28	0.95	C42-H42	0.95
C29-C30	1.456(14)	C43-C44	1.360(18)
C30-H30	0.95	C43-H43	0.95
C31-C33	1.496(13)	C44-C45	1.419(18)
C31-C32	1.513(14)	C44-H44	0.95
C31-H31	1.00	C45-C46	1.387(14)
C32-H32A	0.98	C45-H45	0.95
C32-H32B	0.98	C46-H46	0.95
C32-H32C	0.98	N1A-C2A	1.25(2)
C33-C34	1.355(15)	C2A-C3A	1.32(3)
C33-C38	1.430(17)	C3A-H3AA	0.98
C34-C35	1.396(15)	C3A-H3AB	0.98
C34-H34	0.95	C3A-H3AC	0.98
C35-C36	1.380(19)		
N2-Fe1-N5	176.8(3)	N2-Fe1-N4	98.6(3)
N2-Fe1-N1	79.9(3)	N5-Fe1-N4	79.9(3)
N5-Fe1-N1	102.8(3)	N1-Fe1-N4	89.2(3)
N2-Fe1-N6	102.1(3)	N6-Fe1-N4	158.7(3)
N5-Fe1-N6	79.7(3)	N2-Fe1-N3	80.4(4)
N1-Fe1-N6	89.4(2)	N5-Fe1-N3	97.0(3)

N1-Fe1-N3	159.6(3)	O5-S2-C48	102.7(6)
N6-Fe1-N3	89.5(3)	O6-S2-C48	103.4(6)
N4-Fe1-N3	98.9(3)	O4-S2-C48	100.7(6)
C1-N1-C8	118.1(8)	F5-C48-F6	112.4(13)
C1-N1-Fe1	115.8(7)	F5-C48-F4	106.7(11)
C8-N1-Fe1	126.1(6)	F6-C48-F4	107.8(11)
C2-N2-C6	119.5(8)	F5-C48-S2	111.6(10)
C2-N2-Fe1	120.7(6)	F6-C48-S2	110.6(9)
C6-N2-Fe1	119.8(7)	F4-C48-S2	107.5(9)
C7-N3-C16	122.2(9)	N1-C1-C2	114.8(9)
C7-N3-Fe1	112.5(7)	N1-C1-H1	122.6
C16-N3-Fe1	124.4(6)	C2-C1-H1	122.6
C24-N4-C31	117.6(8)	C3-C2-N2	122.3(10)
C24-N4-Fe1	115.2(7)	C3-C2-C1	128.9(11)
C31-N4-Fe1	126.5(6)	N2-C2-C1	108.8(8)
C29-N5-C25	120.8(8)	C2-C3-C4	117.5(10)
C29-N5-Fe1	120.0(6)	C2-C3-H3	121.3
C25-N5-Fe1	119.2(6)	C4-C3-H3	121.3
C30-N6-C39	121.7(8)	C5-C4-C3	122.7(9)
C30-N6-Fe1	114.3(7)	C5-C4-H4	118.6
C39-N6-Fe1	124.0(6)	C3-C4-H4	118.6
O2-S1-O3	114.9(5)	C4-C5-C6	116.6(10)
O2-S1-O1	113.9(5)	C4-C5-H5	121.7
O3-S1-O1	116.1(5)	C6-C5-H5	121.7
O2-S1-C47	102.5(6)	N2-C6-C5	121.3(9)
O3-S1-C47	104.7(5)	N2-C6-C7	109.1(8)
O1-S1-C47	102.4(6)	C5-C6-C7	129.2(9)
F1-C47-F2	107.7(10)	N3-C7-C6	117.8(9)
F1-C47-F3	106.7(9)	N3-C7-H7	121.1
F2-C47-F3	105.5(9)	C6-C7-H7	121.1
F1-C47-S1	113.0(7)	C9-C8-N1	110.5(8)
F2-C47-S1	110.5(7)	C9-C8-C10	114.9(9)
F3-C47-S1	112.9(9)	N1-C8-C10	112.9(8)
O5-S2-O6	115.8(7)	C9-C8-H8	106.0
O5-S2-O4	115.5(6)	N1-C8-H8	106.0
O6-S2-O4	115.5(6)	C10-C8-H8	106.0

C8-C9-H9A	109.5	C19-C18-C23	118.2(9)
C8-C9-H9B	109.5	C19-C18-C16	121.8(8)
H9A-C9-H9B	109.5	C23-C18-C16	119.9(9)
C8-C9-H9C	109.5	C20-C19-C18	121.4(10)
H9A-C9-H9C	109.5	C20-C19-H19	119.3
H9B-C9-H9C	109.5	C18-C19-H19	119.3
C15-C10-C11	121.1(11)	C19-C20-C21	119.8(10)
C15-C10-C8	118.9(11)	C19-C20-H20	120.1
C11-C10-C8	119.9(10)	C21-C20-H20	120.1
C12-C11-C10	121.0(15)	C22-C21-C20	120.9(10)
C12-C11-H11	119.5	C22-C21-H21	119.6
C10-C11-H11	119.5	C20-C21-H21	119.6
C13-C12-C11	118.8(17)	C21-C22-C23	121.0(11)
C13-C12-H12	120.6	C21-C22-H22	119.5
C11-C12-H12	120.6	C23-C22-H22	119.5
C12-C13-C14	124.1(16)	C18-C23-C22	118.7(10)
C12-C13-H13	117.9	C18-C23-H23	120.7
C14-C13-H13	117.9	C22-C23-H23	120.7
C13-C14-C15	118.3(15)	N4-C24-C25	114.4(9)
C13-C14-H14	120.9	N4-C24-H24	122.8
C15-C14-H14	120.9	C25-C24-H24	122.8
C10-C15-C14	116.5(16)	N5-C25-C26	121.4(9)
C10-C15-H15	121.7	N5-C25-C24	111.1(8)
C14-C15-H15	121.7	C26-C25-C24	127.4(9)
N3-C16-C18	113.5(8)	C25-C26-C27	119.1(9)
N3-C16-C17	114.6(8)	C25-C26-H26	120.5
C18-C16-C17	108.8(8)	C27-C26-H26	120.5
N3-C16-H16	106.5	C28-C27-C26	119.1(9)
C18-C16-H16	106.5	C28-C27-H27	120.4
C17-C16-H16	106.5	C26-C27-H27	120.4
C16-C17-H17A	109.5	C27-C28-C29	119.4(9)
C16-C17-H17B	109.5	C27-C28-H28	120.3
H17A-C17-H17B	109.5	C29-C28-H28	120.3
C16-C17-H17C	109.5	N5-C29-C28	120.1(8)
H17A-C17-H17C	109.5	N5-C29-C30	110.0(8)
H17B-C17-H17C	109.5	C28-C29-C30	129.5(8)



N6-C30-C29	115.7(9)	N6-C39-C40	107.3(8)
N6-C30-H30	122.1	C41-C39-H39	107.7
C29-C30-H30	122.1	N6-C39-H39	107.7
C33-C31-N4	112.2(9)	C40-C39-H39	107.7
C33-C31-C32	111.9(8)	C39-C40-H40A	109.5
N4-C31-C32	113.3(8)	C39-C40-H40B	109.5
C33-C31-H31	106.3	H40A-C40-H40B	109.5
N4-C31-H31	106.3	C39-C40-H40C	109.5
C32-C31-H31	106.3	H40A-C40-H40C	109.5
C31-C32-H32A	109.5	H40B-C40-H40C	109.5
C31-C32-H32B	109.5	C46-C41-C42	118.0(8)
H32A-C32-H32B	109.5	C46-C41-C39	121.6(10)
C31-C32-H32C	109.5	C42-C41-C39	120.1(10)
H32A-C32-H32C	109.5	C43-C42-C41	121.3(10)
H32B-C32-H32C	109.5	C43-C42-H42	119.3
C34-C33-C38	119.5(9)	C41-C42-H42	119.3
C34-C33-C31	121.9(10)	C44-C43-C42	120.0(11)
C38-C33-C31	118.6(9)	C44-C43-H43	120.0
C33-C34-C35	121.0(11)	C42-C43-H43	120.0
C33-C34-H34	119.5	C43-C44-C45	120.3(10)
C35-C34-H34	119.5	C43-C44-H44	119.8
C36-C35-C34	120.0(11)	C45-C44-H44	119.8
C36-C35-H35	120.0	C46-C45-C44	119.8(11)
C34-C35-H35	120.0	C46-C45-H45	120.1
C37-C36-C35	120.3(11)	C44-C45-H45	120.1
C37-C36-H36	119.8	C45-C46-C41	120.4(11)
C35-C36-H36	119.8	C45-C46-H46	119.8
C36-C37-C38	120.5(12)	C41-C46-H46	119.8
C36-C37-H37	119.7	N1A-C2A-C3A	176(2)
C38-C37-H37	119.7	C2A-C3A-H3AA	109.5
C37-C38-C33	118.5(11)	C2A-C3A-H3AB	109.5
C37-C38-H38	120.8	H3AA-C3A-H3AB	109.5
C33-C38-H38	120.8	C2A-C3A-H3AC	109.5
C41-C39-N6	115.9(8)	H3AA-C3A-H3AC	109.5
C41-C39-C40	110.3(9)	H3AB-C3A-H3AC	109.5

---

Table 4.5. Bond lengths [ $\text{\AA}$ ] and angles [ $^\circ$ ] for the **R-MBA** derivative of complex **4.2**.

	U <sup>11</sup>	U <sup>22</sup>	U <sup>33</sup>	U <sup>23</sup>	U <sup>13</sup>	U <sup>12</sup>
Fe1	44(1)	22(1)	36(1)	1(1)	15(1)	-1(1)
N1	37(4)	26(4)	37(4)	-1(4)	13(3)	-5(4)
N2	42(5)	25(4)	45(5)	-5(4)	22(4)	-1(4)
N3	60(6)	23(4)	40(5)	-2(3)	22(4)	-7(4)
N4	38(4)	19(4)	37(4)	2(3)	17(3)	-1(3)
N5	33(4)	23(4)	38(5)	-5(3)	12(4)	0(3)
N6	32(4)	25(4)	42(4)	5(4)	9(3)	2(4)
S1	63(2)	36(1)	50(2)	1(1)	6(1)	6(1)
F1	67(5)	60(4)	90(5)	-11(4)	13(4)	22(3)
F2	80(5)	65(4)	101(5)	-32(5)	-10(4)	4(4)
F3	94(5)	66(4)	109(5)	6(5)	51(4)	-20(5)
O1	93(6)	56(5)	59(5)	-14(4)	7(4)	-4(5)
O2	81(6)	45(4)	74(5)	17(4)	37(4)	7(4)
O3	79(5)	44(4)	89(6)	-3(5)	11(4)	16(4)
C47	43(6)	40(6)	82(8)	-3(6)	20(6)	-4(5)
S2	58(2)	36(1)	63(2)	1(1)	17(1)	7(1)
F4	67(5)	107(5)	68(4)	3(4)	22(3)	8(4)
F5	135(8)	61(5)	84(5)	-22(4)	10(5)	-6(5)
F6	88(6)	93(6)	91(6)	35(5)	10(4)	21(5)
O4	59(5)	96(7)	92(7)	15(5)	29(5)	5(5)
O5	131(9)	51(5)	94(7)	-19(5)	37(6)	-9(6)
O6	75(5)	59(4)	69(5)	9(5)	3(4)	26(5)
C48	76(10)	56(8)	83(10)	-12(7)	29(8)	-8(7)
C1	48(6)	31(5)	36(5)	-3(4)	17(4)	-7(5)
C2	59(7)	27(5)	46(6)	7(5)	25(5)	2(5)
C3	53(7)	31(5)	50(6)	-2(5)	10(5)	12(5)
C4	67(8)	18(4)	44(6)	4(4)	10(5)	2(5)
C5	66(8)	33(5)	32(5)	-5(4)	17(5)	-5(5)
C6	49(7)	25(5)	30(5)	-2(4)	19(4)	-9(5)
C7	44(6)	32(5)	40(5)	-7(4)	13(4)	-13(5)
C8	39(6)	22(4)	43(6)	-2(4)	8(4)	-8(4)
C9	82(9)	44(6)	70(8)	-25(6)	35(6)	-29(6)

C10	55(7)	34(6)	53(7)	6(5)	8(5)	-10(5)
C11	53(8)	53(8)	88(10)	22(7)	18(7)	3(6)
C12	63(9)	51(8)	135(15)	-8(9)	44(10)	-7(7)
C13	109(15)	46(8)	131(16)	-18(10)	60(13)	-4(9)
C14	190(20)	74(11)	62(9)	-27(8)	56(11)	-80(12)
C15	88(10)	78(9)	62(8)	-5(7)	25(7)	-50(8)
C16	37(5)	36(6)	37(5)	-3(4)	5(4)	4(4)
C17	37(6)	36(5)	71(7)	-9(5)	4(5)	-6(4)
C18	38(5)	34(5)	48(6)	4(4)	22(4)	3(4)
C19	48(6)	30(5)	55(6)	2(4)	14(4)	-1(5)
C20	49(7)	32(5)	87(9)	-1(5)	27(6)	6(5)
C21	73(8)	47(6)	66(7)	-7(6)	30(6)	19(6)
C22	109(11)	52(7)	80(9)	-6(6)	49(8)	21(7)
C23	91(9)	37(5)	53(7)	9(5)	40(6)	16(5)
C24	57(6)	25(5)	50(6)	3(4)	30(5)	2(5)
C25	50(6)	23(5)	45(6)	0(4)	15(5)	0(4)
C26	53(6)	22(5)	42(6)	-1(4)	15(5)	4(4)
C27	48(7)	24(5)	61(7)	6(5)	6(5)	10(5)
C28	60(7)	31(5)	34(5)	-2(4)	10(4)	7(5)
C29	35(5)	33(5)	30(5)	3(4)	5(4)	0(4)
C30	51(6)	25(5)	41(6)	10(4)	8(5)	8(4)
C31	51(6)	33(5)	43(5)	2(4)	17(4)	3(4)
C32	90(9)	35(5)	32(5)	6(4)	12(5)	7(6)
C33	58(7)	28(5)	45(6)	-8(4)	18(5)	-6(4)
C34	81(8)	34(5)	41(6)	8(5)	26(5)	9(5)
C35	94(10)	32(5)	58(7)	13(5)	18(6)	5(6)
C36	90(10)	48(6)	45(6)	-7(5)	16(6)	-25(6)
C37	77(9)	60(8)	68(8)	13(6)	38(7)	15(7)
C38	81(9)	40(6)	65(8)	2(5)	38(7)	-6(6)
C39	57(6)	23(4)	33(5)	-3(4)	9(4)	6(4)
C40	70(8)	36(5)	49(6)	-4(5)	29(5)	1(5)
C41	51(6)	19(4)	44(6)	-7(4)	19(5)	-5(5)
C42	49(6)	31(5)	49(6)	-6(4)	12(5)	4(5)
C43	52(6)	35(5)	74(8)	-2(6)	25(6)	0(5)
C44	76(9)	41(6)	62(7)	-5(5)	40(7)	-16(6)
C45	68(8)	42(6)	44(6)	0(5)	20(5)	-1(5)

C46	46(7)	40(6)	50(7)	-5(5)	15(6)	4(5)
N1A	138(12)	83(6)	129(11)	11(9)	98(9)	-14(9)
C2A	112(9)	95(9)	97(8)	-8(7)	60(7)	-16(7)
C3A	148(14)	139(13)	135(13)	24(11)	66(12)	-30(12)

Table 4.6 Anisotropic displacement parameters ( $\text{\AA}^2 \times 10^3$ ) for the **R-MBA** derivative of complex **4.2**. The anisotropy displacement factor exponent takes the form:  $-2\pi^2 [ h^2 a^{*2} U^{11} + \dots + 2 h k a^* b^* U^{12} ]$

	x	y	z	U(eq)
H1	4360	2832	7507	45
H3	4748	4829	6966	53
H4	5986	6035	6836	51
H5	7630	5631	7268	51
H7	8881	4072	8010	46
H8	5396	530	8414	41
H9A	4238	-95	7163	95
H9B	5192	340	6762	95
H9C	4210	1003	6646	95
H11	3026	1551	7530	77
H12	1743	1711	8450	96
H13	2041	1592	10087	110
H14	3546	1088	10905	125
H15	4940	910	9964	89
H16	8979	1904	9354	44
H17A	10500	2660	9616	73
H17B	9715	3567	9529	73
H17C	10295	3311	8630	73
H19	9743	323	9233	52
H20	10424	-920	8333	65
H21	10724	-568	6756	72
H22	10413	1015	6092	92
H23	9685	2306	6962	69

H24	7330	126	6210	50
H26	7962	-1381	7511	46
H27	8185	-1881	9162	53
H28	7837	-712	10348	50
H30	7191	1276	10671	46
H31	5872	2139	5920	50
H32A	5958	1381	4450	78
H32B	6030	491	5251	78
H32C	6991	872	4827	78
H34	5957	3754	5278	60
H35	6834	5128	4745	73
H36	8520	5012	4787	73
H37	9316	3490	5207	79
H38	8433	2051	5651	71
H39	6180	3493	9585	45
H40A	8135	3446	10617	75
H40B	7455	4441	10555	75
H40C	7824	3995	9589	75
H42	4849	3248	10433	51
H43	4190	3033	11885	62
H44	5194	2670	13311	68
H45	6900	2506	13305	60
H46	7564	2670	11844	53
H3AA	8034	-870	13632	204
H3AB	8742	-570	12849	204
H3AC	8281	-1694	12843	204

---

Table 4.7. Hydrogen coordinates ( $\times 10^4$ ) and isotropic displacement parameters ( $\text{\AA}^2 \times 10^3$ ) for the *R*-MBA derivative of complex **4.2**.

N2-Fe1-N1-C1	0.6(6)	N1-Fe1-N4-C31	63.1(7)
N5-Fe1-N1-C1	-177.7(6)	N6-Fe1-N4-C31	149.6(9)
N6-Fe1-N1-C1	103.0(6)	N3-Fe1-N4-C31	-98.1(7)
N4-Fe1-N1-C1	-98.3(7)	N1-Fe1-N5-C29	-89.6(7)
N3-Fe1-N1-C1	15.8(13)	N6-Fe1-N5-C29	-2.5(7)
N2-Fe1-N1-C8	177.1(7)	N4-Fe1-N5-C29	-176.4(7)
N5-Fe1-N1-C8	-1.3(7)	N3-Fe1-N5-C29	85.7(7)
N6-Fe1-N1-C8	-80.6(7)	N1-Fe1-N5-C25	90.7(8)
N4-Fe1-N1-C8	78.2(7)	N6-Fe1-N5-C25	177.7(8)
N3-Fe1-N1-C8	-167.7(8)	N4-Fe1-N5-C25	3.8(7)
N1-Fe1-N2-C2	-0.5(7)	N3-Fe1-N5-C25	-94.0(7)
N6-Fe1-N2-C2	-87.7(8)	N2-Fe1-N6-C30	-178.1(7)
N4-Fe1-N2-C2	87.2(8)	N5-Fe1-N6-C30	-0.8(7)
N3-Fe1-N2-C2	-175.2(8)	N1-Fe1-N6-C30	102.3(7)
N1-Fe1-N2-C6	180.0(8)	N4-Fe1-N6-C30	15.9(13)
N6-Fe1-N2-C6	92.7(7)	N3-Fe1-N6-C30	-98.0(7)
N4-Fe1-N2-C6	-92.4(7)	N2-Fe1-N6-C39	3.3(8)
N3-Fe1-N2-C6	5.3(7)	N5-Fe1-N6-C39	-179.4(8)
N2-Fe1-N3-C7	-2.4(6)	N1-Fe1-N6-C39	-76.3(8)
N5-Fe1-N3-C7	175.7(6)	N4-Fe1-N6-C39	-162.7(8)
N1-Fe1-N3-C7	-17.6(12)	N3-Fe1-N6-C39	83.4(8)
N6-Fe1-N3-C7	-104.7(6)	O2-S1-C47-F1	-57.5(9)
N4-Fe1-N3-C7	94.9(7)	O3-S1-C47-F1	-177.7(8)
N2-Fe1-N3-C16	166.6(7)	O1-S1-C47-F1	60.8(9)
N5-Fe1-N3-C16	-15.2(7)	O2-S1-C47-F2	63.3(9)
N1-Fe1-N3-C16	151.4(8)	O3-S1-C47-F2	-56.9(9)
N6-Fe1-N3-C16	64.3(7)	O1-S1-C47-F2	-178.4(8)
N4-Fe1-N3-C16	-96.1(7)	O2-S1-C47-F3	-178.7(8)
N2-Fe1-N4-C24	174.0(7)	O3-S1-C47-F3	61.0(9)
N5-Fe1-N4-C24	-3.1(7)	O1-S1-C47-F3	-60.5(9)
N1-Fe1-N4-C24	-106.3(7)	O5-S2-C48-F5	179.7(11)
N6-Fe1-N4-C24	-19.8(13)	O6-S2-C48-F5	-59.4(12)
N3-Fe1-N4-C24	92.5(7)	O4-S2-C48-F5	60.2(12)
N2-Fe1-N4-C31	-16.5(8)	O5-S2-C48-F6	53.8(11)
N5-Fe1-N4-C31	166.3(7)	O6-S2-C48-F6	174.6(9)

O4-S2-C48-F6	-65.7(11)	C10-C11-C12-C13	2(2)
O5-S2-C48-F4	-63.7(10)	C11-C12-C13-C14	-4(2)
O6-S2-C48-F4	57.2(10)	C12-C13-C14-C15	4(2)
O4-S2-C48-F4	176.8(9)	C11-C10-C15-C14	1.0(18)
C8-N1-C1-C2	-177.4(7)	C8-C10-C15-C14	-176.7(11)
Fe1-N1-C1-C2	-0.6(10)	C13-C14-C15-C10	-2(2)
C6-N2-C2-C3	2.0(15)	C7-N3-C16-C18	-112.9(9)
Fe1-N2-C2-C3	-177.5(8)	Fe1-N3-C16-C18	79.0(9)
C6-N2-C2-C1	179.8(8)	C7-N3-C16-C17	12.9(11)
Fe1-N2-C2-C1	0.3(11)	Fe1-N3-C16-C17	-155.1(6)
N1-C1-C2-C3	177.9(10)	N3-C16-C18-C19	-129.9(10)
N1-C1-C2-N2	0.3(12)	C17-C16-C18-C19	101.2(11)
N2-C2-C3-C4	-2.6(15)	N3-C16-C18-C23	51.3(14)
C1-C2-C3-C4	-179.9(10)	C17-C16-C18-C23	-77.5(12)
C2-C3-C4-C5	0.3(15)	C23-C18-C19-C20	-1.0(17)
C3-C4-C5-C6	2.3(14)	C16-C18-C19-C20	-179.8(10)
C2-N2-C6-C5	0.8(14)	C18-C19-C20-C21	0.3(18)
Fe1-N2-C6-C5	-179.7(7)	C19-C20-C21-C22	1(2)
C2-N2-C6-C7	173.8(8)	C20-C21-C22-C23	-2(2)
Fe1-N2-C6-C7	-6.7(10)	C19-C18-C23-C22	0.3(18)
C4-C5-C6-N2	-2.8(13)	C16-C18-C23-C22	179.1(12)
C4-C5-C6-C7	-174.2(9)	C21-C22-C23-C18	1(2)
C16-N3-C7-C6	-169.9(8)	C31-N4-C24-C25	-168.4(8)
Fe1-N3-C7-C6	-0.5(10)	Fe1-N4-C24-C25	2.0(11)
N2-C6-C7-N3	4.4(12)	C29-N5-C25-C26	-1.4(15)
C5-C6-C7-N3	176.6(9)	Fe1-N5-C25-C26	178.4(8)
C1-N1-C8-C9	78.5(11)	C29-N5-C25-C24	176.5(8)
Fe1-N1-C8-C9	-97.8(10)	Fe1-N5-C25-C24	-3.8(11)
C1-N1-C8-C10	-51.6(11)	N4-C24-C25-N5	1.0(13)
Fe1-N1-C8-C10	132.1(8)	N4-C24-C25-C26	178.6(10)
C9-C8-C10-C15	142.8(11)	N5-C25-C26-C27	2.0(16)
N1-C8-C10-C15	-89.4(12)	C24-C25-C26-C27	-175.5(10)
C9-C8-C10-C11	-34.9(15)	C25-C26-C27-C28	0.1(16)
N1-C8-C10-C11	93.0(12)	C26-C27-C28-C29	-2.7(16)
C15-C10-C11-C12	-1(2)	C25-N5-C29-C28	-1.3(14)
C8-C10-C11-C12	176.7(12)	Fe1-N5-C29-C28	179.0(8)



C25-N5-C29-C30	-175.4(9)	C35-C36-C37-C38	-1.0(18)
Fe1-N5-C29-C30	4.9(11)	C36-C37-C38-C33	-1.6(17)
C27-C28-C29-N5	3.3(16)	C34-C33-C38-C37	1.9(16)
C27-C28-C29-C30	176.1(11)	C31-C33-C38-C37	-179.4(10)
C39-N6-C30-C29	-177.7(8)	C30-N6-C39-C41	-26.1(14)
Fe1-N6-C30-C29	3.7(12)	Fe1-N6-C39-C41	152.4(8)
N5-C29-C30-N6	-5.4(13)	C30-N6-C39-C40	97.5(11)
C28-C29-C30-N6	-178.8(10)	Fe1-N6-C39-C40	-84.0(9)
C24-N4-C31-C33	-119.6(9)	N6-C39-C41-C46	79.9(13)
Fe1-N4-C31-C33	71.2(9)	C40-C39-C41-C46	-42.2(13)
C24-N4-C31-C32	8.4(12)	N6-C39-C41-C42	-106.1(11)
Fe1-N4-C31-C32	-160.8(7)	C40-C39-C41-C42	131.8(10)
N4-C31-C33-C34	-128.1(11)	C46-C41-C42-C43	-3.0(14)
C32-C31-C33-C34	103.2(12)	C39-C41-C42-C43	-177.2(9)
N4-C31-C33-C38	53.3(12)	C41-C42-C43-C44	2.0(15)
C32-C31-C33-C38	-75.5(13)	C42-C43-C44-C45	0.1(16)
C38-C33-C34-C35	0.3(16)	C43-C44-C45-C46	-1.1(16)
C31-C33-C34-C35	-178.4(10)	C44-C45-C46-C41	0.0(16)
C33-C34-C35-C36	-2.9(17)	C42-C41-C46-C45	2.0(15)
C34-C35-C36-C37	3.2(17)	C39-C41-C46-C45	176.1(9)

---

Table 4.8. Torsion angles [°] for for the **R-MBA** derivative of complex 4.2.

#### 4.5 REFERENCES

- (1) Anslyn, E. V.; Nieto, S.; Dragna, J. M. Chem-Eur J 2010, 16, 227.

## Chapter 5. Correlating Hydrophobicity in Guest Binding to Cyclodextrin with Guest Partitioning Between Water and n-Octanol

### 5.1 INTRODUCTION

A large subset of supramolecular chemistry research is devoted to the design of molecular hosts that can bind a guest with high affinity and high selectivity.<sup>1-4</sup> In order to design selective host molecules with high affinity chemists consider which supramolecular interactions are complementary to the guest and attempt to incorporate these into the host *via* organic synthesis.

In contrast to supramolecular chemistry, drug discovery and design depends on design of small molecules (guests) that have a high affinity and high selectivity for a particular protein (host). Drug chemists attempt to synthesize small molecules with binding motifs that are complementary to the binding site of the protein.<sup>5-8</sup>

Supramolecular chemists and biochemists have been successful at identifying the binding motifs that are involved in the noncovalent association of host-guest systems and biological systems such as hydrogen bonding, dipole-dipole, and hydrophobic interactions.<sup>1-4</sup> However, it is not intuitive how to incorporate these binding motifs into a host or small molecule to achieve high selectivity and high affinity for a guest or protein. In both cases chemists iteratively design, synthesize, and measure the affinity of the host or small molecule to the guest or protein. This process is repeated until the desired level of selectivity and affinity is reached, which is costly and time-consuming. The number of necessary cycles, and thus, the cost and time intensity, to reach high selectivity and high affinity is dependent on the efficiency of the design process. Thus, methodologies that improve the efficiency of the design process for host-guest and protein-small molecule systems are desirable.

The ultimate goal of this project is to develop a method for predicting the free energy, entropy, and enthalpy of binding for both abiotic and biological systems. As a starting point, we were interested in developing a simple method for predicting the contributions of hydrophobicity to binding events.

### **5.1.1 Design Criteria**

We chose cyclodextrin as our initial host system to study. Cyclodextrin was chosen for study because the driving force for binding to cyclodextrin is almost exclusively hydrophobic. Because binding is mostly hydrophobic, we predicted it should be possible to correlate hydrophobicity with the thermodynamic parameters  $\Delta G$ ,  $\Delta H$ , and  $\Delta S$  of binding. The partition coefficient between water and n-octanol is a measure of hydrophobicity, and, thus, it could be used to assign a numerical value to the hydrophobicity of a particular guest. Our hypothesis is that, if the driving force for a particular guest to partition from water into n-octanol is hydrophobicity, and the driving force for the same guest to associate with cyclodextrin in aqueous solution is hydrophobic, then for a set of guests there should be a correlation between the thermodynamics parameters of partitioning and the thermodynamic parameters of binding (Figure 5.1). It is expected that as the  $\Delta G$ ,  $\Delta H$ , and  $\Delta S$  of partitioning from water to n-octanol becomes more favorable, the  $\Delta G$ ,  $\Delta H$  and  $\Delta S$  of binding to the hydrophobic cavity of cyclodextrin should also become more favorable, and thus the parameters should be correlated.

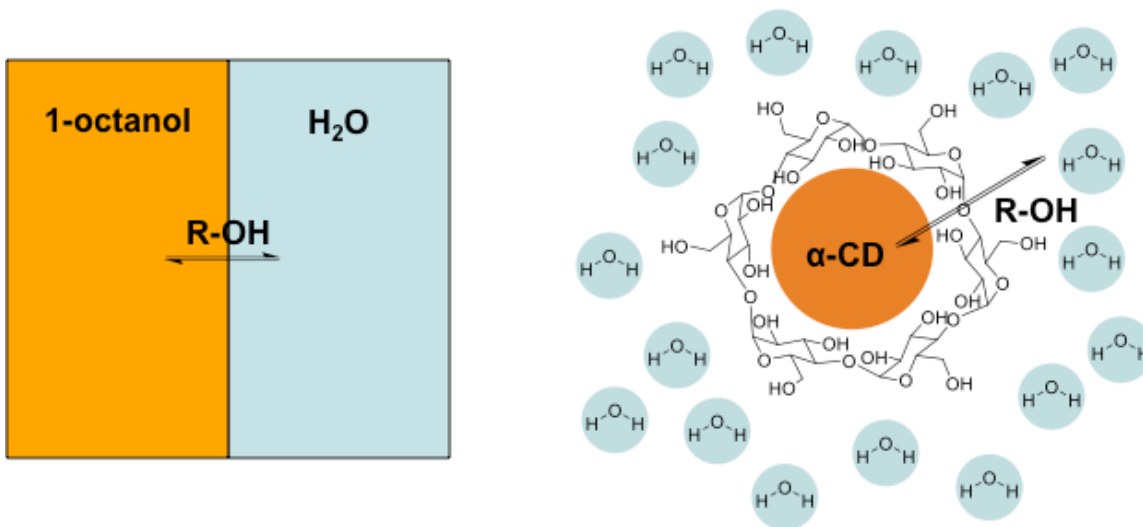


Figure 5.1. An illustration of the similarities between the partitioning of a guest, in this case an alcohol, into water/n-octanol and binding to cyclodextrin (labeled  $\alpha$ -CD). The water is in blue, and the hydrophobic areas are labeled in orange.

Further, cyclodextrin was chosen because there is already a lot of thermodynamic data available on its host-guest chemistry<sup>9-11</sup> eliminating the need for experimentation to generate our own thermodynamic parameters for binding, which is time-consuming and not the goal of this project.

## 5.2 RESULTS AND DISCUSSION

### 5.2.1 Alcohols

Aliphatic alcohols were chosen for initial studies because of their simplicity and the availability of data on both their binding to cyclodextrin<sup>9-11</sup> and partitioning between water and octanol.<sup>12,13</sup> The  $\Delta G$  of binding of the alcohols to cyclodextrin was plotted as a

function of the  $\Delta G$  of partitioning of the alcohols between n-octanol and water. As can be seen in Figure 5.2, there is an approximately linear relationship between the  $\Delta G$  of alcohols binding to cyclodextrin and the  $\Delta G$  of partitioning between n-octanol and water. In particular, alkanols without form a straight line with little to no scatter. The nonlinear alcohols, 2,2 dimethyl-1-propanol, 2-methyl-1-propanol, and 2-propanol, are outliers. The nonlinear alcohols are most likely outliers due to different steric interactions with the host in comparison to the linear alkanols. The graph confirms our hypothesis that, as the free energy of partitioning from water to n-octanol becomes more favorable, the binding to the hydrophobic cavity of cyclodextrin also becomes more favorable.

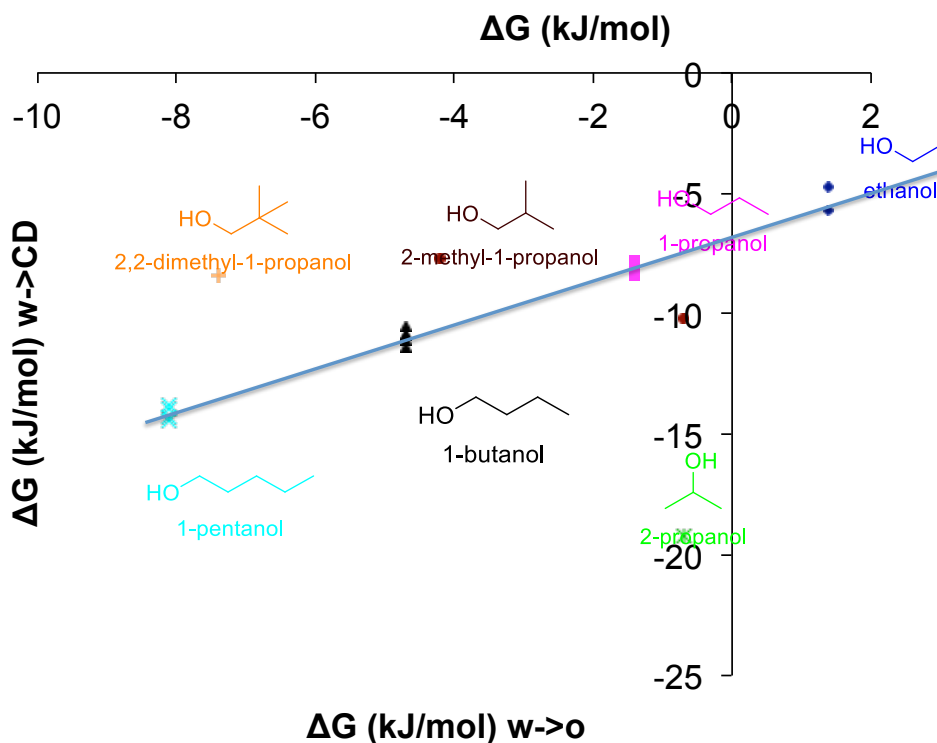


Figure 5.2. A plot of the free energy of binding to  $\alpha$ -cyclodextrin as a function of the free energy of transfer from water to n-octanol for a variety of alcohols.

The  $\Delta H$  of binding of alcohols to cyclodextrin was also plotted as a function of  $\Delta H$  of partitioning of alcohols from water to n-octanol revealing another linear relationship (Figure 5.3). Again, the graph confirms our hypothesis that the  $\Delta H$  of binding to cyclodextrin is correlated with the  $\Delta H$  of partitioning from water to n-octanol.

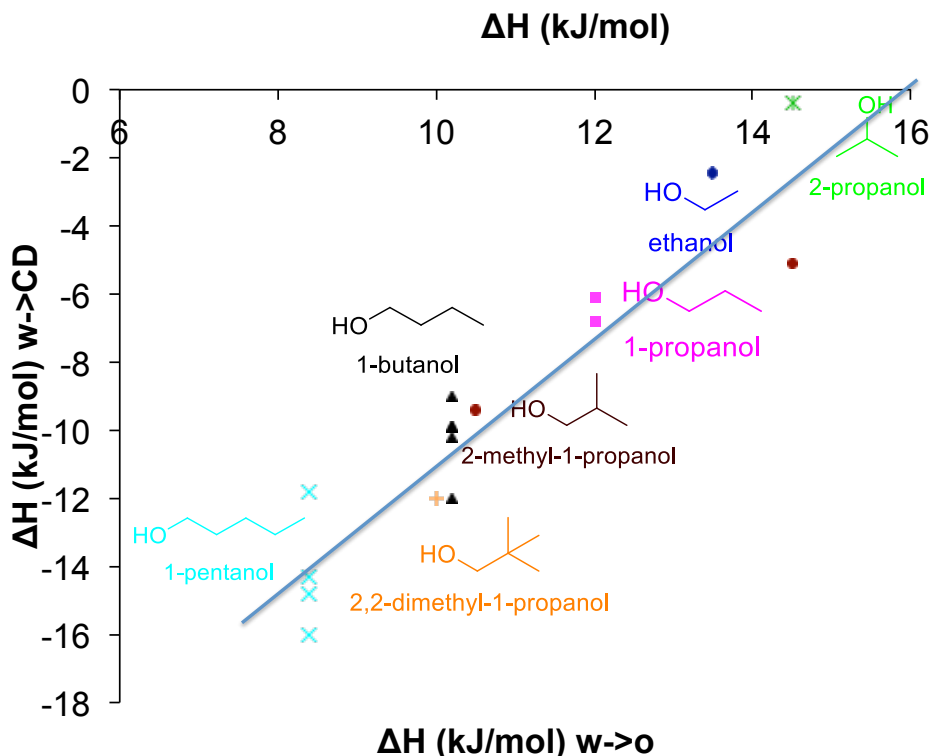


Figure 5.3. A plot of the enthalpy of binding to  $\alpha$ -cyclodextrin as a function of the enthalpy of transfer from water to n-octanol for a variety of alcohols.

Lastly, the  $\Delta S$  of binding of alcohols to cyclodextrin was also plotted as a function of  $\Delta S$  of partitioning of alcohols from water to n-octanol (Figure 5.4). However, with the exception of two outliers, the plot is relatively flat, and thus, the driving force behind binding to cyclodextrin and partitioning from water to n-octanol is an enthalpically driven hydrophobic process. However, it has a large unfavorable entropy of binding to cyclodextrin in comparison to the linear alkanols. This may be due to steric interactions with the cyclodextrins not present for the linear alkanols that restrict of the

movement of the tert-butyl group, and thus, make it entropically disfavored. On the other hand, inexplicably, 2-propanol has a large favorable entropy in comparison to the other linear alkanols.

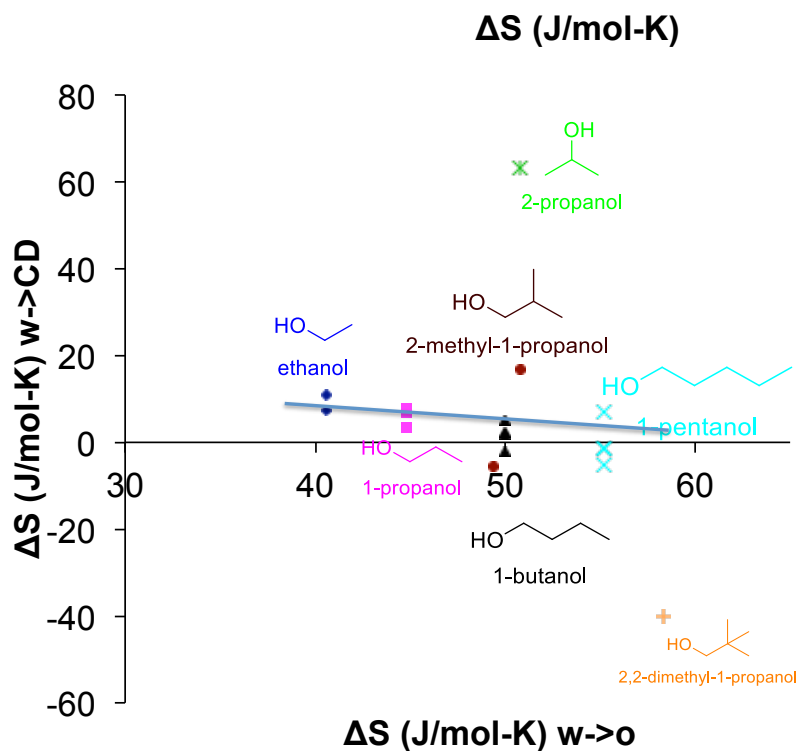


Figure 5.4. A plot of the entropy of binding to  $\alpha$ -cyclodextrin as a function of the entropy of transfer from water to n-octanol for a variety of alcohols.

### 5.2.2 Substituted Benzenes

In order to see if the thermodynamic parameters for partitioning can be correlated with other guests that bind to cyclodextrins, we explored the binding of substituted benzenes. The thermodynamic data of substituted benzenes binding to cyclodextrins<sup>9-11</sup> and partitioning between water and n-octanol<sup>14</sup> was available in the literature. Several plots were made of the different thermodynamic parameters that compare the binding of substituted benzenes to cyclodextrin with the partitioning of the substituted benzenes from



water to n-octanol. However, there is no simple relationship between the binding of substituted benzenes and partitioning of substituted benzenes from water to n-octanol. The lack of correlation is likely due to steric interactions between the substituted benzenes and cyclodextrin that are not present for substituted benzenes partitioning into n-octanol.

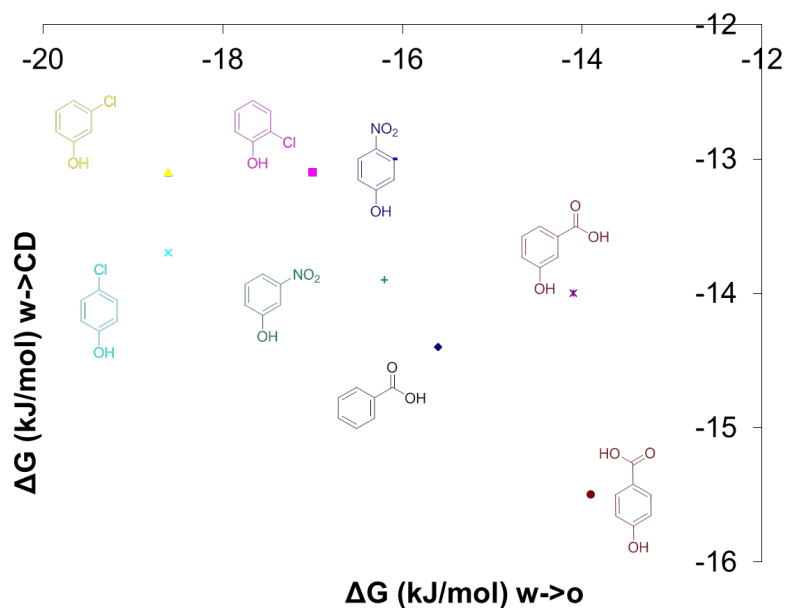


Figure 5.5. A plot of the free energy of binding to  $\beta$ -cyclodextrin as a function of the free energy of transfer from water to n-octanol for a variety of alcohols.

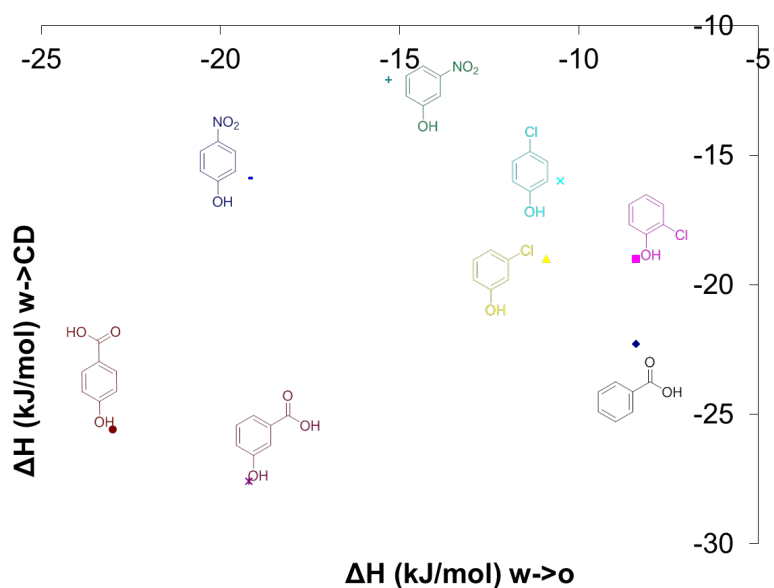


Figure 5.6. A plot of the enthalpy of binding to  $\beta$ -cyclodextrin as a function of the enthalpy of transfer from water to n-octanol for a variety of substituted benzenes.

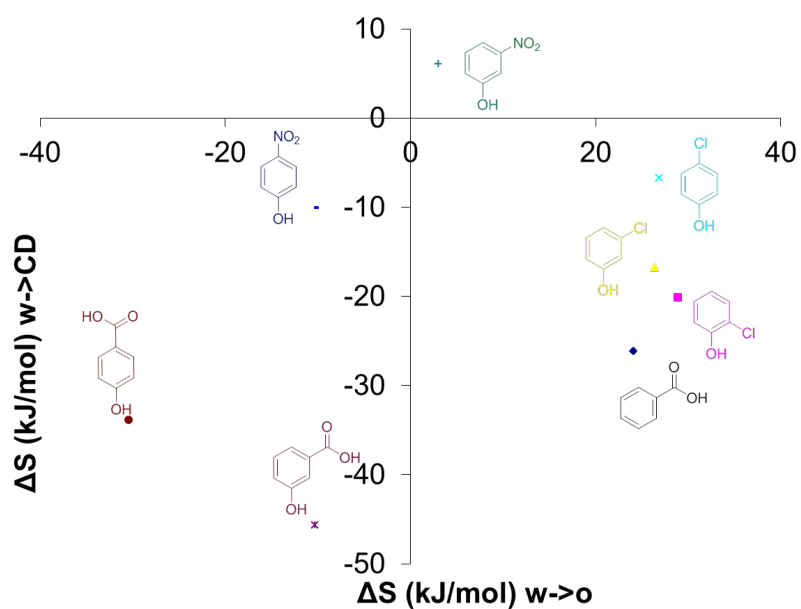


Figure 5.7. A plot of the entropy of binding to  $\beta$ -cyclodextrin as a function of the entropy of transfer from water to n-octanol for a variety of substituted benzenes.

### 5.3 SUMMARY

The goal of this project was to assess the hypothesis that the thermodynamic parameters of partitioning from water to n-octanol can be used to predict the hydrophobic contributions to binding in host-guest systems. Cyclodextrin was chosen as the host system for study because the driving force for guest binding to cyclodextrin is almost exclusively hydrophobic. Plots of the thermodynamic parameters of aliphatic alcohols binding to cyclodextrin as a function of the thermodynamic parameters of partitioning of alcohols from water to n-octanol showed a linear correlation between  $\Delta H$  and  $\Delta G$ , which provides evidence for our hypothesis that there will be a correlation between the  $\Delta G$ ,  $\Delta H$ , and  $\Delta S$  of partitioning from water to octanol and the  $\Delta G$ ,  $\Delta H$ , and  $\Delta S$  of binding to a hydrophobic host. The  $\Delta S$  plot was essentially flat due to low contributions of entropy to the binding events, but it is reasonable to assume that if the  $\Delta H$  and  $\Delta G$  of partitioning correlates with  $\Delta H$  and  $\Delta G$  of binding to a hydrophobic host,  $\Delta S$  will also correlate.

Plots of the thermodynamic parameters of substituted benzenes binding to cyclodextrin as a function of the thermodynamic parameters of partitioning of substituted benzenes from water to n-octanol showed no correlation for any of the parameters. We believe sterics played a role in the lack of a linear correlation between cyclodextrin binding and partitioning between water and n-octanol.

Currently, the thermodynamics of partitioning and binding are being studied for a series linear aliphatic amines.

### 5.4 REFERENCES

- (1) Cram, D. J. *Nature* 1992, 356, 29.
- (2) Cram, D. J.; Karch, S.; Kim, Y. H.; Baczynskyj, L.; Marti, K.; Sampson, R. M.; Kallemeyn, G. W. *J Am Chem Soc* 1988, 110, 2554.

- (3) Lehn, J. M. *Angew Chem Int Edit* 1990, 29, 1304.
- (4) Zhang, N.; Zhong, R. G.; Yan, H.; Jiang, Y. J. *Chem Biol Drug Des* 2011, 77, 199.
- (5) Blasi, D.; Pinto, M.; Nieto, J.; Arsequell, G.; Valencia, G.; Planas, A.; Centeno, N. B.; Quintana, J. *Amyloid* 2011, 18, 55.
- (6) Du, Q. S.; Wei, H.; Huang, R. B.; Chou, K. C. *Expert Opin Drug Dis* 2011, 6, 619.
- (7) Huang, N. K.; Lin, J. H.; Lin, J. T.; Lin, C. I.; Liu, E. M. W.; Lin, C. J.; Chen, W. P.; Shen, Y. C.; Chen, H. M.; Chen, J. B.; Lai, H. L.; Yang, C. W.; Chiang, M. C.; Wu, Y. S.; Chang, C.; Chen, J. F.; Fang, J. M.; Lin, Y. L.; Chern, Y. J. *Plos One* 2011, 6.
- (8) Mavromoustakos, T.; Durdagi, S.; Koukoulitsa, C.; Simcic, M.; Papadopoulos, M. G.; Hodoscek, M.; Grdadolnik, S. G. *Curr Med Chem* 2011, 18, 2517.
- (9) Chen, W.; Chang, C. E.; Gilson, M. K. *Biophys J* 2004, 87, 3035.
- (10) Guo, Q. X.; Luo, S. H.; Liu, Y. C. *J Inclusion Phenom Mol* 1998, 30, 173.
- (11) Takuma, T.; Deguchi, T.; Sanemasa, I. *B Chem Soc Jpn* 1990, 63, 1246.
- (12) Delisi, R.; Goffredi, M.; Liveri, V. T. *J Chem Soc Chem Comm* 1980, 380.
- (13) Goffredi, M.; Liveri, V. T. *J Phys Chem-US* 1982, 86, 2455.
- (14) Dearden, J. C.; Bresnen, G. M. *Int J Mol Sci* 2005, 6, 119.